Aerodynamic analysis of a 2D LEI airfoil

An experimental and numerical study

T.L.B. van Lith

Technische Universiteit Delft

TU Delft

Cover image: Oil flow figure of the suction side of the V3 model at $\alpha = 17°$

Aerodynamic analysis of a 2D LEI airfoil

An experimental and numerical study

by

T.L.B. van Lith

to obtain the degree of Master of Science
at the Delft University of Technology,
to be defended publicly on Monday December 1, 2025 at 09:30 AM.

Student number: 4874536
2025 duration: March 3, 2025 – December 1, 2025
Thesis committee:

Dr.-ing. A. H. van Zuijlen	TU Delft, chair
Dr.-ing. D. A. M. De Tavernier,	TU Delft, examiner
Dr.-ing. R. Schmehl,	TU Delft, supervisor
MSc J. A. W. Poland,	TU Delft, supervisor

TU Delft

This project was supported by the MERIDIONAL project, which has received funding from the European Union's Horizon Europe research and innovation programme under grant agreement No 101084216.

Preface

When I started my master's in wind energy in 2023, I expected to dive deeper into the concepts of classic horizontal-axis wind turbines, which you can see all around us. Little did I know that this master also broadened my knowledge by introducing me to different concepts to harness energy from the wind. One of these concepts is airborne wind energy. The concept was introduced to me by Roland, who gave the course in the first two quarters of my master's.

The past 9 months have been a great experience, as working in a wind tunnel is very unique. The fact that I could work in a wind tunnel and test physical scale models also fits with my personality, as I like to tinker with, build, and mend stuff. This thesis was the perfect balance of academic research and working with this test facility, and for that, I want to express my sincere gratitude to Roland Schmehl and Jelle Poland for supervising me during my thesis, but also for providing me with this opportunity. Even though Jelle already had multiple master's students under his supervision, he did manage to create some time to help me with my research. Next to Jelle and Roland, I want to thank Delphine de Tavernier, as she suggested talking to Jelle. Without our conversations, I would not have met Jelle.

Prior to and during the wind tunnel tests, I have had multiple meetings with Stefan Bernardy to get a better understanding of how these unconventional kite airfoils can be tested in the wind tunnel. With his invaluable experience, the decision for several key design parameters of the scale model could be made faster, as there was a bit of time pressure. Furthermore, when the scale models had arrived, Emiel Langedijk helped me greatly by preparing the model to go in the wind tunnel, helping with the installation of all the testing equipment required during testing, and quickly swapping the two scale models during the test week. Without Stefan and Emiel, this would have been impossible.

The results of my thesis are a great foundation for future experimental research on the unconventional kite airfoils. I am thrilled to see what new developments will come and how the airborne wind energy sector will grow in the future.

At last, I want to thank my girlfriend, Kariann, and my brothers, Bram and Joep, for their support during my thesis, as speaking with them was a great outlet. Finally, I want to thank my parents, Marius and Jorien, for their support as well, but also for bringing ice cream during the wind tunnel test when it was 35+°C inside the wind tunnel facility.

Thank you all

Thijs

T.L.B. van Lith
Delft, December 2025

Abstract

This study analyses the aerodynamic behaviour of a two-dimensional (2D) rigid leading edge inflatable (LEI) airfoil. The aerodynamic data is obtained by experiments performed in the low turbulence tunnel (LTT) at the TU Delft as well as performing computational fluid dynamics (CFD) on the tested models. One of the goals is to experimentally obtain the lift and drag coefficients and compare the experimental data with the results of existing CFD toolchains. Previously, this was not possible as there was no dedicated 2D-rigid LEI airfoil data available for validating CFD results. Furthermore, the flow topology and the boundary layer development is analysed and compared to the results of the CFD toolchain.

The wind tunnel experiments have been performed with two different scale models at a Reynolds number of $\mathrm{Re} = 5 \times 10^5$ and $\mathrm{Re} = 10^6$. The angles of attack ranged from $\alpha = -10°$ to $\alpha = 25°$. One of the scale models is the airfoil at midspan of the V3 kite. The profile geometry of the second scale model is chosen to maximise the lift coefficient of the airfoil. Both models are constructed of steel with a canopy thickness of $2\,\mathrm{mm}$ to suppress the deflection of the canopy under the aerodynamic load. The aerodynamic coefficients are measured using pressure strips on the walls of the wind tunnel and a wake rake behind the airfoil. The aerodynamic coefficients had to be corrected due to the influence of the wind tunnel walls and the wake rake. The correction factors allow the data to approach unbounded airflow. The transitional behaviour of the boundary layer was determined using infrared imaging and oil flow visualisation. During testing, a microphone was used to quickly validate the infrared images. The two models were tested with zigzag tapes placed in different locations. The zigzag tape forced the boundary layer into a turbulent state.

The numerical data on the two models have been acquired through an automated CFD toolchain. The CFD toolchain uses Reynolds-averaged Navier-Stokes (RANS) simulations employing the $k-\omega$ shear stress transport (SST) turbulence model, simulating a fully turbulent boundary layer. In addition, The $\gamma - \tilde{\mathrm{Re}}_{\theta \mathrm{t}}$ transition model is used to simulate the transitional behaviour of the airfoil. The simulations were performed with the open-source CFD software OpenFOAM, using structured meshes generated with Pointwise. The lift, drag, pressure and friction coefficient, as well as the streamline figure around the airfoil, were simulated using CFD.

The experimental results were used to quantify the effects of zigzag tapes, differences due to Reynolds number, to visualize the flow topology, and to validate the CFD results. A zigzag tape on the suction side lowered the stall angle and the maximum lift coefficient. Tripped, fully turbulent, and untripped cases were compared with the CFD results. The fully turbulent assumption agreed best with the measurements. The transition model converged only at high angles of attack. As it is difficult to simulate separation with RANS, the data around the stall angle did not match. Infrared thermography mapped transition versus angle of attack. For the V3 model, the transition location remained essentially fixed from an angle of attack of $3°$ onward, while for the second model it moved steadily toward the leading edge as the angle of attack increased. Oil flow visualisations on the pressure and suction sides were consistent with the computed skin friction distribution and revealed a corner eddy and a recirculation zone. A laminar separation bubble was also observed on the V3 suction side.

In conclusion, this research investigated the experimental and numerical data of 2D-rigid LEI airfoils. The experiments are the first of their kind, as no dedicated LEI airfoils had ever been analysed experimentally, and this work therefore provides the basis for future experimental studies. The influence of the zigzag tapes used to trip the boundary layer showed a pronounced effect on the airfoil polars. The experimental data was used to validate the developed CFD toolchain by comparing it to numerical results, which showed good agreement when assuming fully turbulent flow. Furthermore, the oil-flow visualisation confirmed the presence of a laminar separation bubble on the suction side of the V3 model, while on the pressure side a corner eddy and the recirculation zone were observed.

Contents

List of Figures

List of Tables

Nomenclature

Abbreviations

2D	Two dimensional
3D	Three dimensional
AWE	Airborne Wind Energy
BF	Blockage Factor
CFD	Computational Fluid Dynamics
CI	Confidence interval
DC	Direct Current
FEM	Finite Element Method
FSI	Fluid–Structure Interaction
HPC	High performance computer
IR	Infrared
KCU	Kite Control Unit
LE	Leading edge
LEI	Leading Edge Inflatable
LTT	Low Turbulence Tunnel
OJF	Open Jet Facility
PLA	Polylactic acid
RANS	Reynolds-averaged Navier–Stokes
RPM	Revolutions Per Minute
TE	Trailing edge
TI	Turbulence intensity
URANS	Unsteady Reynolds-averaged Navier–Stokes
VSM	Vortex Step Method
WT	Wind tunnel
ZZ	Zig-zag

Greek Symbols

α	Angle of attack	°
α'	Uncorrected angle of attack	°
β	Compressibility correction factor	-
δ	Reflex angle	-
η	Correction factor	-
η	Location of maximum camber	-
Γ	Circulation	$\mathrm{m^2 s^{-1}}$
κ	Camber	-
Λ	Body shape factor	-
λ	Camber tension	-
ν	Kinematic viscosity	$\mathrm{m^2 s^{-1}}$
ω	Specific turbulent dissipation rate	$\mathrm{s^{-1}}$
ϕ	LE curvature	-
ρ	Air density	$\mathrm{kg m^{-3}}$
σ	Blockage factor	-
σ	Standard deviation	-
θ	Zigzag tape angle	°

Latin Symbols

ΔC_d^*	Wake buoyancy correction	-
μ	Dynamic viscosity	N
Re	Reynolds number	-
A_m	Effective model area	$\mathrm{m^2}$
A_w	Test section area	$\mathrm{m^2}$
b	Span	m
c	Chord length	m
C_d	Drag coefficient	-
C'_d	Uncorrected drag coefficient	-
C_f	Skin friction coefficient	-
$C_\mathrm{l,meas}$	Lift coefficient obtained from pressure measurements	-
C_l	Lift coefficient	-
C'_l	Uncorrected lift coefficient	-
C_m	Moment coefficient	-
C'_m	Uncorrected moment coefficient	-
$C_\mathrm{p,frac}$	Fractional pressure coefficient from total-	
$C_\mathrm{p,l}$	Pressure coefficient lower side	-

$C_{\mathrm{p,R}}$	Resultant pressure coefficient	-
$C_{\mathrm{p,tot}}$	Total pressure coefficient	-
$C_{\mathrm{p,u}}$	Pressure coefficient upper side	-
C_{p}	Pressure coefficient	-
c_{x}	Location of maximum camber	-
c_{y}	Camber	-
k	Turbulent kinetic energy	$\mathrm{m^2 s^{-2}}$
L	Characteristic length	m
L	Lift force	N
L_{x}	Lift force x-component	N
L_{y}	Lift force y-component	N
M	Mach number	-
p	Pressure	$\mathrm{kg m^{-1} s^{-2}}$
q_0	Dynamic pressure	$\mathrm{kg m^{-1} s^{-2}}$
S	Surface area	$\mathrm{m^2}$
t	Thickness	m
U_∞	Free-stream velocity	$\mathrm{m s^{-1}}$
U_{a}	Apparent wind velocity	$\mathrm{m s^{-1}}$
U_{x}	x-component of the velocity	$\mathrm{m s^{-1}}$
U_{y}	y-component of the velocity	$\mathrm{m s^{-1}}$
V	Free-stream velocity	$\mathrm{m s^{-1}}$
w	Zigzag tape width	m
$x_{\mathrm{tr,corr}}$	Corrected location of transition	m
x_{tr}	Location of transition	m
y^+	Non-dimensional wall distance	-
z	Wake rake height	m

1

Introduction

In recent years, various airborne wind energy (AWE) concepts have emerged. AWE systems generate electricity using freely flying systems or tethered flying devices, which are connected to the ground by one or more tethers [1]. Compared to conventional wind turbines, AWE systems offer significant advantages: they can reduce material usage by up to 90% and lower costs by around 50% [1]. Moreover, AWE systems can operate at higher altitudes, where winds are stronger and more consistent.

One of the promising AWE concepts is developed by Kitepower [2], which uses a leading-edge inflatable (LEI) kite. The kite consists of an inflatable leading edge tube supported by multiple chordwise struts. A canopy, a thin fabric, spans between the struts to complete the wing surface. The kite is controlled by bridle lines connected to a control pod, also referred to as the kite control unit (KCU). The bridle lines attached to the leading edge are called power lines, as they carry most of the aerodynamic force. In contrast, the lines connected to the trailing edge are called steering lines, as they are primarily used to maneuver the kite [3]. Figure 1.1 shows the TU Delft V3 kite. This kite is developed by the TU Delft and later deployed and operated by Kitepower [2]. The V3 kite is a reference design used in multiple studies [3, 4, 5, 6, 7].

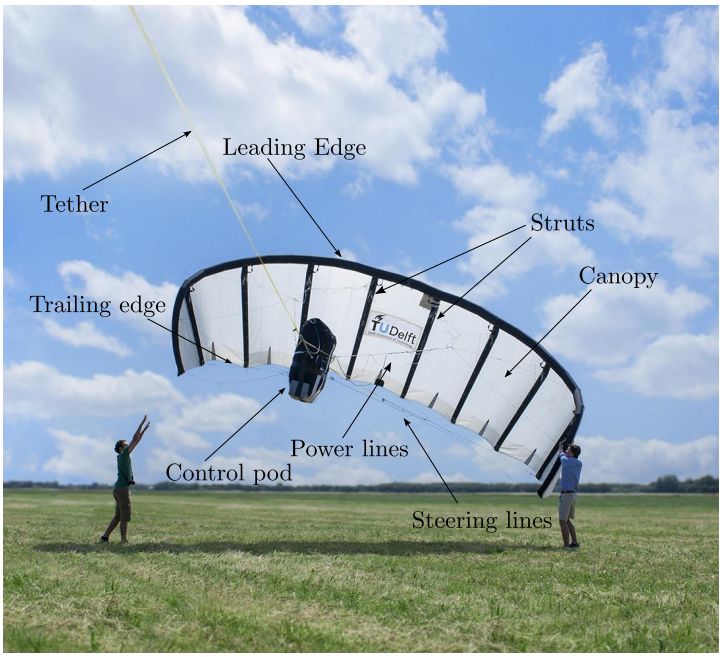

Figure 1.1: V3 kite with the different components indicated [8]

The kite operates in a pumping cycle, which consists of a traction phase and a retraction phase. During traction, the kite flies crosswind while being reeled out, generating power. In the retraction phase, the angle of attack is reduced to depower the kite, minimizing the energy required to reel it back in. After retraction, the cycle restarts. The flight path during this cycle is illustrated in Fig. 1.2. The crosswind flight concept was originally introduced by M. Loyd in 1980 [9].

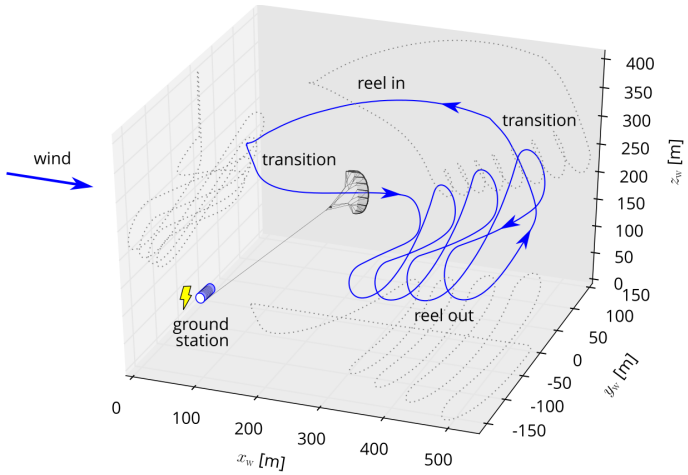

Figure 1.2: Flight path of a pumping kite power system by Fechner [10]

The LEI kites are so-called soft kites, which can deform under load. This means that the aerodynamic forces change the shape of the kite, which in turn changes the forces. This coupling problem is called a fluid-structure interaction (FSI) problem. Multiple high-fidelity models have been constructed, which couple a finite element method (FEM) with computational fluid dynamics (CFD) [11]. These models are computationally expensive and impractical for efficient design exploration. This gap was filled by combining a vortex step method (VSM) [12] and a particle system model [13]. This combined framework reduced the computational cost significantly.

The VSM method developed by Cayon [12], relies on viscous two-dimensional (2D) airfoil polars to determine the local aerodynamic loading on the LEI airfoils. The polars were first obtained by use of regression analysis based on CFD data developed by Breukels [14], which only took leading edge tube thickness and maximum camber into account. As the shape of the LEI airfoil changes dynamically, a wide range of airfoil polars has to be known to increase the accuracy of the VSM. Masure [15] used CFD on LEI airfoils and developed a machine learning based regression model based on multiple shape parameters. Validating the CFD analysis from Masure [15] proved to be difficult, as there is no experimental data available on dedicated LEI airfoils.

This lack of experimental data highlights a gap in the research and motivates the following research questions:

1. What is the influence of different locations of zigzag tapes on the LEI airfoil polars?
2. What is the influence of different Reynolds-numbers on a LEI airfoil polar?
3. Does numerical analysis capture the aerodynamic characteristics of LEI airfoils?
4. What characterises the flowfield topology around a LEI airfoil?
5. What is the influence of zigzag tapes on the flowfield topology around a LEI airfoil?

This research aims to create the basis of experimental analysis of LEI airfoils by performing a wind tunnel analysis in the low turbulence tunnel (LTT) at the TU Delft. The goal is to gain a better understanding of the flow topology around LEI. Next to this, the results can be used to validate the CFD results of Masure [15].

This report is structured as follows. In Ch. 2, the background information on LEI airfoil aerodynamics, parametrising of LEI airfoils, and experimental research will be given. In Ch. 3, the methodology behind

the design of the LEI airfoil scale models is explained as well as the simulation setup for CFD analysis. Chapter 4, the experimental setup is explained, including all the testing equipment. The different test cases performed in the LTT will be given in Ch. 5. Chapter 6 provides the steps taken to calculate the correction factors due to testing in a wind tunnel. The results will be shown in Ch. 7. At last, the key findings and recommendations for future work are described in Ch. 8.

2

Literature study

This chapter will give an overview of the available literature on leading edge inflatable (LEI) kites. First an introduction to the aerodynamics of LEI kites will be given in Sect. 2.1. Then, in Sect. 2.2, a new method of modelling LEI kites is explained. In Sect. 2.3, more information is given about parameterising LEI airfoils, CFD analysis on LEI airfoils, and the influence of a transition model. At last, the experimental research on models approximating LEI airfoil is given in Sect. 2.4.

These sections give an overview of what is known, but also provide a gap within this current research, which this thesis aims to fill. In Sect. 2.5, the research objective is formulated as well as the research questions guiding this thesis.

2.1. Leading edge inflatable kite aerodynamics

This section will explain more about the aerodynamics of LEI kites. First, the flight conditions of the V3 kite are discussed in Sect. 2.1.1. Second, the aerodynamics of the kite as a whole are discussed in Sect. 2.1.2. Then, the aerodynamics of LEI airfoils are discussed in Sect. 2.1.3.

2.1.1. LEI kite flight conditions

During the pumping cycle, the kite encounters a range of inflow conditions while executing complex manoeuvres. Due to its flexible structure, the shape of the kite constantly changes, making it challenging to accurately model its aerodynamic behaviour. Oehler et al. [16] conducted in-flight measurements on the V3 kite using pitot tubes and wind vanes mounted to the bridle lines. These instruments enabled measurements of angle of attack, side-slip angle, and apparent wind velocity.

Oehler et al. [16] found that during the traction phase, the angle of attack varied between $6°$ and $16°$, with an apparent wind velocity of $U_\mathrm{a} = 18\,\mathrm{ms}^{-1}$. In the retraction phase, the angle of attack ranged from $-8°$ to $4°$, with wind speeds below $15\ \mathrm{ms}^{-1}$. Over the full cycle, U_a ranged from $3\ \mathrm{ms}^{-1}$ to $26\ \mathrm{ms}^{-1}$, corresponding to Reynolds numbers between $\mathrm{Re} = 5 \times 10^5$ and $\mathrm{Re} = 4.5 \times 10^6$. The side-slip angle remained small during straight flight but varied up to $\pm 10°$ during turning manoeuvres. Since the kite continuously deforms, the chord length also changes, which affects the accuracy of pitot measurements and Reynolds number calculations.

Cayon et al. [17] performed an in-flight test as well. Here, the angle of attack was measured during two pumping cycles. Cayon et al. found that the angle of attack remains fairly constant throughout the traction and retraction. This suggests that the kite maintains pitch stability around a certain trim angle. The mean angle of attack measured during traction and retraction is $\alpha = 8°$ and $\alpha = 2°$, respectively. During flight, the Reynolds number varied between $\mathrm{Re} = 2.3 \times 10^6$ and $\mathrm{Re} = 4.6 \times 10^6$ based on the apparent wind speed and a chord length of $2.6\,\mathrm{m}$.

2.1.2. Flexible membrane kite aerodynamics

As said, LEI kites are made from flexible membranes, whose shape continuously adapt during flight. This flexibility can be advantageous in various ways. Studies on flexible membrane wings [18, 19, 20, 21] show that their aerodynamic behaviour differs significantly from that of rigid wings.

One key benefit is that aerodynamic forces actively reshape the membrane, dynamically adjusting the effective camber. This can suppress boundary layer separation, allowing flexible wings to reach higher lift coefficients. However, this also leads to more abrupt stall behaviour. This is clearly shown in Fig. 2.1, where different battens correspond to different stiffness levels. The most flexible configuration, single-batten, achieves the highest lift coefficient but also shows the most sudden stall.

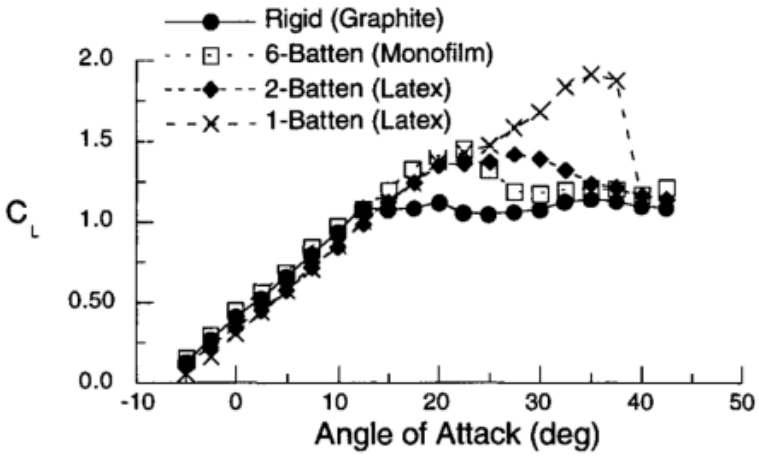

Figure 2.1: Lift polars of rigid and flexible wings [20]

Modelling flexible membrane kites becomes difficult as both structural deformations and aerodynamic loads have to be taken into account. The aerodynamic forces on the kite will alter the shape of the kite, which in turn changes the aerodynamic forces on the kite. In Sect. 2.2, current models on the so-called aero-structural coupling problems will be discussed.

2.1.3. LEI airfoil aerodynamics

Before the entire kite can be modelled. The aerodynamics of a LEI airfoil has to be explained. Figure 2.2 shows a schematic drawing of the flow topology and pressure distribution over a LEI airfoil. The suction side resembles that of a conventional airfoil, featuring a laminar boundary layer that may separate due to high adverse pressure gradients. The high adverse pressure gradient results in flow separation, after which the flow transitions to a turbulent state and eventually reattaches. This is a laminar separation bubble. Further downstream, the boundary layer can separate, resulting in trailing edge separation. The trailing edge separation becomes more pronounced when the angle of attack is increased.

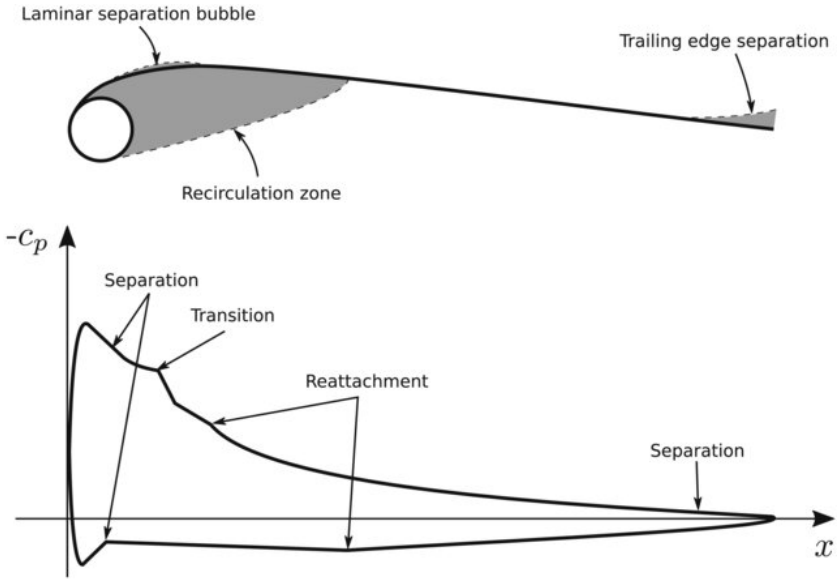

Figure 2.2: Flow topology and pressure distribution around a LEI airfoil [22]

However, the flow around the leading edge tube behaves differently. Its circular shape causes flow separation and thus creates a recirculation zone directly behind it. The size of this zone depends on both the angle of attack and the Reynolds number. The Reynolds number along the leading edge tube is significantly smaller than for the entire airfoil. The characteristic length of the leading edge tube is the diameter, whereas the characteristic length of the airfoil is the chord length. In the present work, the chord-length-to-leading-edge-diameter ratio is approximately 10. This means that the Reynolds number over the leading edge tube is one magnitude lower than for the airfoil [22]. With a low Reynolds number, the boundary layer over the leading edge tube is laminar. This laminar boundary layer separates earlier than a turbulent boundary layer, resulting in a larger low-pressure wake behind the leading edge tube. This low-pressure wake increases the pressure drag significantly. Because a turbulent boundary layer carries more momentum, it can remain attached to the surface for longer, which reduces the wake size while maintaining a higher base pressure. This reduces the pressure drag and thus the drag coefficient [23]. This shift in separation point downstream and the resulting reduction in the drag coefficient is called a drag crisis. The influence of the state of the boundary layer on the wake around a cylinder is visualised in Fig. 2.3.

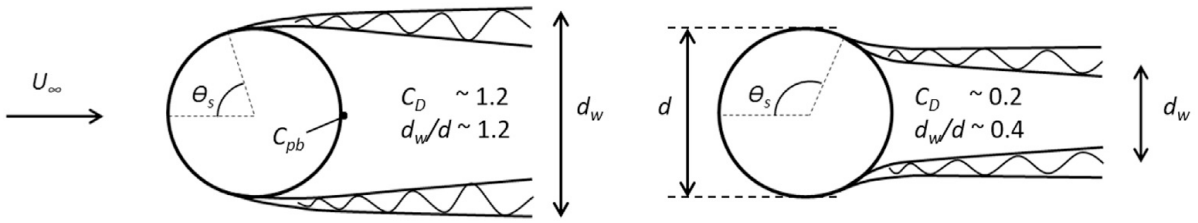

Figure 2.3: Schematic drawing of the wake with a laminar (left) and turbulent (right) boundary layer [23]

2.2. LEI kite modelling

A method to simulate the aero-elasticity of a softwing kite is by simulating the fluid-structure interaction (FSI). FSI couples a finite element method (FEM) with a computational fluid dynamics (CFD) solver, applying a robust mesh deformation method [11]. The aerodynamic model computes the forces, which are passed to the structural model, producing a deformed shape. This new geometry is then input back into the aerodynamic model. This loop is repeated until the solution converges.

These so-called aero-structural models are highly accurate but also computationally expensive, making

them less suitable for design optimisation, where many kite configurations must be evaluated. For this reason, lower-fidelity models are often used to approximate the structural and aerodynamic behaviour of the kite. One major advantage of low-fidelity models is that they allow computations to be performed faster than real-time, which means that the kite's flight path can be predicted during operation. Cayon et al. [12] developed such a low-fidelity aero-structural model. This section explains more about the aerodynamic model used, as well as how this model is integrated with a structural model of the V3 kite.

One way of solving fluid flow problems is by assuming potential flow. This approach assumes an ideal, incompressible, and inviscid fluid, which greatly simplifies the governing equations and significantly reduces computational cost. Using this method, the flow around an airfoil is represented by multiple vortices, each inducing velocity in the flow field according to the Biot–Savart law. The lift generated by such a vortex can be described by the Kutta–Joukowski theorem, given in Eq. 2.1.

$$L = -\rho U_\infty \Gamma \tag{2.1}$$

Potential flow methods are both fast and sufficiently accurate, making them a good candidate for use in low-fidelity aerodynamic models within aero-structural frameworks.

One of these models is the vortex step method (VSM), also known as the Weissinger method. The version used here is based on work by Jonkman [24] and Damiani [25], building on earlier work by Ranneberg [26]. The VSM has proven to be robust and computationally efficient, while still providing accurate results, even for geometries with low aspect ratios and high anhedral angles [12]. The VSM discretises the wing into a series of horseshoe vortices, each with its own vortex strength. To compute these strengths, an initial guess is made. Based on this guess, the induced velocity at each quarter-chord point is calculated. Using the resulting induced velocity and the free-stream velocity, the angle of attack at each control point is determined. With the help of 2D viscous airfoil polars, the lift coefficient for each section is found. This lift coefficient is then used to calculate the total lift, after which the Kutta–Joukowski theorem is applied again to find the resulting vorticity. The new vorticity is compared with the initial guess, and if the values are within a certain margin, the system is considered to have converged. If not, a new iteration is performed using relaxation factors.

The structural model developed by Poland [13] is used to model the deformation. Poland discretised the wing into nine different segments, separated by the struts of the kite. Poland assumes that the shape of the wing is largely defined by the geometry of the bridle line system.

For the aerodynamic discretisation, the V3 kite was divided into 54 segments, resulting in six segments per structural section as defined by Poland [13]. The full discretisation of the V3 kite, including the location of the control points, is shown in Fig. 2.4.

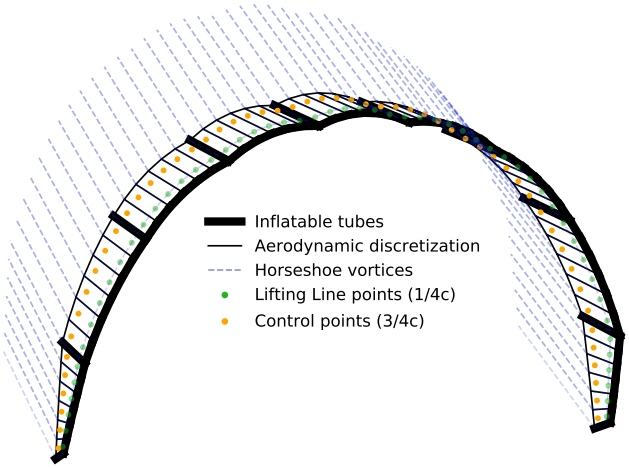

Figure 2.4: Aerodynamic model of the V3 kite with coarse discretization [27]

To account for the nonlinear behaviour of the lift coefficient, the VSM uses 2D viscous airfoil polars. These are taken from a study by Breukels [14], where the lift polar was generated using polynomial regression based on CFD results that varied the angle of attack, maximum camber, and airfoil thickness. For simplicity, Cayon et al. [12] assumes that the chordwise deformation of the airfoils does not change. This means that the maximum camber and thickness remain constant throughout the iterations.

After performing a simulation at sideslip angle $\beta = 0$, the results were compared to a RANS simulation performed by Lebesque [6]. The resulting lift and drag curves from the VSM method are shown in Fig. 2.5.

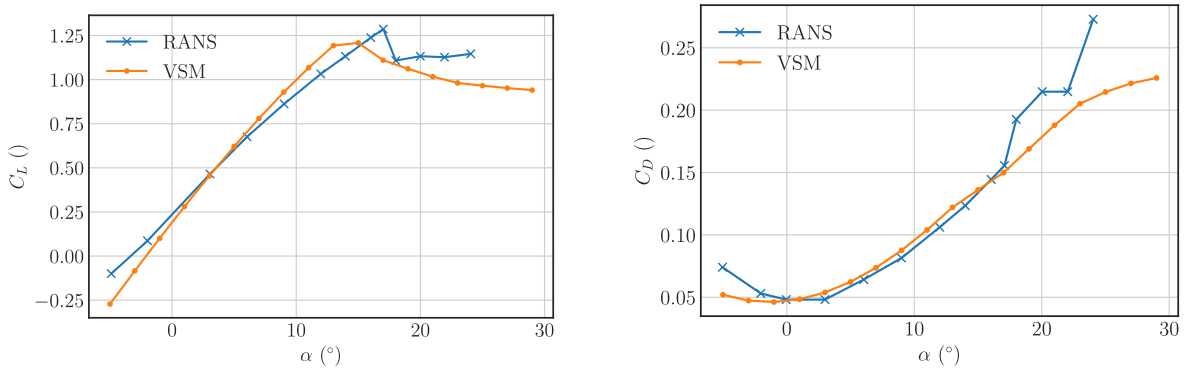

Figure 2.5: Reconstructed airfoil polars based on the VSM method [27]

From this figure, it becomes clear that the lift curve follows the linear region of the RANS results quite well. Interestingly, the slope of the lift curve is slightly steeper than that of the RANS simulation. The drag curve also shows good agreement, which is notable considering that lower-fidelity models generally struggle with drag prediction. For both lift and drag, the behaviour after stall differs, which is expected since the VSM is not valid beyond the stall angle. Cayon [27] suspects that the 2D polars from Breukels [14] might contribute to the differences between the VSM and RANS results. This will be discussed further in Sect. 2.4.1.

2.3. Simulating airfoil aerodynamics

As mentioned earlier, Breukels constructed polynomial models for the lift and drag coefficients of LEI airfoils using regression analysis based on three key parameters: airfoil thickness, maximum cam-

ber, and angle of attack. In recent years, several improvements have been made to this regression modelling by incorporating additional geometric descriptors, leading to more accurate and versatile 2D airfoil polars. This section starts by discussing recent improvements in geometric parameterisation in Sect. 2.3.1. In Sect. 2.3.2, the current CFD analysis will be discussed as well as the influence of transition on the CFD results.

2.3.1. Parametrising LEI airfoils

Over the past few years, more parameters have been added to describe a wider range of LEI airfoil shapes. These enhancements are necessary to obtain more flexible lift polynomials that can be used in aerodynamic models such as the VSM in the aero-structural framework developed by Cayon [12].

There is no universally accepted equation-based description of LEI airfoil shapes. Earlier studies by Folkersma et al. [22], Deaves [28], and Sachdeva [29] relied on spline interpolations of coordinate points, likely exported from SurfPlan™, a CAD tool widely used in surf kite design [30]. However, the limited availability of SurfPlan coordinate files and the narrow variety of profiles derived from splines necessitated a more flexible and reproducible parameterisation method, similar to conventional airfoils like the NACA series.

To address this, Breukels developed a parametric model to describe LEI airfoils using two geometric parameters: thickness t and camber κ. These quantities were adopted in later studies, including those by van Kappel [31] and Berens [8]. The geometric framework defined by van Kappel is visualised in Fig. 2.6. A similar geometric framework was proposed earlier by den Boer [19] but focused on sailing airfoils. This geometric framework can be seen in Fig. 2.7.

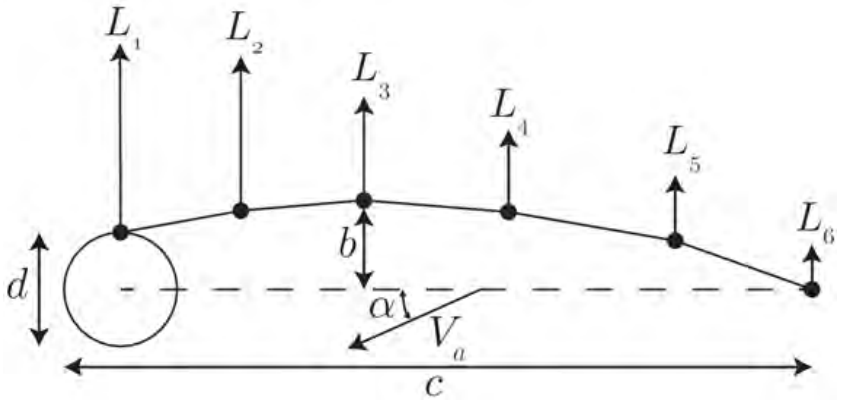

Figure 2.6: Side view of a LEI airfoil section [31]

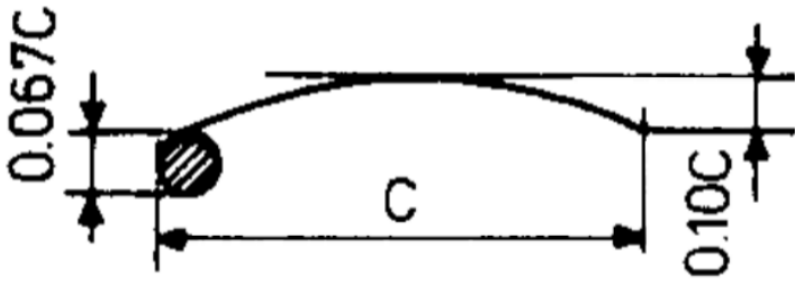

Figure 2.7: Side view of a LEI airfoil section by den Boer [19]

In both frameworks, t and κ are defined as functions of the chord length c where $t = \frac{d}{c}$ and $\kappa = \frac{b}{c}$. A notable inconsistency appears in the definition of the maximum canopy height b. van Kappel

[31] aligned the trailing edge with the center of the leading edge tube, a convention also followed by SurfPlan. In contrast, Breukels adopted the definition used by den Boer [19], where the trailing edge is horizontally aligned with the front of the leading edge.

To stay consistent with SurfPlan conventions, Watchorn [32] built further on van Kappel's framework. In addition, Watchorn introduced a third geometric parameter, the location of maximum camber η, to increase the flexibility of the airfoil design. This was motivated by experimental findings from den Boer [19], who observed that the position of maximum camber in a flexible membrane airfoil shifts forward with increasing angle of attack. The updated parameter set t, κ, and η is illustrated in Fig. 2.8.

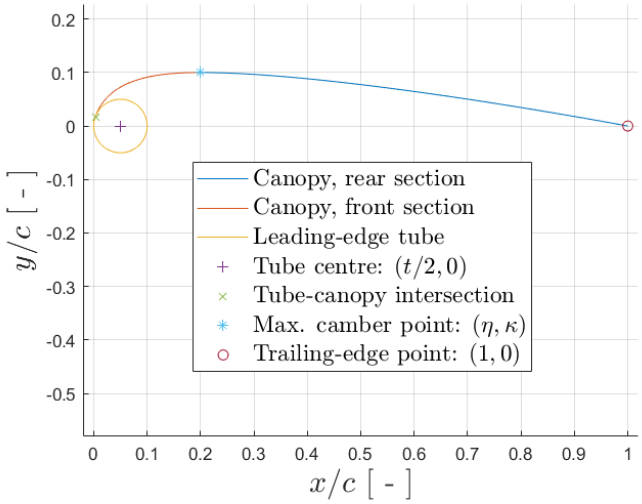

Figure 2.8: Side view of a LEI airfoil section by Watchorn [32] (t = 0.1, κ = 0.1, η = 0.2)

More recently, Corentin [33] added the reflex angle to the LEI airfoil parameterisation. For larger kites, this angle helps prevent the kite from flying too far overhead (zenith), which can lead to a loss of apparent wind or front stall. The reflex angle generates a positive moment, increasing the angle of attack and enhancing lift, thereby preventing nose stall. The reflex angle is visualised in Fig. 2.9.

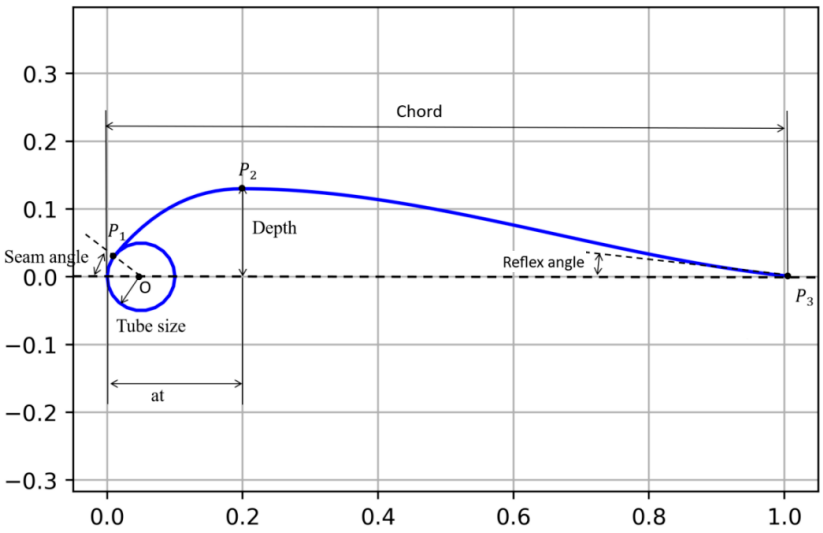

Figure 2.9: Side view of a LEI airfoil showing a reflex angle [33]

In Fig. 2.9, the seam angle is also indicated. This is the angle on the leading edge tube where the

canopy is stitched to the tube. In the models by Watchorn [32] and Corentin [33], the seam angle is fixed at $20°$ and $35°$, respectively. Masure [15] observed that the seam angle should vary with changes in leading edge thickness and camber location. He proposed a new approach based on Bézier curves instead of cubic polynomials to generate the airfoil shape. This method offers better control over the smoothness of the shape through the use of control points. At the time of writing, Masure's model represents the most advanced parameterisation framework for LEI airfoils.

Masure's model uses six different parameters to describe a LEI airfoil. In addition to the leading edge tube thickness t, maximum camber κ, location of maximum camber η, introduced by Watchorn, and the reflex angle δ from Corentin, Masure added two new parameters: camber tension λ and leading edge (LE) curvature ϕ. These parameters define the placement of control points used in the Bézier curve construction. An overview of all parameters is shown in Fig. 2.10. These six parameters significantly increase the flexibility in describing LEI airfoils.

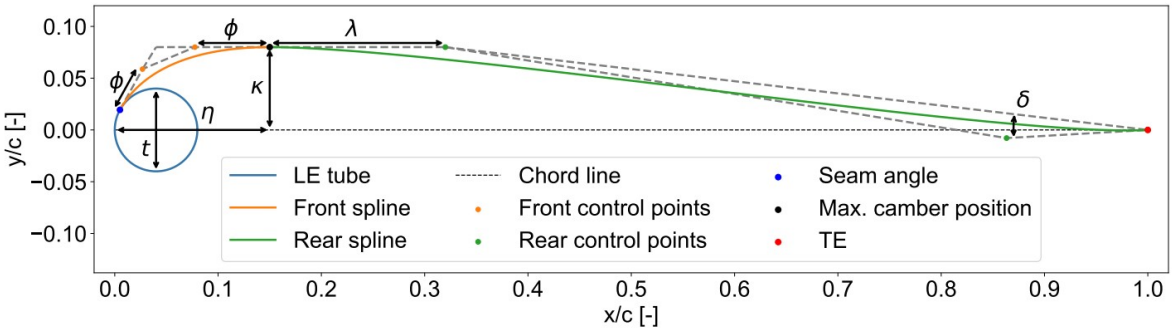

Figure 2.10: LEI kite profile parametrisation using Bézier curves and control points [15]

Table 2.1 shows the chronological development in the parametrisation of LEI airfoils.

Table 2.1: Chronological development of LEI airfoil parametrisations

Year	Author(s)	Parameters	Notes
1980	den Boer [19]	t, κ	Sailing airfoils; TE aligned with LE canopy
2011	Breukels [14]	t, κ	First LEI parametric model
2012	van Kappel [31]	t, κ	Alligns trailing edge with centre LE tube
2023	Watchorn [32]	t, κ, η	Added camber location η as camber shift with AoA
2023	Corentin [33]	t, κ, η, δ	Reflex angle δ prevents nose stall in large kites
2025	Masure [15]	$t, \kappa, \eta, \delta, \lambda, \phi$	Bézier curves, variable seam angle, ML regression

2.3.2. Airfoil CFD

One of the goals of the parametrisation of LEI airfoils is to apply regression modelling on numerical data to obtain polynomial equations expressing the aerodynamic coefficient in terms of the airfoil parameters. The numerical data is obtained by applying CFD analysis on different airfoil types. In the work of Breukels [14], Wachtorn [32], and Masure [15], Reynolds-averaged Navier-Stokes (RANS) simulation is applied. Using the RANS approach is more suitable for simulating higher Reynolds flows as all turbulent scales are modelled. This reduces computational cost significantly as neither small-scale nor large-scale turbulence is solved. RANS is also the most widely used CFD method for flow simulations due to its high computational efficiency. These studies also assumed that the boundary layer is fully turbulent, so no transition occurs in the boundary layer.

It is assumed that the stitching seam, connecting the canopy to the leading edge, may trip the boundary layer. This seam, visible in Fig. 2.11, could promote early transition. To investigate the influence of this zigzag tape, Poland [3] conducted wind tunnel tests at the open jet facility (OJF) of TU Delft [34], using a scaled V3 kite with and without zigzag tapes mimicking the seam. The zigzag tapes did influence the

aerodynamic performance, though it is still unclear whether the boundary layer is already fully turbulent during flight.

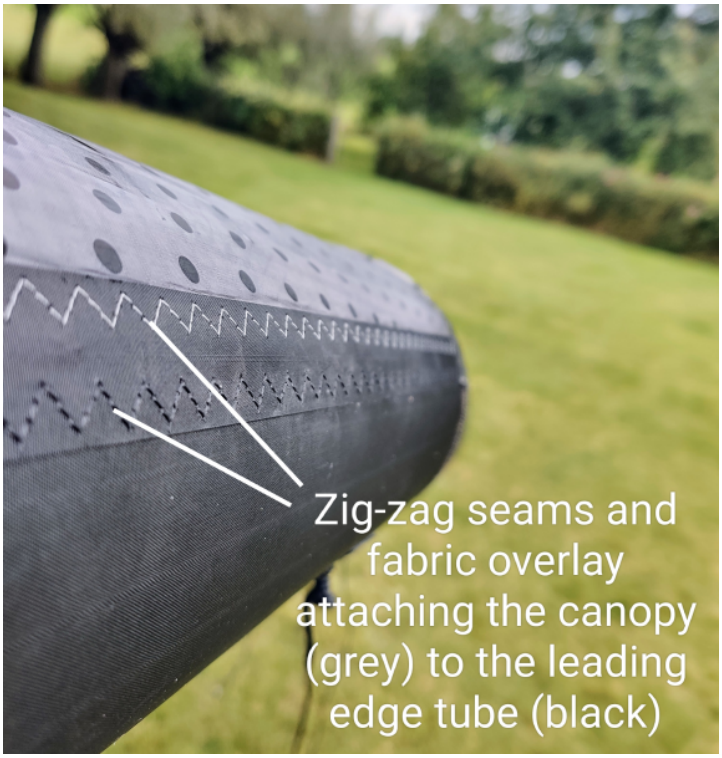

Figure 2.11: Stitching seams near the leading edge of the kite [15]

To gain a better understanding of the difference in airfoil polars with and without a transition model, Folkersma [35] modelled a LEI airfoil, assuming a fully turbulent boundary layer, but also using a $\gamma - \tilde{\mathrm{Re}}_{\theta_t}$ transition model. The CFD analysis is performed on a LEI airfoil. In Fig. 2.12 and Fig. 2.13, the results of the lift and drag coefficient can be seen for the analysis without and with the transition model, respectively.

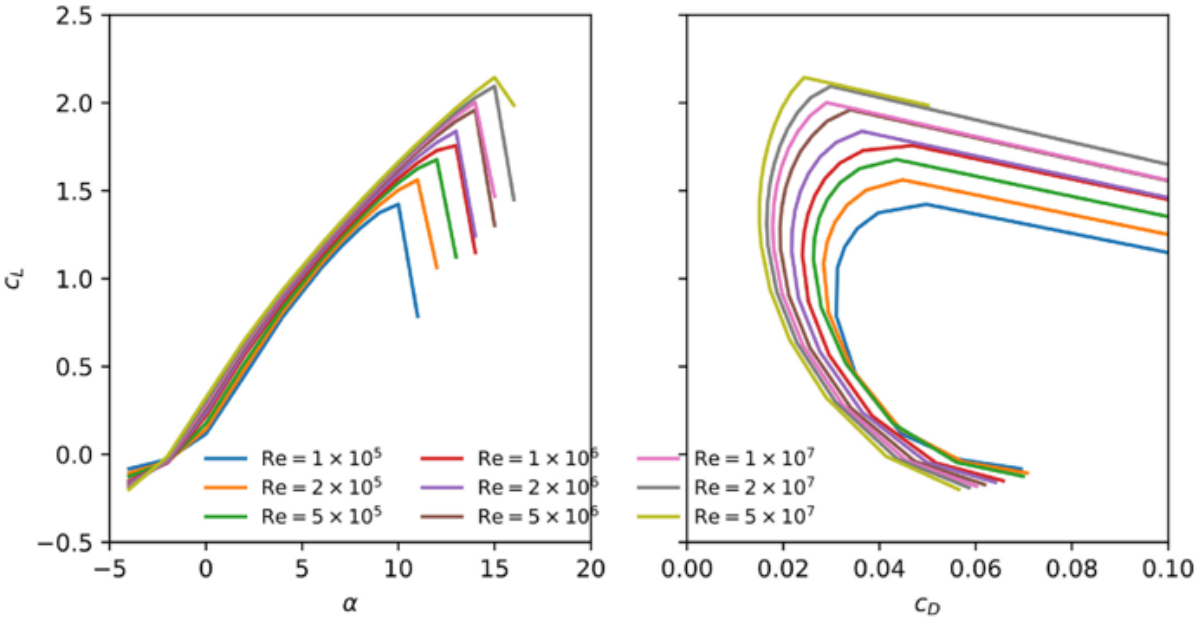

Figure 2.12: C_l-α curve (left) and C_l-C_d curve (right) for a LEI airfoil for varying Reynolds number without transition model [35]

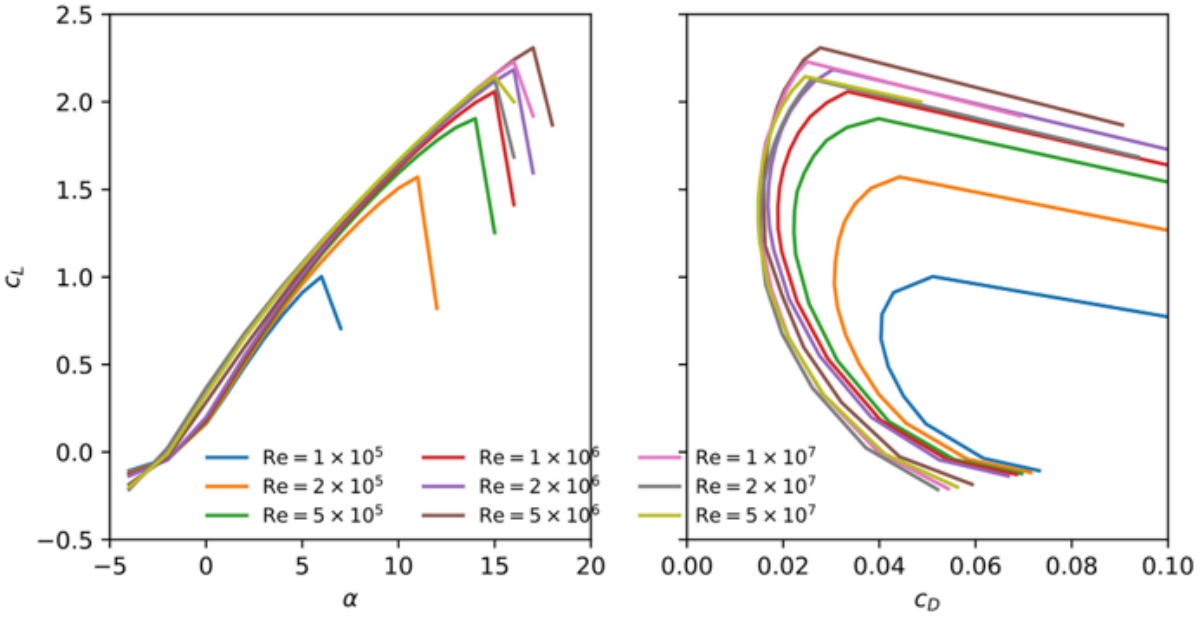

Figure 2.13: C_l-α curve (left) and C_l-C_d curve (right) for a LEI airfoil for varying Reynolds number with transition model [35]

These figures show that for $\mathrm{Re} = 10^5$, the aerodynamic performance, including the transition model, is worse than assuming a fully turbulent flow. This is due to the formation of a long laminar separation bubble. Doubling the Reynolds number to $\mathrm{Re} = 2 \times 10^5$ increases the aerodynamic performance significantly. As the boundary layer transitions into a turbulent boundary layer, it in turn delays separation. This increases the stall angle. If the Reynolds number is increased beyond $\mathrm{Re} = 2 \times 10^7$, the aerodynamic performance is similar as the flow naturally transitions to a turbulent flow at the front of the airfoil. These figures highlight the importance of considering the transition effect at Reynolds numbers below $\mathrm{Re} = 2 \times 10^7$.

2.4. Experimental methods

Up until now, there has not been experimental research focused on LEI airfoils. However, this does not mean that there has not been similar experimental research. Bruining [36] performed research in the LTT [37] on curved plates, which are used on windmills. Slow-running four-bladed windmills were extensively used to pump water in the Netherlands. The blades had a tube mounted at 25% chord position to mount the blades to the horizontal axis. Bruining [36] wanted to change the position of this tube to different locations to see what the aerodynamic improvements would be. A few of the tested setups can be seen in Fig. 2.14.

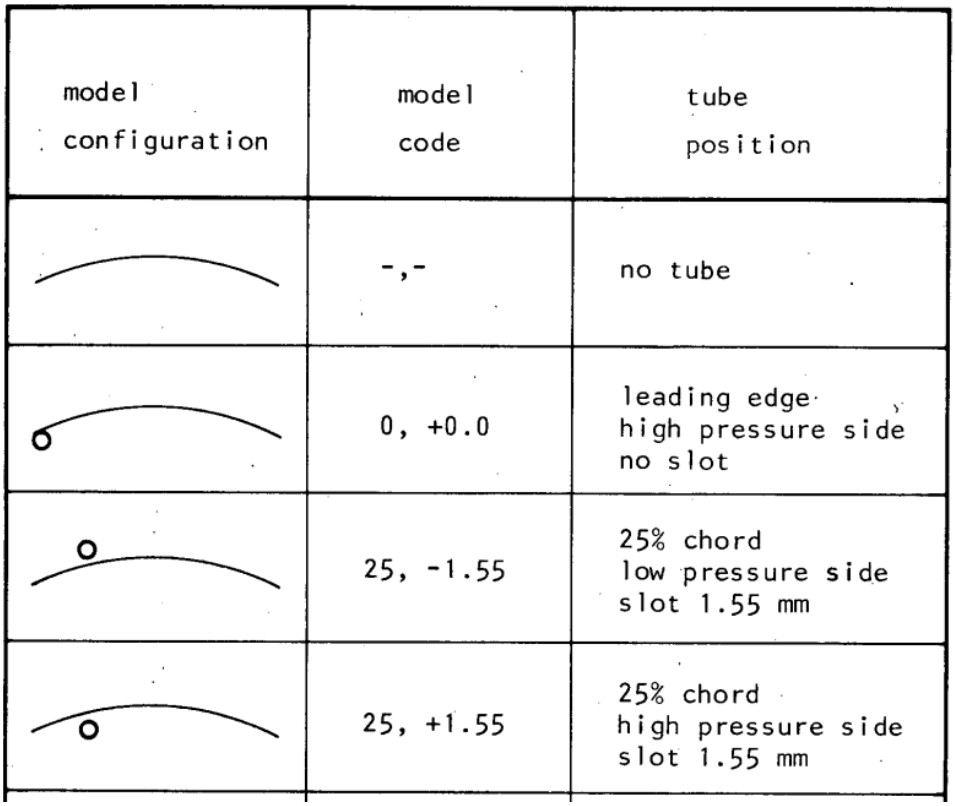

Figure 2.14: Different models which Bruining [36] tested in the LTT [37]

From this figure, the Model code ”0, +0.0” represents a LEI airfoil somewhat accurately. The leading edge tube and canopy are not materially connected, which results in a small hole between these two components. The airfoil has been tested at $\mathrm{Re} = 6 \times 10^4$ and $\mathrm{Re} = 10^5$.

den Boer [19] performed an experimental study on the low-speed aerodynamic characteristics of a two-dimensional sail wing with adjustable slack of the sail. In this study, the tested sails are used in hang gliders as well as in the sail rotor of windmills. The tested model consisted of a cylindrical bar that could be rotated around its own axis. Attached to this bar was a sail. By turning the cylindrical bar, the tension in the sail could be adjusted to change the shape. The side view of the model can be seen in Fig. 2.15. This model represents the LEI airfoils in kites more closely. The difficulty of using den Boer’s [19] results as validation for numerical models lies in the flexibility of the model. The CFD analysis is based on 2D-rigid airfoils. Den Boer found in his experiments that, when wind speeds increase, the location of maximum camber shifts towards the leading edge. Therefore, the shape is constantly changing and thus not suitable for validating CFD results.

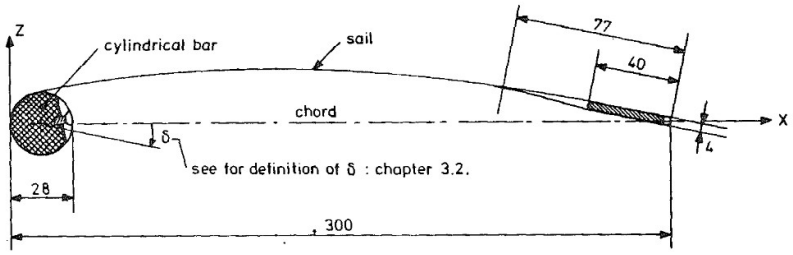

Figure 2.15: Sideview of the wind tunnel model by den Boer [19]

2.4.1. Experimental vs numerical data

Folkersma, as said before, has constructed a numerical method to analyse 2D LEI airfoils with CFD. To validate his model, the model case ”0, +0.0” by Bruining [36] has been analysed in his CFD model and compared to the experimental results. The downside is that the leading-edge tube and the curved plate in the experimental test are not materially joined, which results in a tiny hole between the two components. Folkersma [35] adjusted the input model to the model shown in Fig. 2.16.

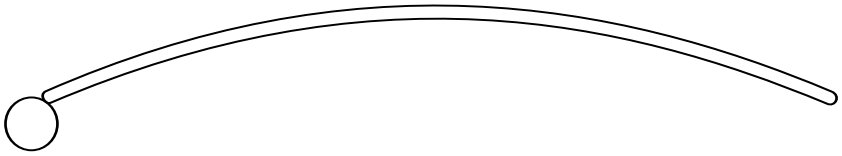

Figure 2.16: CFD model tested by Folkersma [35]

After running the CFD analysis at $\mathrm{Re} = 10^5$, assuming a fully turbulent flow and the flow including a transition model, the results were compared to the experimental results of Bruining [36]. The comparison can be seen in Fig. 2.17

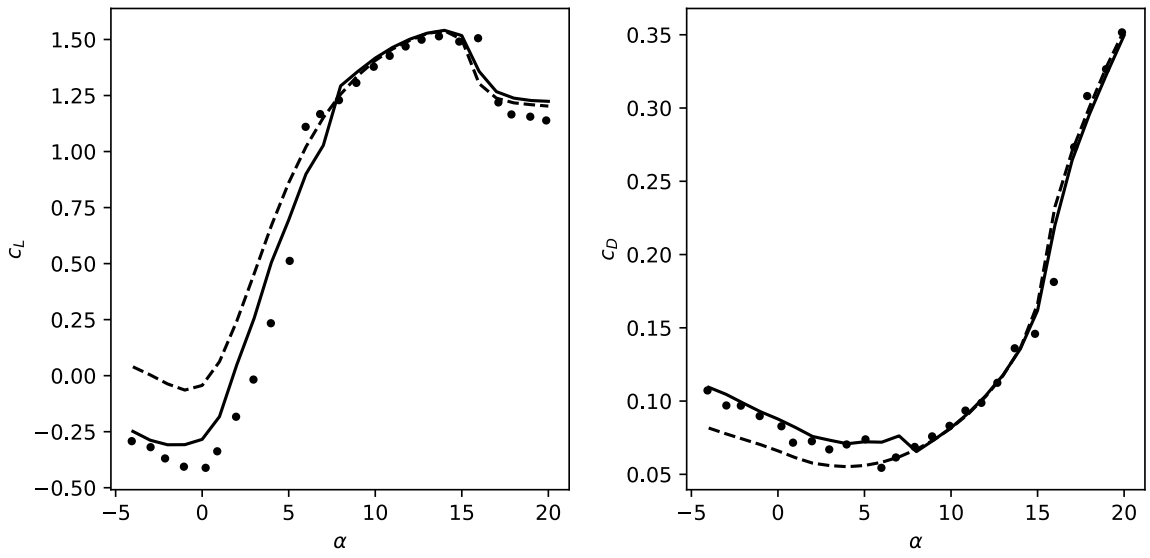

Figure 2.17: Lift (left) and drag (right) coefficients of model by Bruining [36]. The experimental results are shown as black dots, the simulation results with the transition model are shown as a solid line, and the results without the transition model as a dashed line [35]

In this figure, the black dots are the data points from Bruining [36]. The solid and dashed lines are the CFD results with and without the transition model. The simulations with the transition give a more ac-

curate representation of the results than the simulations without the transition model. The experimental data validate the numerical method created by Folkersma.

In the study of Cayon [27], a comparison is made between CFD analysis of Breukels [14], the RANS simulation with and without transition model of Folkersma [35], and experimental results of den Boer [19]. The comparison can be seen in Fig. 2.18

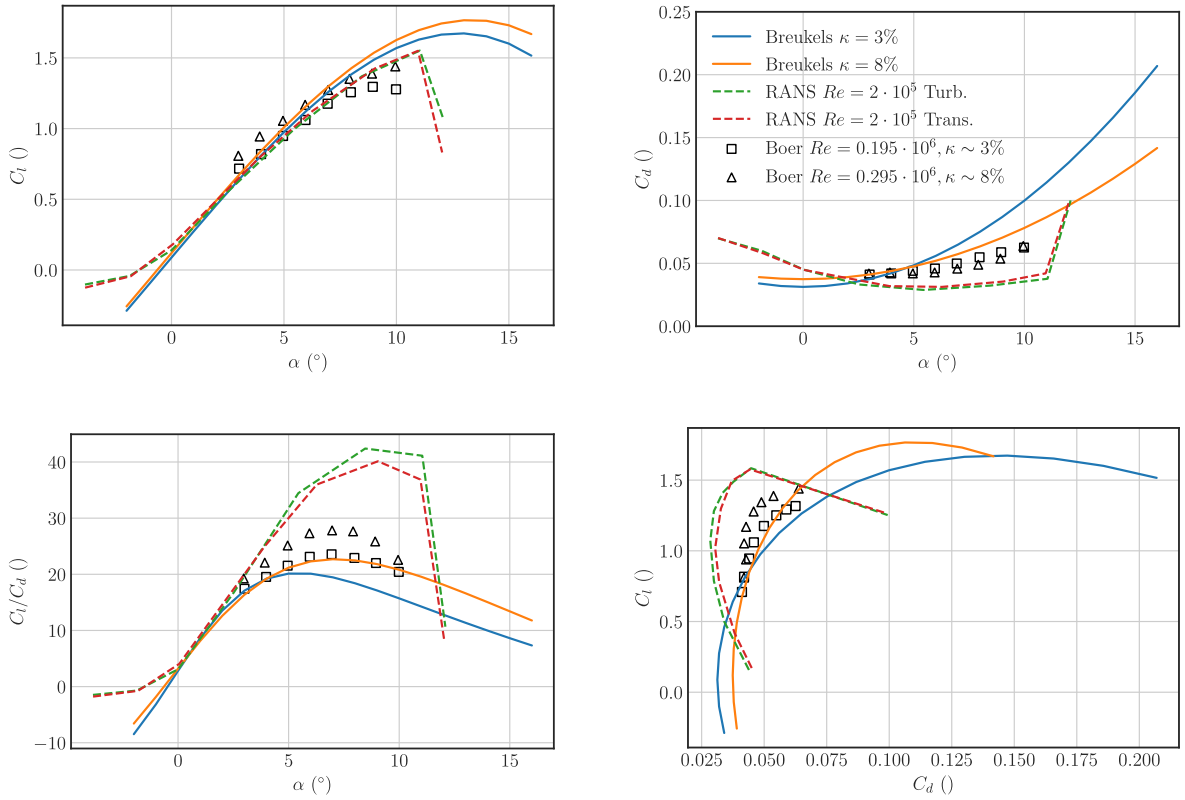

Figure 2.18: Comparison of airfoil data of a LEI airfoil. Experimental data [19] is shown by markers, RANS simulations by Folkersma [35] by dashed lines and Breukels's regression modeling [14] by continuous lines [27]

Looking at the lift curve from this figure, it becomes clear that the results obtained by Breukels [14] have a steeper lift slope and a lower lift coefficient at zero angle of attack with respect to the experimental data. The data from Folkersma [35] has a better match with the experimental results. This steeper lift slope can also explain the discrepancy found in Fig. 2.5. The VSM method constructed by Cayon [12] is based on the airfoil polars from Breukels [14] and could therefore have a steeper lift curve.

The drag curve in Fig. 2.18 shows that the simulation results by Breukels [14] match the experimental results. This match also correlates to the match in the drag coefficient of Fig. 2.5.

2.5. Research questions

The literature study focused on LEI kite aerodynamics, kite modelling techniques, and experimental tests on LEI-like airfoils. No experimental research has been carried out specifically on 2D-rigid LEI airfoils. Such data is needed to better understand boundary layer development around these airfoils and can also serve to validate CFD results. Once validated, the regression model for airfoil polars can be integrated into the VSM model by Cayon. Including a wider range of airfoil shapes will improve the accuracy of modelling the flight path of LEI kites.

From this, a research objective can be concluded and formulated as stated below:

> "*To perform experimental and numerical analysis of the aerodynamic performance of a 2D rigid LEI airfoil*"

Based on this research objective, the following research question can be drawn up

> "*What are the aerodynamic characteristics of a 2D rigid LEI airfoil*"

This research question is divided into smaller sub-questions, each contributing to addressing the main research question. These sub-questions are stated as follows:

1. What is the influence of different locations of zigzag tapes on the LEI airfoil polars?
2. What is the influence of different Reynolds-numbers on a LEI airfoil polar?
3. Does numerical analysis capture the aerodynamic characteristics of LEI airfoils?
4. What characterises the flowfield topology around a LEI airfoil?
5. What is the influence of zigzag tapes on the flowfield topology around a LEI airfoil?

3

Methodology

This chapter will cover the methodology behind the sizing of the wind tunnel models. Next to this, the computational fluid dynamics (CFD) setup for the numerical analysis will be explained. First, technical specifications of the wind tunnel facility are given in Sect. 3.1. Second, the model sizing is explained in Sect. 3.2. The CFD setup will be given in Sect. 3.3.

3.1. Wind tunnel

The wind tunnel, which will be used to perform the experiment, is the low turbulence tunnel (LTT) of Delft University of Technology. The LTT is a closed-throat single-return wind tunnel. The dimensions of the entire wind tunnel are enormous, as the wind tunnel is built in a 3-story building. The fan and engine are located on ground level. The settling chamber and test section are on the second floor. The wind tunnel is powered by a six-bladed fan, which is driven by a 525 kW DC motor. This combination will give the wind tunnel a maximum velocity of $120\,\mathrm{ms}^{-1}$ in the test section. The maximum Reynolds number that can be achieved is roughly $\mathrm{Re} = 3.5 \times 10^6$.

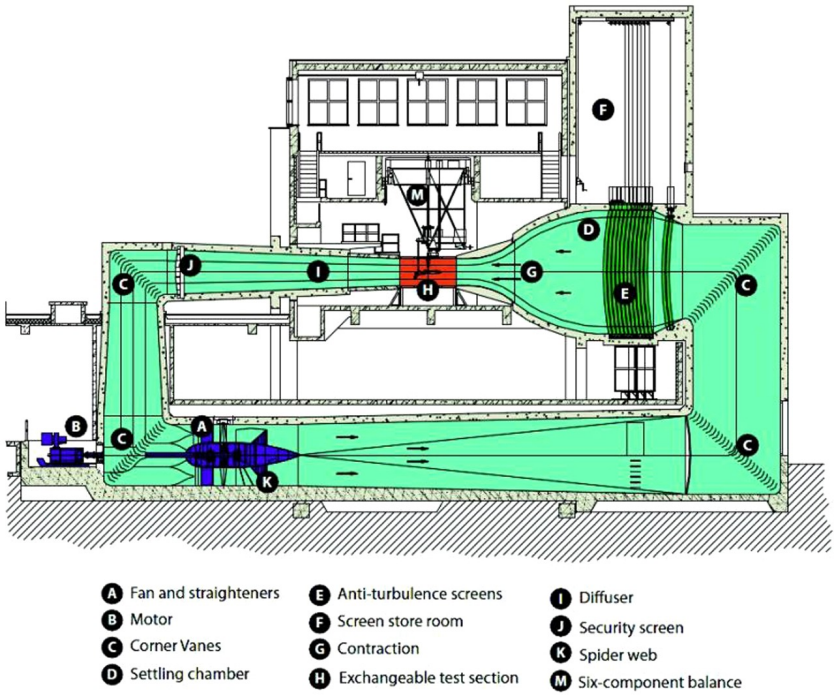

Figure 3.1: Schematic drawing of the LTT at the TU Delft [38]

In Fig. 3.1, a schematic drawing of the LTT can be seen. The flow is driven by the six-bladed fan at (A). From here, the flow is guided along two corners to the second floor by the turning vanes (C), where it enters the settling chamber (D). Here, the flow velocity is low as the area of the tunnel is increased. In the settling chamber, the flow quality is increased by the use of the anti-turbulence screens (E). These screens will ensure that the velocity distribution in the tunnel is uniform and the turbulence levels are reduced. This improvement in flow quality is done in the settling chamber to reduce losses as the flow speeds are low. To increase the flow velocity, the wind tunnel contracts at (G) after which the flow enters the test section (H). After the test section, the flow enters the diffuser (I) to reduce the airspeeds, which will reduce the losses in the wind tunnel. At last, the flow is again guided by the corner vanes to the ground floor, where the cycle is repeated.

Due to the large contraction ratio of the wind tunnel of 17.8, the free-stream turbulence in the test section is reduced significantly. The free-stream turbulence at $20\ \mathrm{ms}^{-1}$ is 0.015% and 0.07% at $75\ \mathrm{ms}^{-1}$.

3.2. Model design

To design the two wind tunnel models, first, the coordinate system has to be defined. This will be done in Sect. 3.2.1. Second, the airfoil shapes will be determined in Sect. 3.2.2. Third, the outer dimensions of the models will be determined in Sect. 3.2.3. Fourth, the canopy thickness will be calculated in Sect. 3.2.4. At last, the construction process of the model will be given in Sect. 3.2.5

3.2.1. Coordinate system

The coordinate system used in defining the airfoil is represented in Fig. 3.2 and Fig. 3.3. As the airfoil will be mounted vertically in the wind tunnel test section, the coordinate system is as follows:

- The x-axis points downstream of the wind tunnel test section
- the y-axis points vertically inside the wind tunnel test section.
- The z-axis runs laterally inside the wind tunnel test section

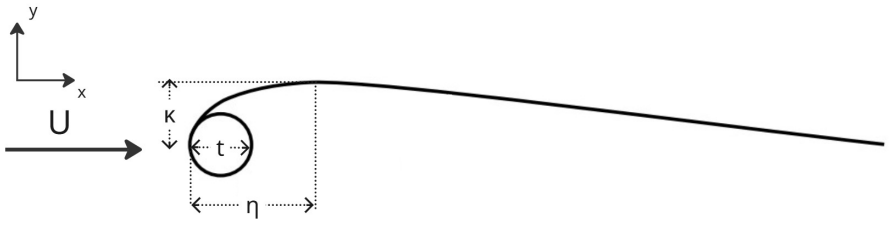

Figure 3.2: Schematic drawing of the sideview of a LEI airfoil

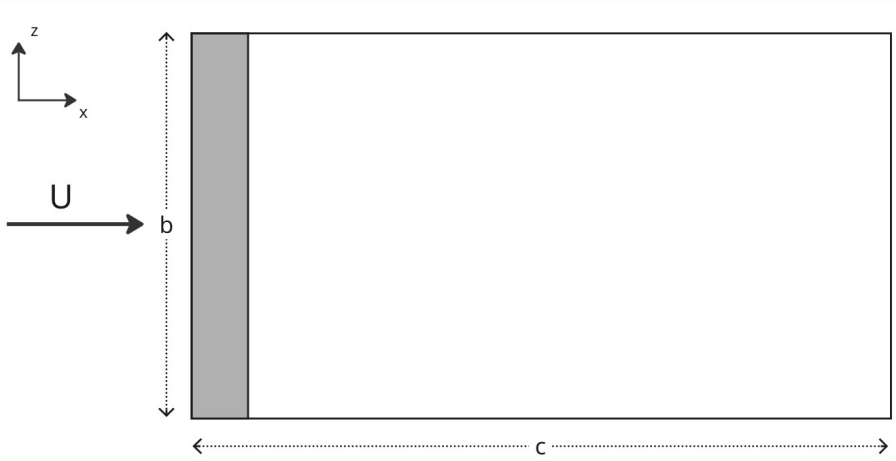

Figure 3.3: Schematic drawing of the topview of a LEI airfoil

In Fig. 3.2, three shape parameters are shown. The leading edge tube thickness t, maximum camber κ, which is also referred to as c_{y}, and maximum camber location η, also referred to as c_{x}. In Fig. 3.3, the chord length c is shown as well as the span b. The forces acting on the airfoil will be in the xz-plane. The following subsection will define the shape parameters of the two models

3.2.2. Airfoil shape

To design the models, the software developed by Siemens called SolidEdge [39] is used. This software has an integrated FEM solver, which will be used to calculate the maximum deflection when testing at $\mathrm{Re} = 2 \times 10^6$. For the experiment, two different airfoils will be tested in the LTT. One of these models will be the airfoil at midspan of the V3 kite.

V3 model

The model is parametrised using the developed software by Masure [15]. Using a DAT file containing the coordinates, the program could generate the parameters that correspond to the imported data file. The airfoil can be seen in Fig. 3.4. This model will be referred to as the V3 model.

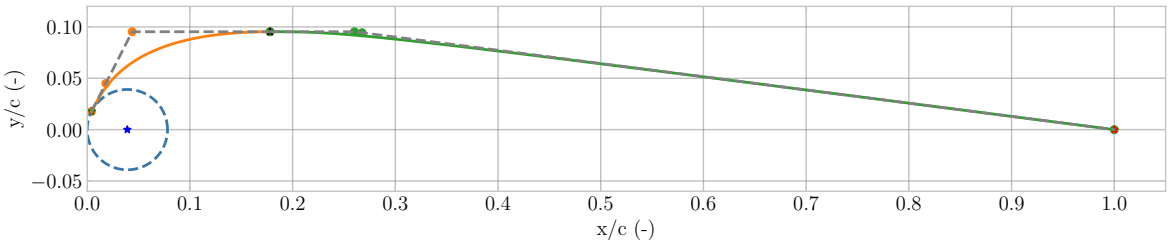

Figure 3.4: V3 airfoil at midspan

Model2

The second model is based on the results of Watchorn [32]. In Fig. 3.5, three $C_l - \alpha$ curves can be seen with a variation in the leading edge tube thickness, location of maximum camber, and maximum camber. Watchorn found that the lift coefficient increased with a smaller leading edge tube diameter, higher maximum camber, and the camber location more towards the trailing edge. The maximum camber resulting in the highest C_l, according to the figures, would be $\kappa = 0.14$. In kite design, this value is too high and therefore, the maximum camber is set to be $\kappa = 0.1$.

Using the parametrization of Masure [15] the second model is parametrized as in Fig. 3.6.

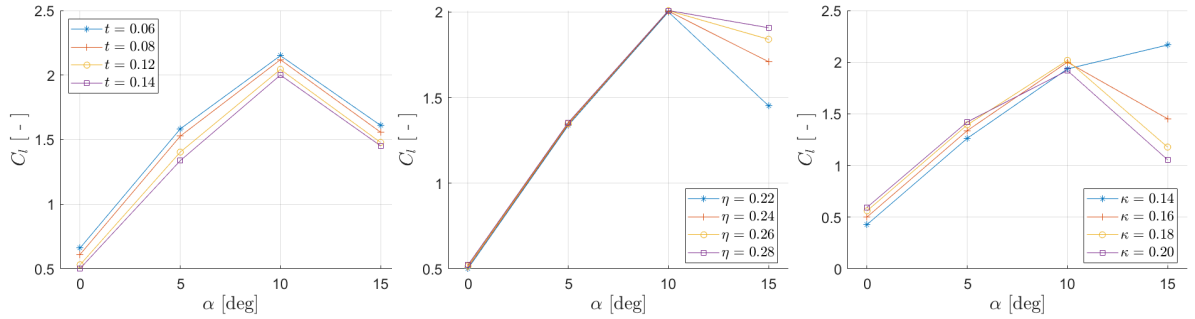

Figure 3.5: Lift polars for different leading edge thickness t (left) , maximum camber position η (middle) and maximum camber κ (right) [32]

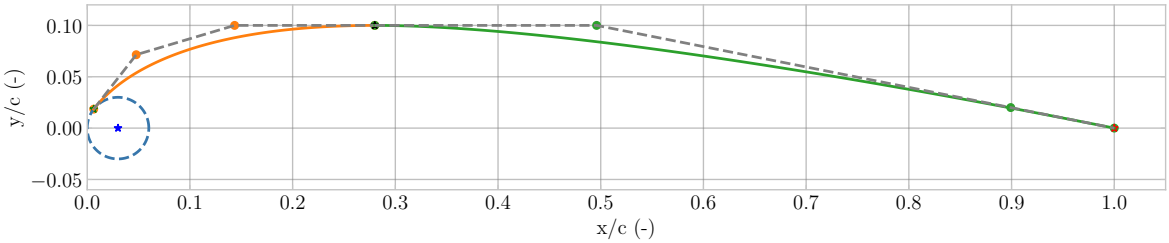

Figure 3.6: Model2 airfoil

Conclusion
In Fig. 3.7, the 2 airfoils are overlaid, which shows a clear distinction in the geometry of the airfoils. In Table 3.1, the parameters describing the airfoils are given.

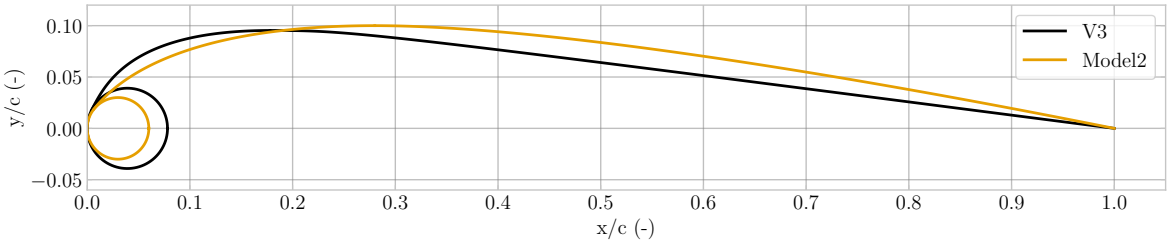

Figure 3.7: V3 model and Model2 airfoil overlay

Table 3.1: Parameters for the V3 model and Model2

Model	t (-)	η (-)	κ (-)	δ (°)	λ (-)	ϕ (-)
V3 model	0.0782	0.178	0.0953	0	0.1	0.351
Model2	0.0600	0.280	0.1000	0	0.3	0.650

The 2D shape will be extruded to form a 3D scale model. The outer dimensions for the two models will be explained in the following subsection.

3.2.3. Outer dimensions

Before constructing the model, the outer dimensions should be determined. The final dimensions of the model depend on several different key parameters. These parameters will be discussed in this subsection, after which a conclusion will be drawn for the final outer dimensions.

Test section size

The test section of the LTT is an octagon which is $1.80\,\mathrm{m}$ wide, $1.25\,\mathrm{m}$ high, and $2.60\,\mathrm{m}$ long. On top of the test section, there is a turntable to which will set the angle of attack of the airfoil. Because the turntable is at the top of the test section, this means that the model will be attached vertically instead of horizontally. To ensure that the scale model will not move during testing, the scale model will be attached to the floor and ceiling of the test section. This means that the span of the model will be $1250\,\mathrm{mm}$. To make sure the models will fit. It is advised that $2\,\mathrm{mm}$ clearance is kept. Therefore, the final span of the model will be $1248\,\mathrm{mm}$

Pressure tabs on wall

In order to measure the lift coefficient of the LEI airfoil, strips of pressure tabs will be installed on the walls of the wind tunnel. These strips will capture the pressure footprint created by the model on the test section walls. This pressure footprint extends to infinity upwind and downwind, which makes it impossible to capture the entire footprint. The pressure strips on the wall have a total length of $2.4\,\mathrm{m}$ and therefore, require a correction factor to obtain the entire pressure field. How this correction factor is calculated will be explained in Ch. 6. For now, it is important to understand that increasing the chord length of the model will increase the uncertainty of the calculated correction factor, as a larger part of the pressure footprint has to be modelled. In the work of de Tavernier [40], an experiment in the LTT is performed withe the pressure strips. In her experiment the models have a chord length of $0.6\,\mathrm{m}$. Therefore, the assumption is made that all chord lengths below $0.6\,\mathrm{m}$ are acceptable. Opting for a smaller chord length does increase the accuracy of the pressure measurements, but it will reduce the achievable Reynolds numbers.

Reynolds number

The Reynolds number is an important parameter with respect to aerodynamics and wind tunnel experiments. The Reynolds number provides insight into the nature of the flow, whether it is laminar or turbulent. The Reynolds number is the ratio between the inertial forces and viscous forces in a fluid flow. It is crucial to keep the Reynolds number similar to full-scale operations, as the aerodynamic properties like lift, drag, and boundary layer behaviour will be similar. This will also ensure that the acquired data from the wind tunnel is relevant and applicable to real-world scenarios. The formula for the Reynolds number can be seen in Eq. 3.1

$$Re = \frac{\rho U L}{\mu} \tag{3.1}$$

In this equation ρ is the air density in $\mathrm{kgm^{-3}}$, U the free-stream velocity in $\mathrm{ms^{-1}}$, L the characteristic length in m, and μ the dynamic viscosity in Pas. The characteristic length L will be the chord length of the model. During the retraction phase, the kite encounters Re numbers around $\mathrm{Re} = 10^5$ to $\mathrm{Re} = 7.5{\times}10^5$. On the other hand, during the traction phase of the kite, the encountered Re numbers are in the order of $\mathrm{Re} = 10^6$ to $\mathrm{Re} = 10^8$ [22]. Therefore, it is preferable that the Re number during testing falls within this range. As discussed before, due to the finite length of the pressure tabs, the chord length should lie below $0.6\,\mathrm{m}$. In Table 3.2, the required wind speeds are shown for different Reynolds numbers and chord lengths.

Table 3.2: Required wind speed for different Re and chord lengths.

$\mathrm{Re} \times 10^6$	$U_\infty\ (\mathrm{ms^{-1}})$			
	$c = 0.40\ (\mathrm{m})$	$c = 0.45\ (\mathrm{m})$	$c = 0.50\ (\mathrm{m})$	$c = 0.55\ (\mathrm{m})$
1	36.51	32.45	29.21	26.55
2	73.02	64.91	58.42	53.11
3	109.53	97.36	87.62	79.66

To increase the Reynolds number significantly, the wind speed can be increased. As the LTT can reach wind speeds in the test section to around $120\,\mathrm{ms}^{-1}$, the maximum theoretical Reynolds number with a chord length of $0.4\,\mathrm{m}$ will be $\mathrm{Re} = 3.2 \times 10^6$. However, due to the unusual shape of the LEI airfoil, the canopy deflects under loading, unlike conventional airfoils. This means that the loads, and therefore the wind speed, should be kept minimal in order to have an acceptable deflection in the canopy. This results in increasing the chord length as the wind speeds can be reduced. Calculating the canopy deflection will be done in Sect. 3.2.4.

Blockage factor

During the testing of the airfoil, the goal is to construct airfoil polars. Testing is done from $\alpha = -10°$ to $\alpha = 25°$. At $25°$, the frontal surface area inside the wind tunnel is significantly larger than at $0°$. In Fig. 3.8, the model can be seen inside the wind tunnel at $\alpha = 0°$ and $\alpha = 25°$.

Figure 3.8: Difference in exposed surface area of the V3 model in the LTT at $\alpha = 0°$ (left) and $\alpha = 25°$ (right)

During testing, it is assumed that there will be no time changes of wind speed in the test section and, therefore, no changes to the mass flow. If the model is at a higher angle of attack, the effective area through which this air can flow decreases. The ratio between the area of the model and the test section is called the blockage factor (BF), for which the relation can be seen in Eq. 3.2.

$$\mathrm{BF} = \frac{A_\mathrm{m}}{A_\mathrm{w}} \tag{3.2}$$

Here, A_m is the effective area of the model and A_w the area of the test section. It is advised by S. Bernardy [41] that the maximum blockage ratio stays below 15%. The octagonal test section has a height and width of $1.25\,\mathrm{m}$ and $1.8\,\mathrm{m}$ respectively. The four corner triangles making the section octagonal have two sides of $0.3\,\mathrm{m}$. This results in a test section area of $2.07\,\mathrm{m}^2$. This means that the maximum effective area of the model is $A_\mathrm{m} = 0.3105\,\mathrm{m}^2$. The effective area of the model can be calculated with Eq. 3.3 and is rewritten to solve for the chord length.

$$A_\mathrm{m} = \sin(\alpha)\, c b \quad \Rightarrow \quad c = \frac{A_\mathrm{m}}{b \sin(\alpha)} \tag{3.3}$$

Where α is the angle of attack, c is the chord length, and b is the span of the model. Filling in Eq. 3.3 with $\alpha = 25°$ gives $c = 0.5878\,\mathrm{m}$. This is the maximum chord length after which blockage effect will influence the results.

Manufacturability

At last, the manufacturability is an important aspect for sizing the model. The model should be $1248\,\mathrm{mm}$ long in the spanwise direction to span the entire test section. This means that the canopy and leading edge tube should be $1248\,\mathrm{mm}$ long. For the V3 model airfoil, the leading edge tube thickness t is 0.077. This factor results in awkward tube diameters when choosing rounded chord length such as 0.4 and $0.5\,\mathrm{m}$. Therefore, the decision is made to size the tube diameter with off-the-shelf pipe dimensions. This means that the chord length is dictated by the tube diameter. This method reduces the cost of manufacturing significantly.

Because the tube diameter of Model2 is 0.06, a rounded chord length like $0.5\,\mathrm{m}$ can be chosen, as this results in a tube diameter of $0.03\,\mathrm{m}$.

Conclusion
In the end, the final outer dimensions for the V3 model and Model2 are tabulated in Table 3.3. The V3 model chord length is driven by the tube diameter. The chord length is lower than the maximum allowable chord length for the blockage factor. Furthermore, a Reynolds number of $\mathrm{Re} = 2 \times 10^6$ can be achieved while keeping the flow velocity acceptable. At last, the chord length is shorter than the chord length used by de Tavernier [40]. Therefore, the uncertainty due to the pressure strips is acceptable. For Model2, the chord length is set at $0.5\,\mathrm{m}$, which results in a tube diameter of $0.03\,\mathrm{m}$. These dimensions are also within the limits set by the achievable Re number and maximum blockage factor. The reduction in chord length with respect to the V3 model will reduce the uncertainty of modelling the pressure distribution.

Table 3.3: Outer dimensions of the V3 model and Model2

Model	b (mm)	c (mm)	t (mm)
V3 model	1248	522	40
Model2	1248	500	30

3.2.4. Canopy thickness

After determining the outer parameters of the two models, the canopy thickness has to be calculated. Unlike a conventional airfoil, where the upper and lower surfaces meet at the leading and trailing edge, the LEI airfoil's upper surface sits freely at the trailing edge. As the experimental test will be on a rigid 2D LEI airfoil, the canopy at the trailing edge should not deform. In the previous subsection, the chord lengths for the V3 model and Model2 are set to be $0.522\,\mathrm{m}$ and $0.5\,\mathrm{m}$ respectively. To achieve the maximum desired Reynolds number of $\mathrm{Re} = 2 \times 10^6$, the wind tunnel has to operate at $57\,\mathrm{ms}^{-1}$ and $60\,\mathrm{ms}^{-1}$ respectively. These speeds will generate a significant lift force on the model, which will ultimately deform the canopy. As this is the maximum Reynolds number, the canopy thickness and material will be determined for these wind speeds.

In full-scale kites, the membrane thickness of the canopy lies around $10^{-5}c$[35]. Replicating this in a wind tunnel model is not feasible. It is desired, however, to keep the canopy thickness as thin as possible to keep the obtained data more realistic. This subsection will explain more about the generated forces during the wind tunnel test. Next to this, the different construction materials are discussed. At last, the calculated deflection will be shown for the final model dimensions.

Forces
The 2D airfoils are both analysed using Masure's model with $\mathrm{Re} = 2 \times 10^6$ [15], assuming a fully turbulent boundary layer. The resultant lift-polars can be seen in Fig. 3.9. From these figures, the maximum lift coefficient is 1.84 and 1.94, both at $\alpha = 14°$ for the V3 model and Model2, respectively. During the test, the boundary layer will most likely not be fully turbulent. Therefore, the lift coefficient is expected to be higher than these values. This is, however, a good approximation for the deflection calculation. These lift coefficients are used to determine the total lift generated by the airfoil with Eq. 3.4.

$$L = \frac{1}{2}\rho V^2 C_l S \tag{3.4}$$

In this equation, L is the total lift force in N, ρ the air density in $\mathrm{kg/m}^3$, V the free-stream velocity in ms^{-1}, C_l the non-dimensional lift coefficient, and S the surface area in m^2. The total lift for each model for $\mathrm{Re} = 10^6$ and $\mathrm{Re} = 2 \times 10^6$ is tabulated in Table 3.4.

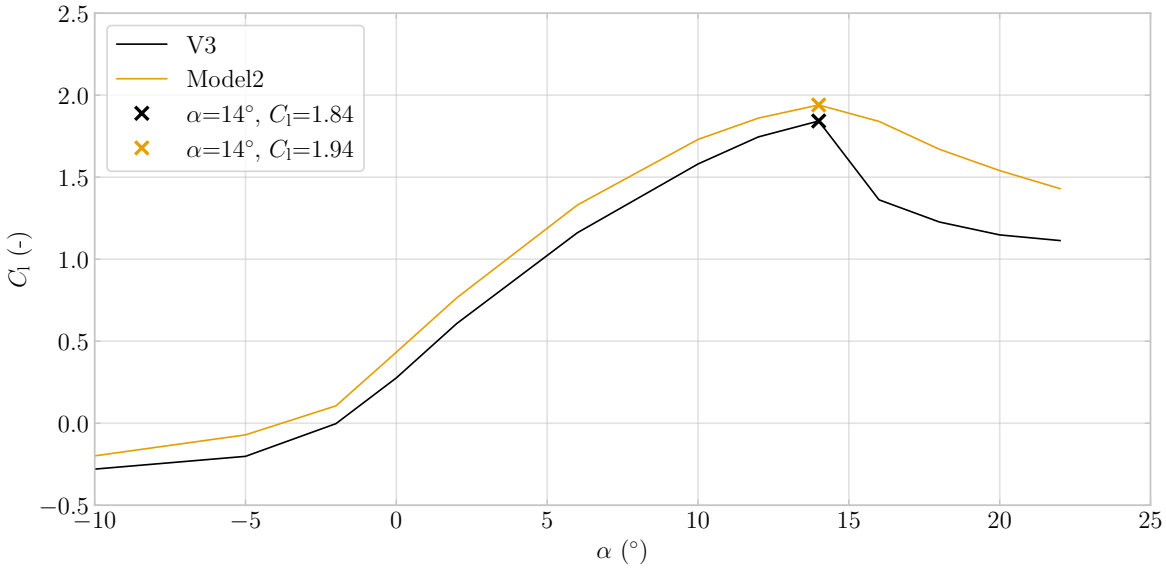

Figure 3.9: C_l vs α for two airfoils

Table 3.4: Total lift force per model at $\mathrm{Re} = 2 \times 10^6$

Model	L (N)
V3 model	2361.01
Model2	2564.50

However, the total lift over the airfoil is not uniform. The distribution of the lift force depends on the pressure distribution over the airfoil. In Fig. 3.10, the pressure distribution over the V3 airfoil at midspan and Model2 airfoil is shown at $\mathrm{Re} = 2 \times 10^6$.

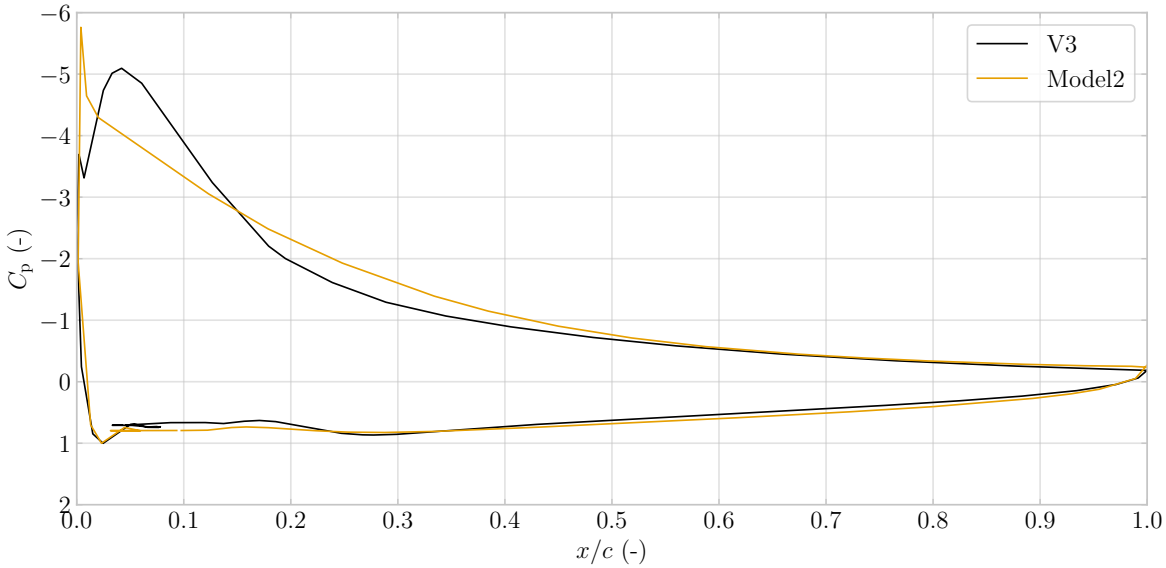

Figure 3.10: Pressure distribution for both models at $\alpha = 14°$ and $\mathrm{Re} = 2 \times 10^6$

To distribute the total lift forces over the model, the model is discretised into 10 panels. The total

pressure coefficient, $C_{\mathrm{p,tot}}$ per panel is obtained at $x/c = 0.05$,$x/c = 0.15$ to $x/c = 0.95$. $C_{\mathrm{p,tot}}$ is calculated by $C_{\mathrm{p,tot}} = C_{\mathrm{p,l}} - C_{\mathrm{p,u}}$ at each prescribed location. The $C_{\mathrm{p,tot}}$ per panel is then divided by the sum of all $C_{\mathrm{p,tot}}$ to obtain the weighted pressure coefficient per panel. This percentage is multiplied by the total lift force to redistribute the total lift force. The results for the V3 model and Model2 can be seen in Table 3.5 and Table 3.6, respectively.

Table 3.5: Load distribution V3 model at $\alpha = 14°$

x/c (-)	$C_{\mathrm{p,tot}}$ (-)	$C_{\mathrm{p,frac}}$ (-)	L at $\mathrm{Re} = 2 \times 10^6$ (N)	L_{x} (N)	L_{y} (N)
0.05	5.69	0.31	701.29	−169.66	680.46
0.15	3.44	0.19	423.98	−102.57	411.39
0.25	2.38	0.13	293.34	−70.96	284.62
0.35	1.85	0.10	228.01	−55.16	221.24
0.45	1.47	0.08	181.18	−43.83	175.80
0.55	1.18	0.06	145.44	−35.18	141.12
0.65	0.95	0.05	117.09	−28.33	113.61
0.75	0.75	0.04	92.44	−22.36	89.69
0.85	0.55	0.03	67.79	−16.40	65.77
0.95	0.23	0.01	28.35	−6.86	27.51
Total	18.49	1.00	2278.90		

Table 3.6: Load distribution Model2 at $\alpha = 14°$

x/c (-)	$C_{\mathrm{p,tot}}$ (-)	$C_{\mathrm{p,frac}}$ (-)	L at $\mathrm{Re} = 2 \times 10^6$ (N)	L_{x} (N)	L_{y} (N)
0.05	4.70	0.25	627.30	−151.76	608.67
0.15	3.52	0.19	469.81	−113.66	455.85
0.25	2.73	0.14	364.37	−88.15	353.55
0.35	2.11	0.11	281.62	−68.13	273.25
0.45	1.63	0.09	217.55	−52.63	211.09
0.55	1.29	0.07	172.17	−41.65	167.06
0.65	1.04	0.06	138.81	−33.58	134.68
0.75	0.83	0.04	110.78	−26.80	107.49
0.85	0.64	0.03	85.42	−20.66	82.88
0.95	0.40	0.02	53.39	−12.92	51.80
Total	18.89	1.00	2521.22		

At last, the maximum C_{l} is achieved at an angle of attack of 14° for both the V3 model and Model2. To obtain the correct direction of the lift force, the lift force has to be decomposed into an x and y component. This is done according to Fig. 3.11, which results in Eq. 3.5.

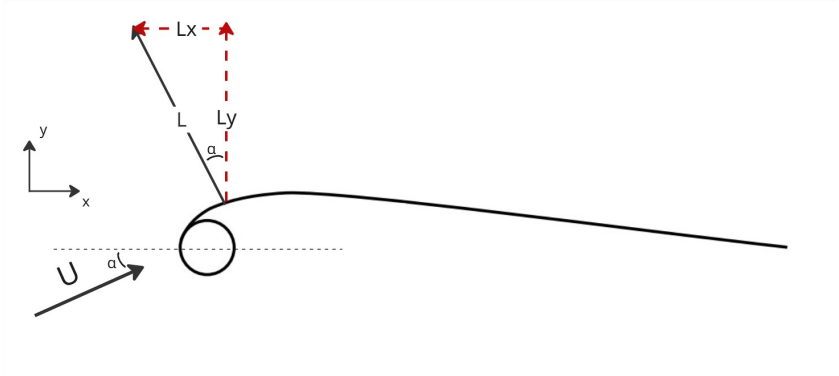

Figure 3.11: Decomposition of lift force

$$\begin{aligned} L_{\mathrm{x}} &= -\sin(\alpha) * L \\ L_{\mathrm{y}} &= \cos(\alpha) * L \end{aligned} \tag{3.5}$$

The final x and y components of the V3 model and Model2 can be seen in Table 3.5 and Table 3.6, respectively.

Materials & manufacturability
For the canopy of the LEI airfoil, three materials were considered: 3D printer plastic, aluminium and steel. The choice of material is mainly driven by the stiffness required to prevent excessive deflection during high-load test cases. The modulus of elasticity for common 3D-printed plastics such as PLA lies between 2 and $3\,\mathrm{GPa}$, while aluminium and steel have values of approximately $70\,\mathrm{GPa}$ and $200\,\mathrm{GPa}$ respectively. The difference in stiffness is significant. Using a plastic plate would result in unacceptable deformation and was therefore discarded. Aluminium offers a moderate stiffness but remains prone to deflection compared to steel. Steel, having the highest modulus of elasticity, is most suitable for maintaining the geometric integrity of the airfoil under load.

In addition to stiffness, the manufacturability of the plate imposes further constraints. The canopy must be at least $1\,\mathrm{mm}$ thick to avoid complications during welding. Welding very thin sheet metal can lead to burn-through or excessive warping. On the other hand, the thickness should not exceed $3\,\mathrm{mm}$ to ensure that the leading edge radius remains manufacturable. For the chosen leading edge tube diameter, the required radius would be too tight with a plate thickness above $3\,\mathrm{mm}$, especially if turning is used. Considering both structural and manufacturing aspects, the final decision is made to construct the canopy plate from steel. This material provides sufficient stiffness to limit deformation and offers better weldability compared to aluminium at low thicknesses.

Resultant deflection
As said before, SolidEdge [39] by Siemens is used to determine the deflection of each model. SolidEdge uses Femap in combination with Nastran, which is the most used FEM solver. Each model is fitted with a rib to suppress deflection further. The model is discretised into ten separate panels on which a uniform load is applied. These forces are in Table 3.5 and Table 3.6 for the V3 model and Model2, respectively. As the sides of the canopy and leading edge tube are attached to the test section walls, a fixation constraint is applied on these surfaces. At last, an automatic connection is made between the leading edge tube and the canopy, including the rib. In Fig. 3.12a and Fig. 3.12b, the V3 model can be seen with the constraints and connections, and the forces, respectively. With the forces acting on the airfoil known and the material from which the model will be constructed, the minimum allowable canopy thickness can be calculated. The subjective mesh size used in each FEM analysis is $8\,\mathrm{mm}$. This means that the software tries to make every cell $8\,\mathrm{mm}$, as this is sometimes not possible on curved surfaces.

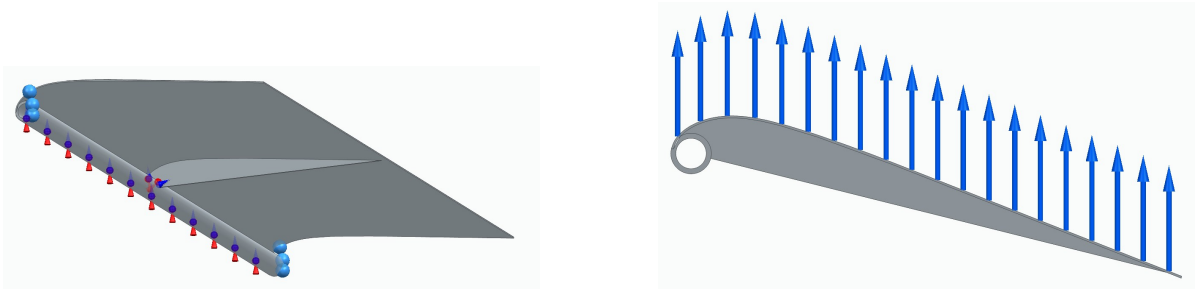

(a) Constraints on the V3 model

(b) Forces (not to scale) on the V3 model at $\alpha = 14°$

Figure 3.12: Boundary conditions on the V3 model

In this figure, the blue spheres represent the fixation constraints. The blue/red cones represent the connections, and the blue arrows represent the forces. Do note that the forces are not drawn to scale and are actually non-linearly distributed, mimicking the pressure distribution. With these boundary conditions, the FEM analysis is performed on the V3 model with a canopy thickness of 1, 2, and $3\,\mathrm{mm}$. The results can be seen in Fig. 3.13.

The displacement seen in the figures is exaggerated to provide a better visualisation. The figures of the displacement of the Model2 under maximum load for a canopy thickness of 1, 2, and $3\,\mathrm{mm}$ can be found in the appendix under Fig. A.1. The displacement results are tabulated in Table 3.7.

Table 3.7: Maximum displacement for V3 model and Model2 at $\mathrm{Re} = 2 \times 10^6$ and $\alpha = 14°$

Canopy thickness (mm)	V3 model max displacement (mm)	Model2 max displacement (mm)
1	20.50	6.83
2	3.62	2.05
3	1.81	1.12

Table 3.7 shows the maximum displacement of the V3 model and Model2 airfoils at $\mathrm{Re} = 2 \times 10^6$ and $\alpha = 14°$ for different canopy thicknesses. For the V3 model, a canopy thickness of $1\,\mathrm{mm}$ results in a maximum deflection of $20.5\,\mathrm{mm}$, which is considered too large for accurate aerodynamic testing. Increasing the thickness to $2\,\mathrm{mm}$ reduces the displacement significantly to $3.62\,\mathrm{mm}$, while a further increase to $3\,\mathrm{mm}$ only reduces it marginally to $1.81\,\mathrm{mm}$. The small difference between the $2\,\mathrm{mm}$ and $3\,\mathrm{mm}$ case does not justify the added manufacturing complexity and the reduction in manufacturability of the canopy. Therefore, the V3 model canopy thickness is set to $2\,\mathrm{mm}$. For the Model2 airfoil, the displacement at $1\,\mathrm{mm}$ is significantly lower at $6.83\,\mathrm{mm}$. This is not due to a lower aerodynamic load but most likely the result of the airfoil shape, which has more curvature than the V3 model and can therefore carry a load more efficiently. The assumption is made that a maximum deflection of $5\,\mathrm{mm}$ is acceptable during aerodynamic testing. Therefore, the canopy thickness of Model2 is set to $2\,\mathrm{mm}$

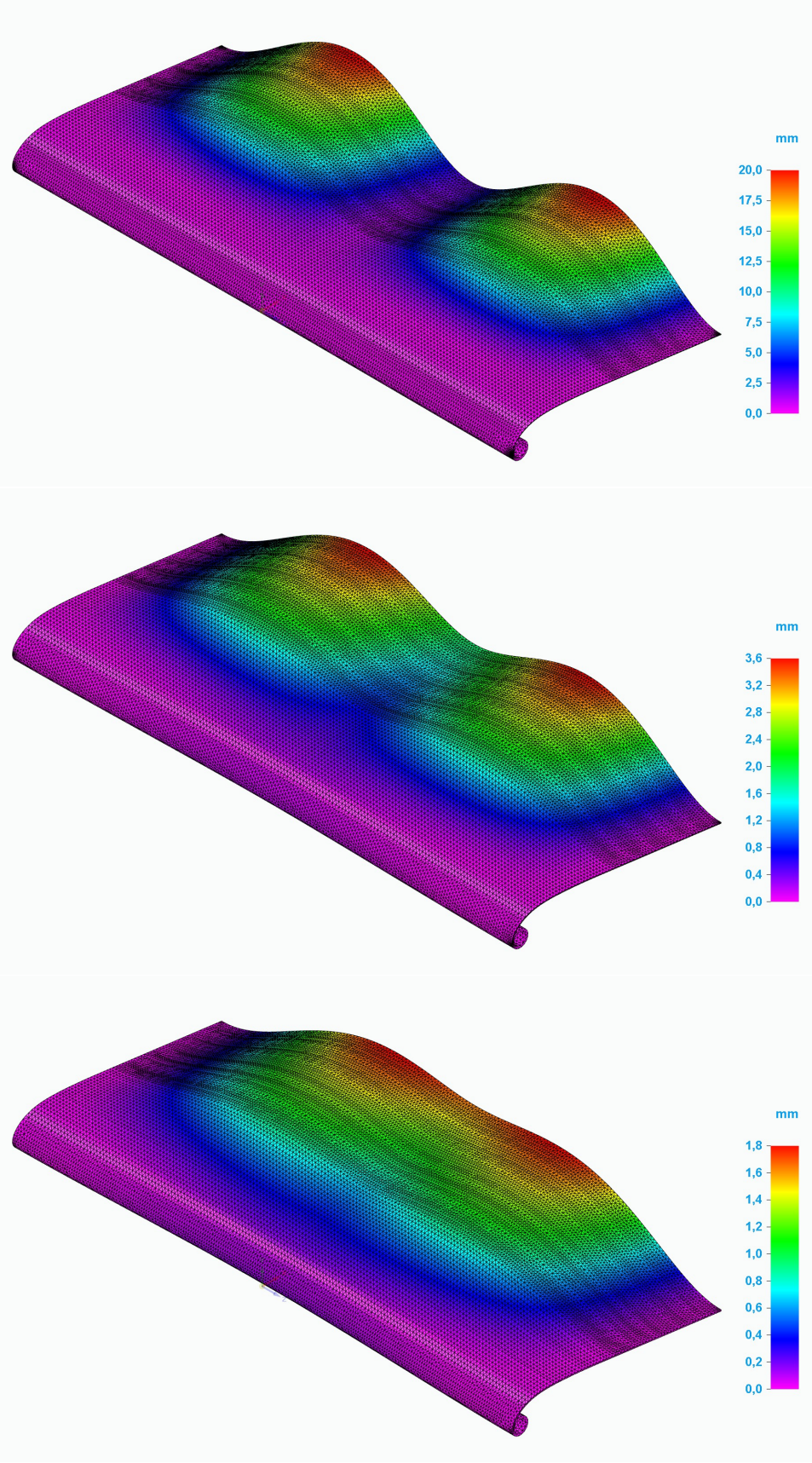

Figure 3.13: Exaggerated displacement of the V3 model at $\alpha = 14°$ and $\mathrm{Re} = 2 \times 10^6$ for different canopy thicknesses: $1\,\mathrm{mm}$ (top), $2\,\mathrm{mm}$ (middle), and $3\,\mathrm{mm}$ (bottom).

3.2.5. Model construction

With all dimensions known and the canopy thickness determined, the models can be constructed. The model can be installed in the wind tunnel on so-called ground plates. To make installation easier, side plates are added to the airfoil. These side plates are welded to the leading edge tube as well as the canopy. These sideplates will ensure that the sides of the model are fixed, as this assumption was made in the deflection calculation. The sideplate of the V3 model is $600\,\mathrm{by}\,100\,\mathrm{mm}$ with a thickness of 4mm. This means that the span of the model is reduced to $1240\,\mathrm{mm}$. The total span of the entire model will be $1248\,\mathrm{mm}$, which is required to ensure that the model fits inside the wind tunnel. As the chord length of Model2 is shorter than that of the V3 model, the sideplate is 575 by $100\,\mathrm{mm}$. This side plate is also $4\,\mathrm{mm}$ thick and thus the span of the airfoil is reduced to $1240\,\mathrm{mm}$.

The canopy will be formed using rolling to create a smooth curvature of the airfoil. To accommodate the canopy on the leading edge, a slot will be milled. This milled slot will be straight and will not follow the inside curvature of the canopy. This will make manufacturing easier. A close-up of the attachment point of the leading edge tube and the canopy can be seen in Fig. 3.14.

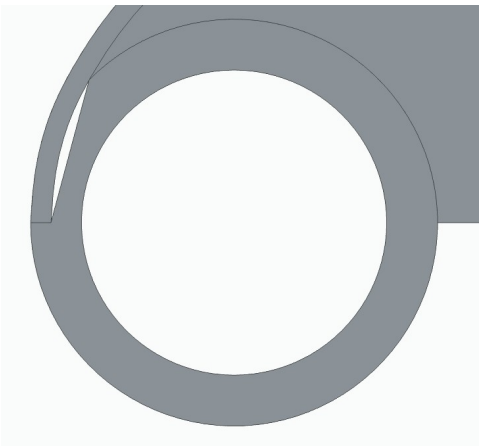

Figure 3.14: Gap between canopy and leading edge tube due to the milled slot in the leading edge tube

Welding the entire model can bring some difficulties. As said before, if the plate is too thin, burn-through can occur, which is not desired in an aerodynamic model. Next to this, warping is also a major concern. During welding, the individual parts are heated, which causes an expansion of the material. If the material cools unevenly, the residual stress in the material will cause the plate to deform [42]. For this reason, the consideration is made to assemble the model via spot welding. Instead of creating full welds along the attachment points, local spot welds are used, which minimise the heating and cooling of the canopy. This will ensure that minimal warping will occur and thus stay true to the designed dimensions.

The completed models will have to be prepped before installation in the wind tunnel test section. The model still has some imperfections in the canopy after assembly. To ensure a smooth surface, a matte black decoration foil is wrapped around the canopy and the leading edge tube. This will even out imperfections as well as aid in the infrared visualisation of the boundary layer. This will be discussed in Ch. 4. The completed models can be seen in Fig. 3.15

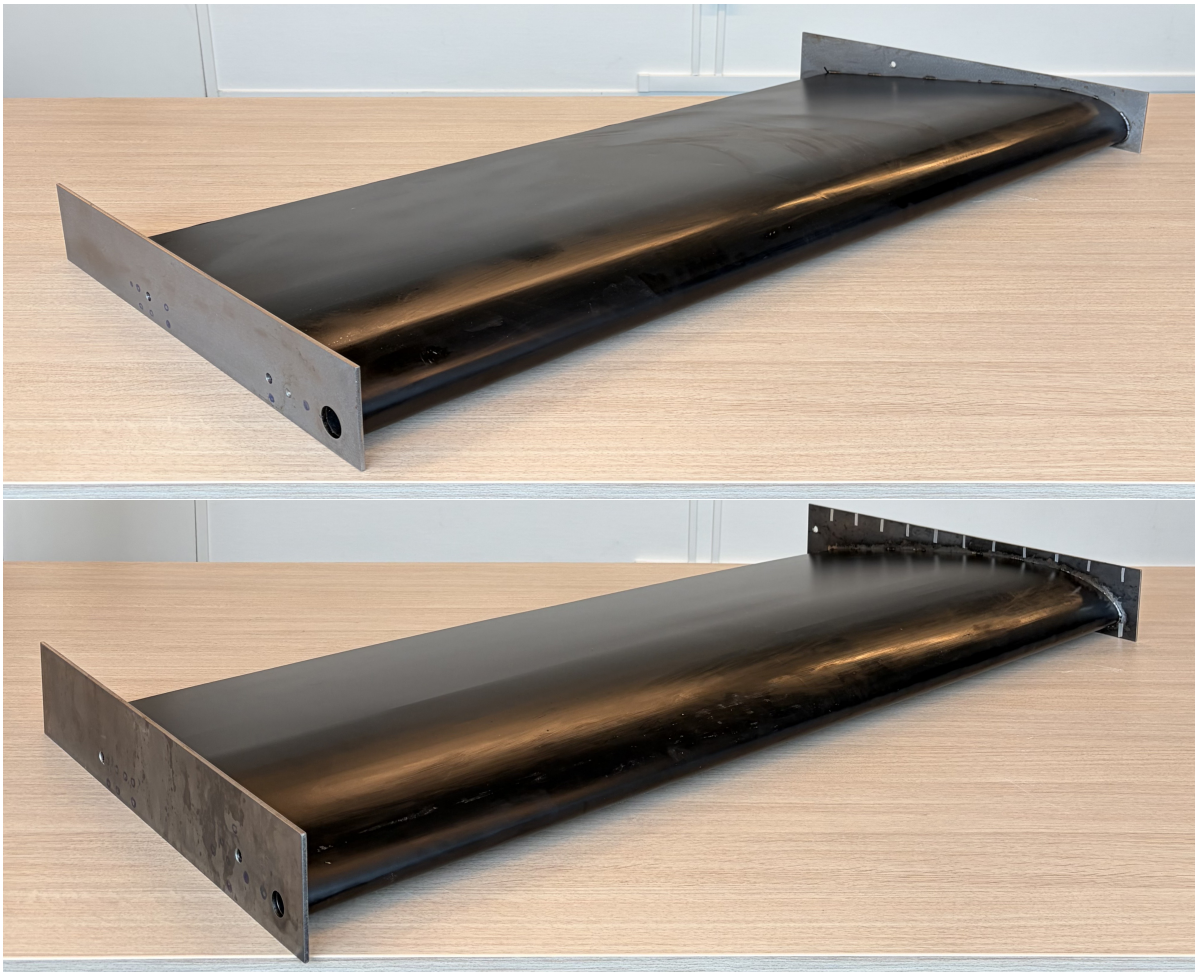

Figure 3.15: Completed models V3 model (top) and Model2 (bottom).

3.3. CFD analysis

The numerical analysis of the LEI airfoils is performed using CFD. The simulations are made with the CFD toolchain developed by Masure [15]. This toolchain automatically meshes and solves LEI airfoils using Pointwise [43] and OpenFOAM [44]. With this toolchain, the geometric parameters are used as input, after which Pointwise will automatically generate a mesh around this airfoil. Then, using multiple angles of attack and the Reynolds number as input, OpenFOAM will try to calculate a converged solution based on these input parameters. First, in Sect. 3.3.1, the meshing will be explained. Second, in Sect 3.3.2, the simulation setup is described. Third, in Sect 3.3.3, the convergence monitoring is explained.

3.3.1. Meshing

To mesh the LEI airfoil, a structured O-grid is generated using Pointwise [43]. The O-grid is selected as the grid is insensitive to angle of attack variations. As only one grid has to be generated per angle of attack, it will significantly reduce the computational cost. The far-field boundary is modelled as a cylinder. The region is meshed with 201 cell layers outward from the profile with a unit depth of length 1.

As a LEI airfoil has a sharp corner at the connection between the LE-tube and pressure side canopy, a fillet is used to smoothen this connection. Furthermore, a canopy thickness is introduced as the actual canopy also has a finite thickness. This also made a rounded trailing edge possible, which is beneficial for the connection of the O-grid. The optimal fillet size and canopy thickness have been determined

using a sensitivity analysis by Masure [15]. The O-grid around a LEI airfoil, including close-ups for the fillet and trailing edge, can be seen in Fig. 3.16.

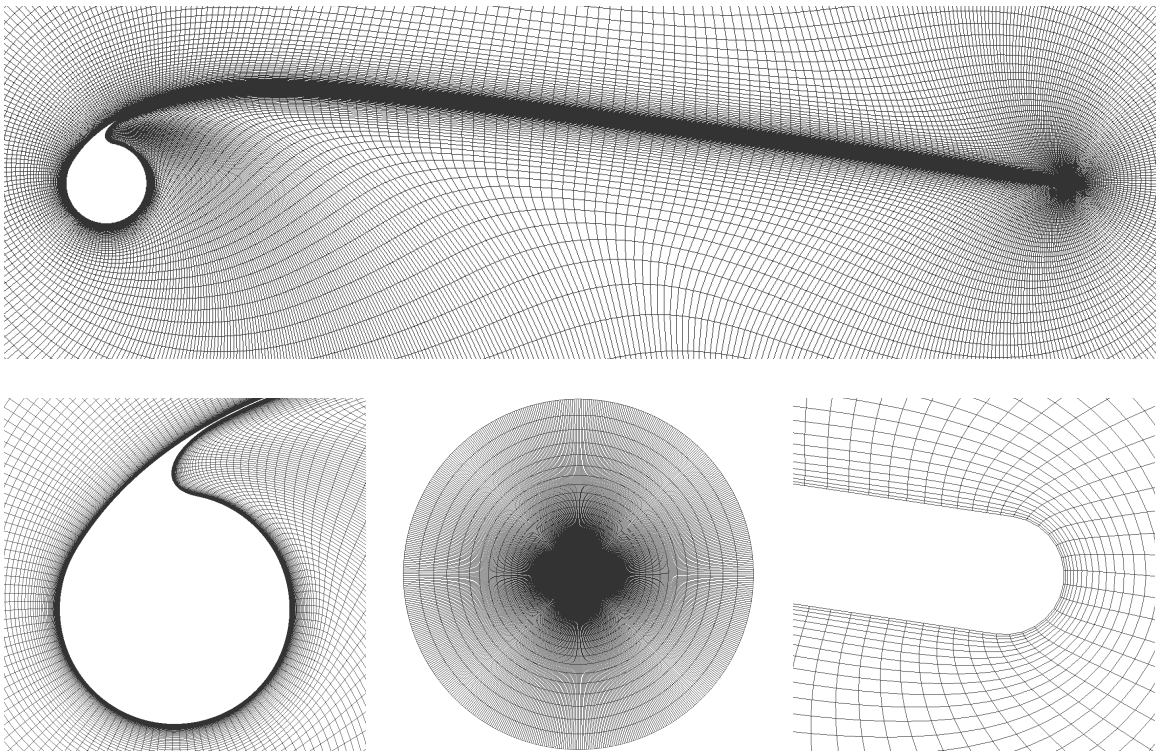

Figure 3.16: Fully structured mesh (575×201) for a LEI kite profile. The top panel shows the airfoil, and the lower panels depict, from left to right, the LE tube, the O-grid, and the TE [15].

Due to the complex shape of the LEI airfoil with respect to a conventional NACA profile, the profile node distribution had to be adjusted to correctly capture the aerodynamic effects around the complex shape. Masure [15] based the spacing on the work of Watchorn [32], where the leading and trailing edge had a uniform node spacing. A hyperbolic tangent distribution was used over the canopy, where the start and end of the canopy have the same spacing as the uniform node distribution to prevent abrupt changes in the grid density.

To generate the different size layers of the cells, Pointwise uses a hyperbolic extrusion algorithm with a fixed growth rate of 1.1 based on the work of Watchorn [32]. A key important parameter for this layer generation is the initial step size y, which influences the y^+ value. The y^+ value is a dimensionless quantity which is used to indicate whether the near-wall mesh resolution is sufficient to capture the boundary layer effect in turbulence modelling. The y^+ value can be calculated with Eq. 3.6. The initial step size y is chosen to ensure the required $y^+_{\max} < 1$ [45]

$$y^+ = \frac{\rho_\infty y u_\tau}{\mu_\infty} \tag{3.6}$$

3.3.2. Simulation setup

The simulations are done using Reynolds-averaged Navier–Stokes (RANS), employing the $k-\omega$ shear stress transport (SST) turbulence model. Within this toolchain, it is possible to assume a fully turbulent boundary layer or select the $\gamma - \tilde{\mathrm{R}}\mathrm{e}_{\theta t}$ transition model [46]. The inlet velocity scalar u_∞, set to $1\,\mathrm{ms}^{-1}$, is projected in the direction of the angle of attack to obtain the vector inlet velocity seen in Eq. 3.7.

$$\mathbf{u}_{\mathrm{i}} = u_{\infty} \begin{bmatrix} \cos\alpha \\ \sin\alpha \\ 0 \end{bmatrix} \tag{3.7}$$

The turbulent kinetic energy, k_{i}, is defined as Eq. 3.8 where I represents the freestream turbulence intensity. The specific dissipation rate ω_{i} at the inlet is defined as Eq. 3.9.

$$k_{\mathrm{i}} = \frac{3}{2}(u_{\infty} I)^2 \tag{3.8}$$

$$\omega_{\mathrm{i}} = \frac{k_{\mathrm{i}}}{\nu_{\infty}} \left(\frac{\nu_{\mathrm{t}}}{\nu_{\infty}} \right)^{-1} \tag{3.9}$$

$\nu_{\mathrm{t}}/\nu_{\infty}$ represents the eddy viscosity ration. The values for I and $\nu_{\mathrm{t}}/\nu_{\infty}$ are set to 0.02% and 10 respectively based on the sensitivity analysis performed by Folkersma [22]. The boundary conditions for the flow variables are tabulated in Table 3.8. The airfoil surface is defined as a stationary, impermeable no-slip wall with the associated boundary conditions. The spanwise boundaries are set to EMPTY to enforce 2D.

Table 3.8: Boundary conditions used for the RANS simulation

Variable	Unit	Far Field	Airfoil Surface
$\mathbf{u}$	$\mathrm{m s^{-1}}$	inletOutlet	fixedValue
p_{k}	$\mathrm{m^2 s^{-2}}$	outletInlet	zeroGradient
k	$\mathrm{m^2 s^{-2}}$	inletOutlet	fixedValue
ω	$\mathrm{s^{-1}}$	inletOutlet	omegaWallFunction
ν_{t}	$\mathrm{m^2 s^{-1}}$	calculated	nutkWallFunction

3.3.3. Convergence monitoring

In the toolchain developed by Masure [15], the threshold for the flow and force residuals is set at 8×10^{-7} and 10^{-4} respectively, with a maximum number of iterations set to 5.001. Exceeding this results in a non-converged simulation.

Figure 3.17 shows the flow and force residuals of the V3 model at $\alpha = 6°$ and $\mathrm{Re} = 10^6$. The final flow residuals fall below the convergence threshold, whereas the force residuals show oscillatory behaviour. This indicates unsteadiness in the flow, but it can still provide a converged solution. Because there is unsteadiness, an attempt has been made to perform unsteady RANS (URANS) simulations to see if this would be more accurate in capturing separation and the influence of the recirculation zone. However, a number of problems have been encountered. For this reason, the rest of the report will only cover RANS simulations. A more detailed discussion on URANS is given in App. C.

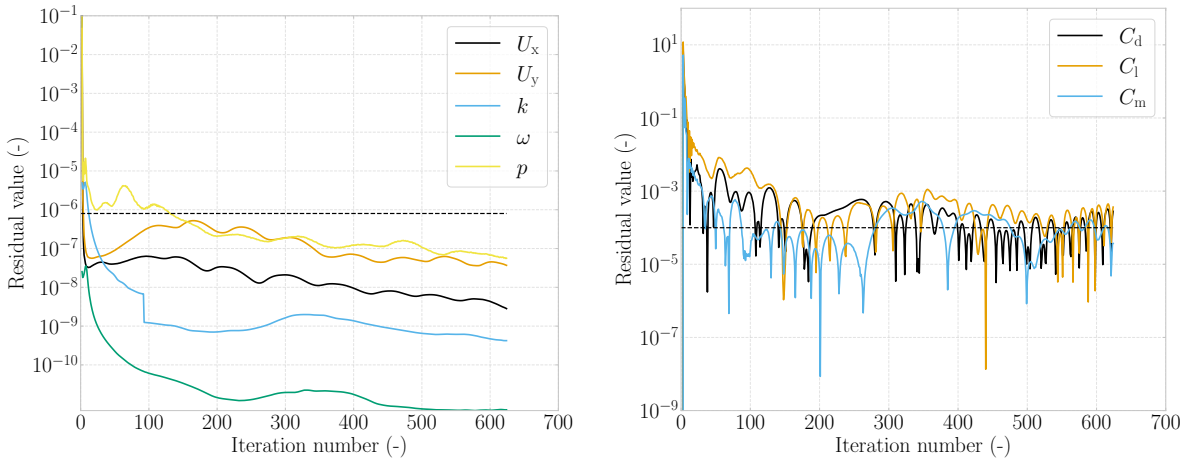

Figure 3.17: Final flow (left) and force (right) residuals of the V3 model at $\alpha = 6°$ and $\mathrm{Re} = 10^6$

4

Experimental setup

This chapter describes the experimental setup used in the LTT at TU Delft. The setup enables both the monitoring of aerodynamic coefficients and the detection of boundary layer transition. Section 4.1 presents the measurement equipment and visualisation methods, while Sect. 4.2 discusses the determination of the critical zigzag tape height required to trigger transition.

4.1. Wind tunnel equipment

This section will cover all the equipment that will be used during the wind tunnel test. The sections are divided into multiple subsections. Section 4.1.1 will explain all the equipment used to capture the aerodynamic coefficients of the LEI airfoil. Section 4.1.2 will provide all the equipment used to visualise the state of the boundary layer. Finally, sect 4.1.3 and 4.1.4 will give information on the turntable and the fan, respectively.

4.1.1. Coefficient measurement equipment

In the wind tunnel, the goal is to determine the lift and drag coefficients. To calculate the lift coefficient, a strip with pressure tabs will be installed on the wind tunnel walls. The drag coefficient can be measured with the use of a wake rake. The downside of using these two measuring devices is that the moment coefficient can not be calculated. This means that, in order to calculate the corrections, an educated guess has to be made for the moment coefficient. This will be further explained in Sect. 6.3. This section will explain more about the measurement equipment used in the wind tunnel.

Pressure strips on wall

In the test section of the LTT, two pressure strips can be mounted on the walls. These strips are $2.4\,\mathrm{m}$ long with 22 equally spaced pressure holes and can be seen in Fig. 4.1. As the test section is $2.6\,\mathrm{m}$ long, the strips are mounted exactly in the middle, leaving $10\,\mathrm{cm}$ at each end. This measurement device captures the pressure footprint produced by the airfoil inside the wind tunnel test section. The pressure footprint extends infinitely upwind and downwind of the airfoil, and therefore, it is not possible to capture the entire footprint. Processing this data will be explained in Ch. 6.

Figure 4.1: Pressure strip mounted on the side of the wind tunnel

Wake rake
In the wake of the airfoil, a wake rake is placed. The wake rake consists of 67 total pressure tubes and 16 static pressure tubes over a length of $504\,\mathrm{mm}$ [40]. The wake rake can be seen in Fig. 4.2.

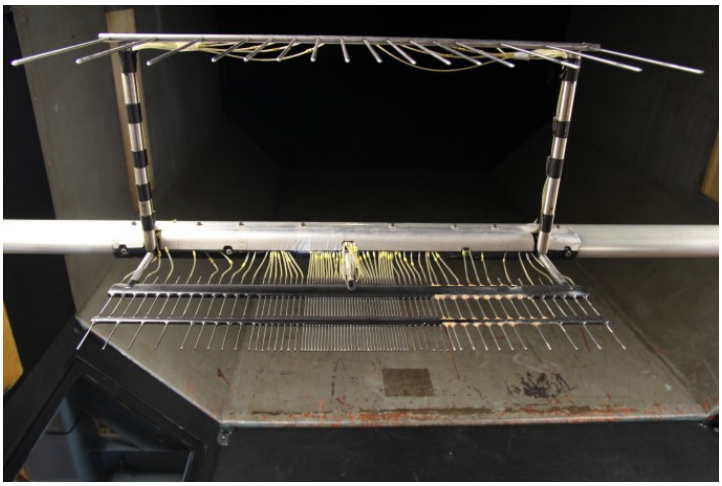

Figure 4.2: Wake rake inside the test section

All pressure tubes from the pressure strips on the wall and the wake rake are combined in a central system. The measurements are recorded using an electronic data acquisition system [47]. The wake rake measures the loss in momentum behind the airfoil. From this, the drag coefficient can be calculated automatically. If the size of the wake becomes larger than the wake rake, the wake rake cuts out, after which the drag measurements can not be taken anymore. This is done to prevent false readings as the entire wake can not be captured by the wake rake and thus the total loss in momentum.

4.1.2. Boundary layer visualization

To visualise the boundary layer transition, different methods can be used. This section will explain more about three different methods. Infrared (IR) imaging, a microphone, and flow visualisation oil.

Infrared imaging
The principle behind infrared imaging of the transition from a laminar boundary layer into a turbulent boundary layer is based on the coefficient of convection of heat transfer of both layers. The laminar

boundary layer acts as an insulator, whereas the turbulent boundary layer, due to its increase in vorticity, will increase the heat transfer from the surface to the flow. This difference in heat transfer will result in a surface temperature change across the airfoil. This method of imaging only works when there is a difference in temperature between the model and the flow. For this reason, multiple heat lamps, located in the walls of the wind tunnel test section, are used to heat up the surface. The higher the temperature difference between the model and the flow, the clearer the distinction becomes between the laminar and turbulent boundary layer [48].

The major downside of IR imaging is that it requires a model material with a high emissivity, as this aids in the visualization of the surface heat. Next to this, low thermal conductivity is preferable, as the heat from the laminar side will not creep towards the turbulent side. The wind tunnel models are created out of steel. Steel has a low surface emissivity and high thermal conductivity, which could result in poor infrared images [49]. According to Running et al. [49], a matte-black thin wrap-film (3M™Wrap Film Series 1080) aids significantly in the quality of IR images as the tape has a high emissivity and low thermal conductivity. For this reason, a black decoration foil is used to wrap to model, aiding in emissivity and thus improving the figures.

Microphone
A less accurate way of determining the location of transition across an airfoil is by the use of a microphone. During testing, a microphone can be held near the top surface of the airfoil to measure the sound. When the boundary layer becomes turbulent, the noise increases significantly due to the vorticity. It is difficult to specify at which location the boundary layer becomes turbulent, as the location of the microphone is hard to read. Next to this, the microphone will sit on a stick, which will influence the airfoil and thus influence the boundary layer, making the measurement inaccurate. The microphone is useful to quickly validate the infrared images.

Flow visualization oil
Flow visualization oil is an oily substance that can be applied to the airfoil. It consists of paraffin with a UV-sensitive additive. During a test at a constant angle of attack, the oil creeps along the surface in the streamwise direction. The friction coefficient determines the patterns seen by the oil flow visualization. In Fig. 4.3, a friction plot is given where the flow goes from laminar to turbulent with transition. The arrows indicate what pattern the oil shows due to the friction coefficient.

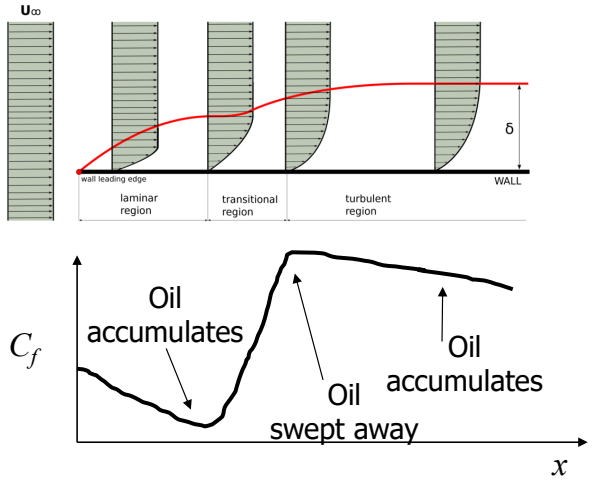

Figure 4.3: Overview of oil flow due to the friction coefficient based on boundary layer transition [50]

The laminar and turbulent boundary layer have a similar oil streamwise pattern. The distinction between these regions is indicated by the transitional region. As the friction coefficient increases, the oil is swept away. This creates a visible dark area between the laminar and turbulent regions. When the airflow separates from the airfoil, the friction coefficient becomes zero. This results in the oil accumulating over the entire separated region.

4.1.3. Turntable

The models are attached to the turntable in the test section. The turntable sets the angle of attack of the model. In the controlling software, a range of angles can be specified, which results in the system automatically turning the airfoil to the specific angles inside the wind tunnel and taking each measurement.

The models are mounted to the ground plate. The ground plate, seen in Fig. 4.4, sits at the top and bottom of the turntable, where screws can be used to attach the model.

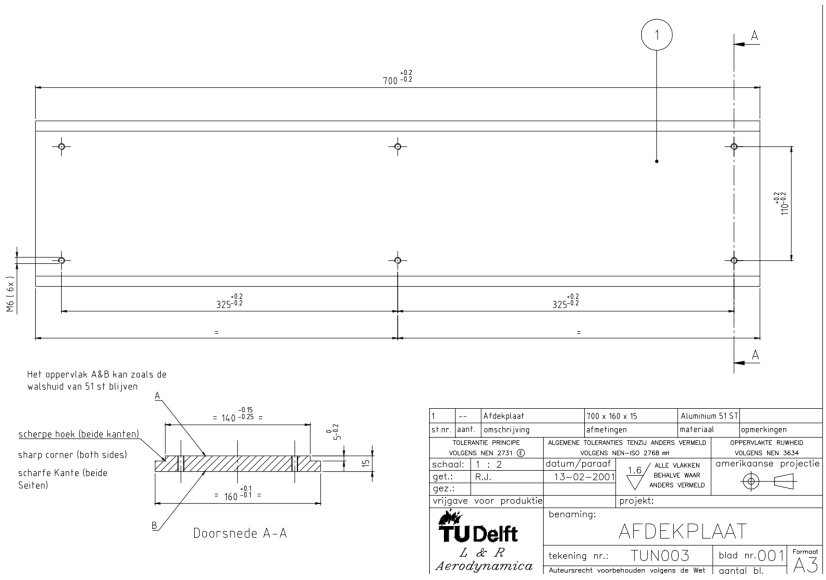

Figure 4.4: Ground plate for the LTT test section

4.1.4. Fan speeds

The wind speed is controlled by changing the revolutions per minute (RPM) of the fan. As a rule of thumb, an $1\,\mathrm{ms}^{-1}$ increase in wind tunnel flow corresponds approximately to a $12\,\mathrm{RPM}$ increase. The distance between the fan and the test section is significant. Therefore, it is important to wait after changing the RPM of the fan. This will ensure that the flow seen in the test section stays constant and that large under- or overshoots are prevented. Table 4.1 shows the required RPM per wind speed for testing.

During testing, the wind tunnel will automatically adjust the fan speed RPM to keep the Reynolds number constant. As the fan moves the air through the wind tunnel, it will increase the temperature. As the temperature increases, the air density decreases. This will lower the Reynolds number. The reduction in Reynolds number is compensated by increasing the wind speed and thus the fan's RPM

Table 4.1: Required RPM per flow velocity inside the test section

$U_\infty\ (\mathrm{ms}^{-1})$	RPM
28.0	336
29.5	354
56.0	672
58.5	702

4.2. Zigzag tapes

Zigzag tapes are used to force the transition of the boundary layer. In Fig. 4.5, the three parameters describing the shape of the zigzag tapes can be seen. For this experiment, with models of this size, $\theta = 60°$ and $w = 12\mathrm{mm}$ according to Bernardy [41]. The required thickness of the zigzag tape depends

on the critical roughness height. This roughness height can be calculated with Eq. 4.1 [51]. Do note that in Fig. 4.5, h is used to describe the height of the zigzag tape, whereas in Eq. 4.1, k is used to describe the critical height to trip the boundary layer.

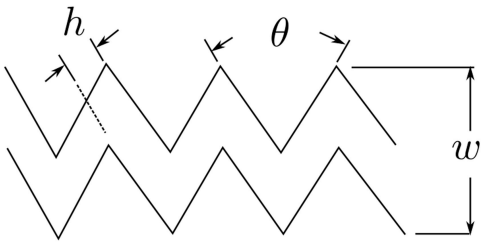

Figure 4.5: The shape and critical parameters describing zigzag tapes [52]

$$k = \frac{\mathrm{Re_k} v}{U_\infty} \tag{4.1}$$

In Eq. 4.1 k is the critical roughness height in m, $\mathrm{Re_k}$ the critical roughness Reynolds number, which lies between 200 and 600, v the kinematic viscosity in $\mathrm{m^2 s^{-1}}$, and U_∞ the free-stream velocity in $\mathrm{ms^{-1}}$. In Fig. 4.6, the roughness height k versus wind speed U_∞ is plotted for different critical roughness Reynolds numbers. From this, the required thickness zigzag tables for both models are tabulated in Table 4.2.

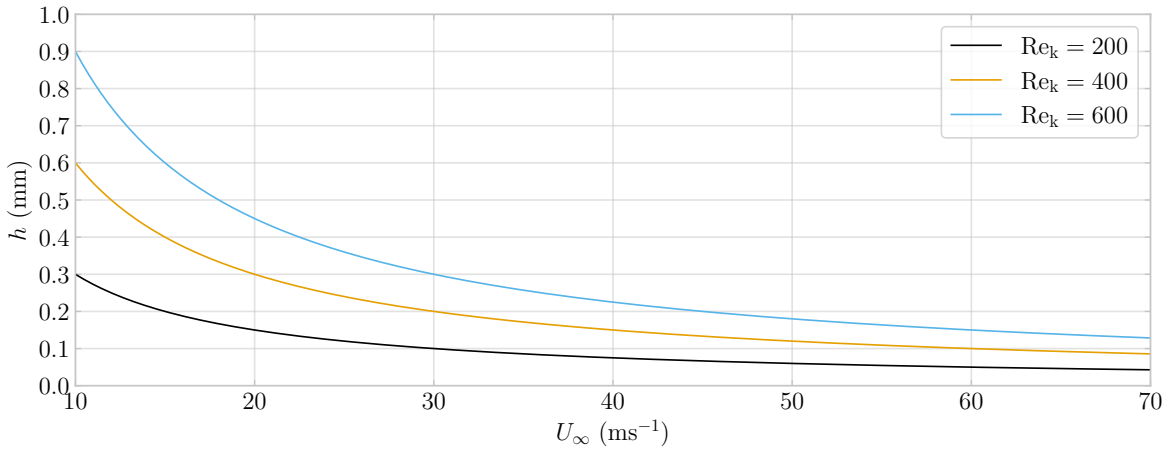

Figure 4.6: Critical roughness height versus wind speed for multiple critical roughness Reynolds numbers

Table 4.2: Critical roughness height for the V3 model and Model2

$\mathrm{Re_k}$	k (mm) for V3 model		k (mm) for Model2	
	$U_\infty = 29\ \mathrm{ms^{-1}}$	$U_\infty = 57\ \mathrm{ms^{-1}}$	$U_\infty = 30\ \mathrm{ms^{-1}}$	$U_\infty = 60\ \mathrm{ms^{-1}}$
200	0.103	0.053	0.100	0.050
600	0.310	0.158	0.300	0.150

In practice, the required zigzag thickness to trip the boundary layer is determined during testing. It is not desired that the zigzag tape be unnecessarily thick, as this will increase the drag of the model. In the experiment, only one thickness of zigzag tape will be used. This is done as it requires time to reapply the zigzag tapes between different Reynolds runs. The thickness that will be used is $0.2\,\mathrm{mm}$. This thickness ensures that the boundary layer is tripped during the $\mathrm{Re} = 2 \times 10^6$ runs and will most likely trip during the $\mathrm{Re} = 1 \times 10^6$ runs. The increase in drag is assumed to be negligible.

5

Test cases

This chapter summarises the wind tunnel experiments conducted on the V3 model and Model2. The tests were performed at various Reynolds numbers, angles of attack, and with different locations of zigzag tapes to study aerodynamic performance and transition behaviour. Section 5.1 covers initial uncertainty checks, including hysteresis, long runs, and repeatability. Section 5.2 outlines the test cases performed for each model. Finally, Sect. 5.3 describes the selection of zigzag tape thickness based on transition effectiveness.

5.1. Uncertainty analysis test

Before starting the actual test cases, a few initial checks were done to understand the uncertainty in the results. These included tests for hysteresis, repeatability, and validation of the testing interval.

Hysteresis describes a situation where the airfoil's aerodynamic behaviour does not just depend on the current angle of attack, but also on how that angle has changed over time. This was tested by first taking the airfoil deep into stall and then reducing the angle of attack back to non-stall conditions. If hysteresis does not apply, then the aerodynamic coefficients should be the same when returning from stall. Differences between the two would show that the history affects the results.

Determining the duration of each measurement was done by performing a long run and a normal run. The same airfoil was kept at a constant angle of attack and Reynolds number and tested twice. The long measurement took three times as many samples as the normal measurement. Comparing the cumulative mean indicates the validity of the duration of the measurement.

To check repeatability and whether the test interval was long enough, the same airfoil was kept at a fixed angle of attack and Reynolds number and tested three separate times. The data is compared to validate the repeatability of the experiment.

After these tests, Model2 was tested at $\mathrm{Re} = 2 \times 10^6$ to check if the calculated deflection in was accurate. At this speed, flutter was observed near stall, even though the canopy had been designed to handle these conditions. Because of the flutter, the results no longer represented a rigid 2D airfoil, and the data could not be used. To avoid this, all tests that were originally planned at $\mathrm{Re} = 2 \times 10^6$ were changed to $\mathrm{Re} = 5 \times 10^5$ for both the V3 model and Model2.

This showed that some of the assumptions made in the FEM analysis in SolidEdge were not accurate. Based on those simulations, the canopy was only expected to deflect $2.05\,\mathrm{mm}$. However, those simulations used static loading—forces were applied as fixed loads on each panel. That doesn't reflect what happens when flow separation occurs, as is the case during stall. In that situation, the forces become unsteady and can interact in a way that causes the canopy to flutter. These dynamic effects were not captured in the FEM model and likely explain the discrepancy.

5.2. Test cases

During the testing campaign, multiple test runs will be performed. This section will give an overview of the different tests performed to acquire all relevant data. In Table 5.1, all different test cases are shown for both the V3 model and Model2.

Table 5.1: Overview of test cases for the V3 model and Model2 configurations.

V3 model		Model2	
Re	Configuration	Re	Configuration
5×10^5	No ZZ	5×10^5	No ZZ
1×10^6	No ZZ	1×10^6	No ZZ
1.5×10^6	No ZZ	2×10^6	No ZZ
5×10^5	ZZ on bottom at $90°$	5×10^5	ZZ on bottom at $90°$
1×10^6	ZZ on bottom at $90°$	1×10^6	ZZ on bottom at $90°$
5×10^5	ZZ on top at 5%	5×10^5	ZZ on top at 10%
1×10^6	ZZ on top at 5%	1×10^6	ZZ on top at 10%
5×10^5	ZZ on bottom at $90°$ and on top at 5%	5×10^5	ZZ on top at 5%
1×10^6	ZZ on bottom at $90°$ and on top at 5%	1×10^6	ZZ on top at 5%
5×10^5	ZZ on bottom at $45°$	5×10^5	ZZ on bottom at $90°$ and on top at 5%
1×10^6	ZZ on bottom at $45°$	1×10^6	ZZ on bottom at $90°$ and on top at 5%
1×10^6	ZZ on bottom at $45°$ and on top at 3%		

For the zigzag placement, several different cases were considered. The zigzag tapes were placed at 3%, 5% and 10% on the suction side of the airfoil. Next to this, the zigzag tape was placed on the leading edge tube. ”bottom at $90°$” denotes that the zigzag tape was placed at the lowest point on the LE tube, at 90° from the leading edge. Next to this, ”bottom at $45°$” means that the zigzag tape was placed at an angle of 45° from the leading edge.

5.2.1. Angle of attack overview

The airfoils were tested at a wide range of angles of attack, α, to accurately capture pre-stall, stall, and post-stall behaviour. The exact angles differ between the two models due to differences in their stall behaviour. For the V3 model, the stall angle is expected to be lower, so a finer resolution around $\alpha = 12°$ to $15°$ was used. Model2 was expected to stall at higher angles, so the angle range was extended further into post-stall conditions.

Table 5.2: Tested angles of attack for both airfoil models

V3 model, α range (°)	Model2, α range (°)
-10, -9, -8, -7, -6, -5, -4, -3, -2, -1, 0, 1, 2, 3, 4, 5, 6, 7, 8, 9, 10, 11, 11.2, 11.4, 11.6, 11.8, 12, 12.2, 12.4, 12.6, 12.8, 13, 13.2, 13.4, 13.6, 13.8, 14, 14.2, 14.4, 14.6, 14.8, 15, 16, 17, 18, 19, 20, 21, 22, 23	-10, -9, -8, -7, -6, -5, -4, -3, -2, -1, 0, 1, 2, 3, 4, 5, 6, 7, 8, 9, 10, 11, 12, 12.5, 13, 13.5, 14, 14.2, 14.4, 14.6, 14.8, 15, 15.2, 15.4, 15.6, 15.8, 16, 16.2, 16.4, 16.6, 16.8, 17, 17.2, 17.4, 17.6, 17.8, 18, 18.5, 19, 19.5, 20, 20.5, 21, 21.5, 22, 22.5

5.3. Zigzag tape revision

As the test cases at $\mathrm{Re} = 2 \times 10^6$ were changed to $\mathrm{Re} = 5 \times 10^5$, the thickness of the zigzag tapes had to be adjusted accordingly. Based on Fig. 4.6, the critical roughness height at $\mathrm{Re} = 5 \times 10^5$ lies between $0.2\,\mathrm{mm}$ and $0.6\,\mathrm{mm}$. Since a $0.6\,\mathrm{mm}$ tape would generate too much drag at $\mathrm{Re} = 1 \times 10^6$, different zigzag tapes were tested to determine which thickness was sufficient to trip the boundary layer. In Fig. 5.1, Model2 is shown at $\alpha = 8°$ and $\mathrm{Re} = 5 \times 10^5$, with three zigzag tapes applied: $0.25\,\mathrm{mm}$ at the top, $0.3\,\mathrm{mm}$ in the middle, and $0.2\,\mathrm{mm}$ at the bottom. It is clear that the $0.2\,\mathrm{mm}$ tape does not trip the boundary layer, the $0.25\,\mathrm{mm}$ thick tape does, but the transition is delayed compared to the $0.3\,\mathrm{mm}$ tape. Therefore, the $0.3\,\mathrm{mm}$ zigzag tape was chosen for tripping the boundary layer on the suction side of the airfoil. On the pressure side, it was not possible to confirm the effectiveness of the tape using infrared imaging. To ensure tripping occurred, a $0.5\,\mathrm{mm}$ thick zigzag tape was used.

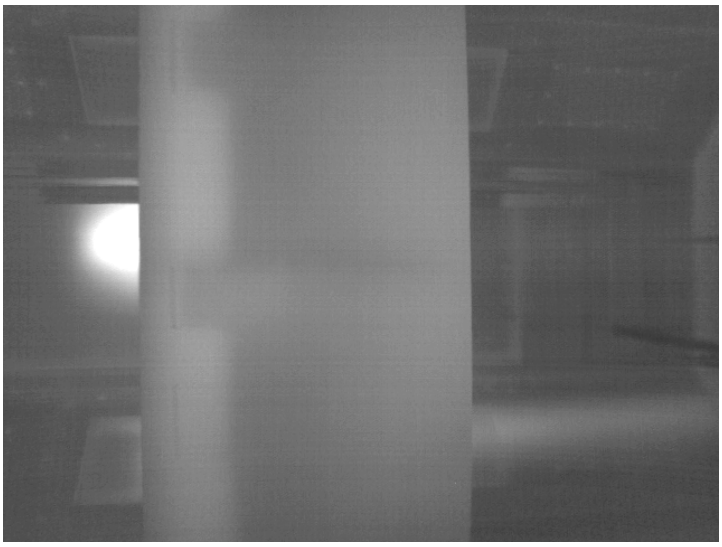

Figure 5.1: Infrared image of the suction side of Model2 with different thickness zigzag tapes of $0.25\,\mathrm{mm}$ (top), $0.3\,\mathrm{mm}$ (middle), and $0.2\,\mathrm{mm}$ (bottom).

To validate that the boundary layer was successfully tripped, a microphone was used to detect the acoustic difference between laminar and turbulent flow. The experimental setup with the microphone is shown in Fig. 5.2. As the probe was moved into the darker shaded area, the microphone picked up a distinct static noise, confirming the presence of a turbulent boundary layer. This method was also applied behind the zigzag tapes on the suction side to verify their effectiveness. On the pressure side, it was more difficult to assess, as the leading edge tube was too small to position the microphone accurately.

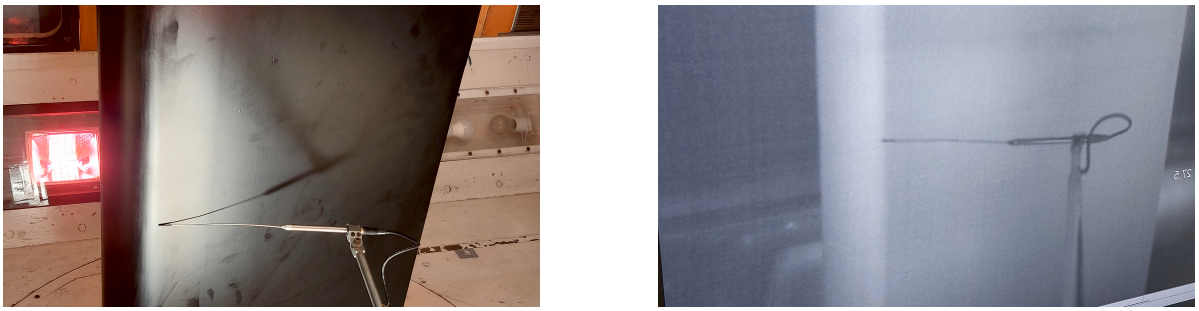

Figure 5.2: Model with microphone along the suction side (left) and the infrared image with the microphone (right)

6

Data Processing

This chapter will explain the methods used to perform the data processing of the raw wind tunnel data. Before the data can be used for analyses, it has to be corrected due to the wind tunnel pressure strips as well as the influence of the wind tunnel walls and wakerake. Next to this, the analysis of the infrared images will be discussed.

In Sect. 6.1, the preprocessing steps are explained before calculating and applying the different correction factors. Second, in Sect. 6.2, the correction factors due to the wall pressure strips are calculated for both the V3 model and Model2. Third, in Sect. 6.3, the formulas are given to correct the airfoil coefficient due to the influence of the wind tunnel walls and the wake rake. At last, the method of determining the location of the transition from the infrared images is explained in Sect. 6.4.

6.1. Data preprocessing

Before performing each test case described in Ch. 5, the wake rake required calibration due to interference from the model's structural rib. This calibration was carried out by traversing the entire height of the wind tunnel with the wake rake and plotting the resulting drag coefficient. The outcome of this full traverse is shown as the black line in Fig. 6.1, where it is clearly visible that the rib induces a significant increase in drag.

To avoid this interference, the measurement range was limited to between $z = 280$ and $z = 380\,\mathrm{mm}$, which consistently avoids the rib. This range was then used in several tests, including the no-zigzag case at $\mathrm{Re} = 1 \times 10^6$, shown as the orange line in the same figure.

However, because the wake rake position had to be manually re-entered each day, an alignment error occurred in a later test. The blue line in the figure shows unusually high drag values that resemble the rib region rather than the clean airfoil. To confirm this, the data was artificially shifted by $z = -100\,\mathrm{mm}$, producing the dashed green line. It confirms that the rake had accidentally been placed too far upwards, overlapping with the rib.

As a result, the data for Model2 required some preprocessing. It was assumed that the range between $z = 340$ and $z = 380\,\mathrm{mm}$ still correctly represents the airfoil drag. All data points outside this range were omitted. While this reduces the number of points available for averaging, the impact was considered acceptable given the circumstances.

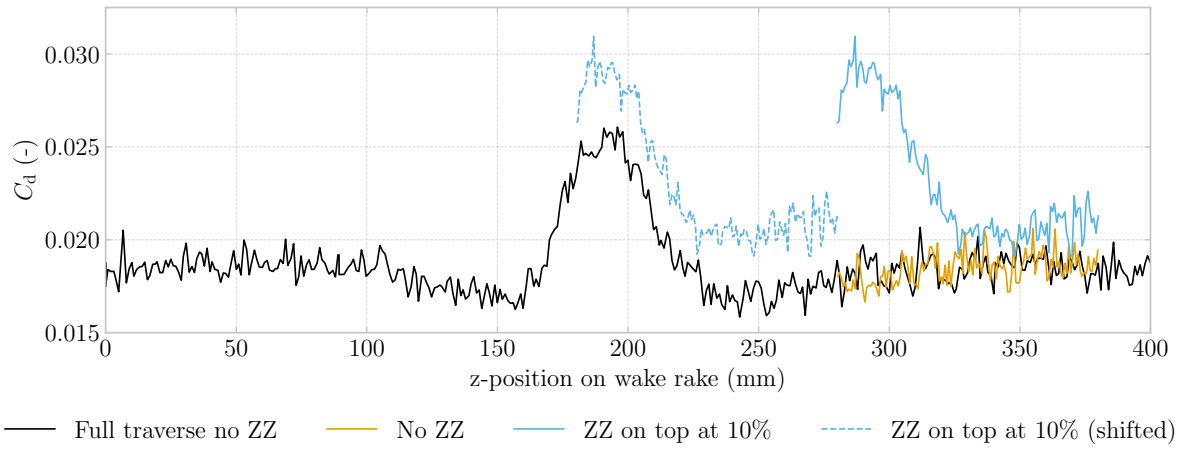

Figure 6.1: Drag coefficient vs wake rake position for Model2 at $\alpha = 8°$ and $\mathrm{Re} = 1 \times 10^6$

6.2. Correction factor wall pressure strips

The lift coefficient is measured by the use of pressure strips on the walls of the wind tunnel. These strips are placed on the pressure and suction side of the airfoil and have a length of $2.4\,\mathrm{m}$. The strips have 22 equally spaced pressure holes, which capture the pressure footprint of the airfoil. The pressure footprint represents the response of the pressure distribution created around the airfoil. This indirectly presents the lift generated by the airfoil. The pressure footprint of an airfoil extends infinitely up- and downstream, thus, the pressure strips are not able to capture the entire pressure footprint. A schematic drawing of this setup can be seen in Fig. 6.2

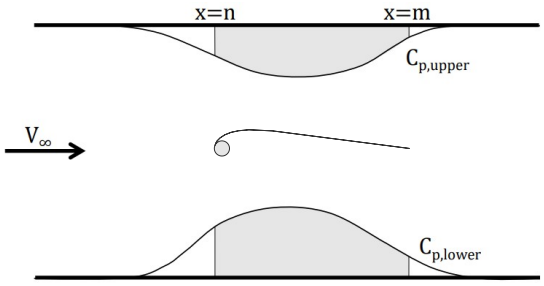

Figure 6.2: Schematic drawing of the pressure footprint on the wind tunnel walls

In this picture, the grey shaded area is the part of the pressure footprint which is captured by the pressure tabs on the wall. To calculate the lift coefficient, the pressure difference between the lower and upper wall has to be integrated over the length of the pressure strips. As this will not capture the entire pressure profile, a correction factor has to be applied. This formula is given in Eq. 6.1.

$$C_l = \frac{1}{\eta c} \int_n^m C_{\mathrm{P,R}} dx \tag{6.1}$$

In this equation, C_l is the lift coefficient, η the wall correction factor, c the chord length and $C_{\mathrm{P,R}}$ the resultant pressure between the upper and lower wall. The pressure strip go from n upstream to m downstream.

A theoretical approach to determine this correction factor is introduced by Abbot et al. [53] and Althaus [54]. The airfoil is represented by a point vortex with a strength Γ. This point vortex is located at the quarter-chord point of the airfoil. It is required to adhere to the wind tunnel wall constraint. This means that the normal velocity at the walls should be zero. To fulfil this constraint, an infinite set of imaging

vortices with alternating sign and equal spacing is placed. A schematic overview of this so-called image system can be seen in Fig. 6.3. According to Abbot et al. [53] and Althaus [54], the complex potential function can be derived. This is Eq. 6.2 where Γ is the vortex strength, z the complex variable $(x + iy)$ and h the wind tunnel width.

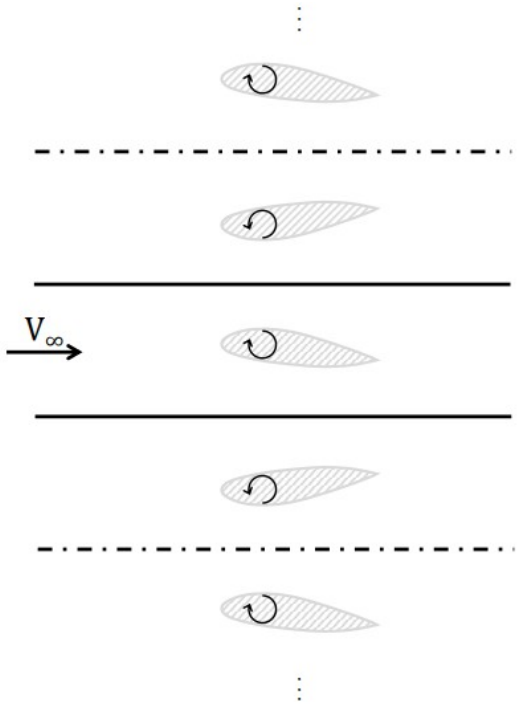

Figure 6.3: Schematic drawing of the image system showing an infinite row of imaging vortices with alternating sign and equal spacing [40]

$$f = \frac{i\Gamma}{2\pi}\log(\sinh\left(\frac{\pi z}{2h}\right)) - \frac{i\Gamma}{2\pi}\log(\sinh\left(\frac{\pi(z-ih)}{2h}\right)) \tag{6.2}$$

Equation 6.2 can be used to derive the velocity and thus the resultant pressure coefficient at the wind tunnel walls. These equations are given in Eq. 6.3 to Eq. 6.5.

$$C_{\mathrm{P,R}} = \frac{(V_\infty + u)^2 - (V_\infty - u)^2}{V_\infty^2} \tag{6.3}$$

Where

$$u = \frac{\Gamma}{2h}\,\mathrm{sech}(\frac{\pi x}{h}) \tag{6.4}$$

So

$$C_{\mathrm{P,R}} = \frac{2\Gamma}{hV_\infty}\frac{1}{\cosh(\frac{\pi x}{h})} \tag{6.5}$$

The generated lift due to this point vortex can be calculated by integrating the pressure distribution along the wind tunnel walls between the upstream location n and downstream location m. Assuming that the point vortex is located at x_0, the limits of integration are $m - x_0$ to $n - x_0$. This lift is referred to as L' and is given by Eq. 6.6 where q_0 is the free stream dynamic pressure. Furthermore, using the Kutta Joukowski theorem, the total lift of a point vortex can be expressed as seen in Eq. 6.7, where Γ is the circulation, ρ the fluid density and V_∞ the free stream velocity. This formula can be rewritten as Eq. 6.8.

$$L' = \int_{n-x_0}^{m-x_0} q_0 C_{\mathrm{P,R}} dx \tag{6.6}$$

$$L = \Gamma \rho V_\infty \tag{6.7}$$

$$L = \frac{2q_0}{V_\infty}\Gamma \tag{6.8}$$

The ratio between L' and L is the correction factor. This correction factor compensates for the lift that is not measured by the pressure strips. Rewriting Eq. 6.9 gives Eq. 6.11

$$\eta_{\mathrm{x}} = \frac{L'}{L} \tag{6.9}$$

$$\eta_{\mathrm{x}} = \frac{\int_{n-x_0}^{m-x_0} q_0 C_{\mathrm{P,R}} dx}{\frac{2q_0}{V_\infty}\Gamma} \tag{6.10}$$

$$\eta_{\mathrm{x}} = \frac{2}{\pi} \arctan\left[\frac{e^{-\pi x_0/h}\left(e^{\pi n/h} - e^{\pi m/h}\right)}{1 + \left(e^{-2\pi x_0/h} e^{\pi(m+n)/h}\right)}\right] \tag{6.11}$$

Finally, after taking into account the chord length of the model, the formula for the correction factor results in Eq. 6.12

$$\eta = \frac{\int_c C_{\mathrm{P,R}} \eta_{\mathrm{x}} d(x/c)}{\int_c C_{\mathrm{P,R}} d(x/c)} \tag{6.12}$$

In the study of de Tavernier [40], it became clear that solving this equation theoretically does not consider the variation in airfoil shape. The study proved that the theoretical values are representable for symmetric airfoils with moderate thickness, but for non-symmetric airfoils, this theoretical relation is no longer true. de Tavernier [40], proposes a method where the theoretical expression for the wall pressure is fitted through the experimental wall pressure. This is done by tweaking the variables x_0, h, and $C_{\mathrm{p,max}}$ to fit the experimental data points. Using the Sequential Least Squares Programming (SLSQP) method, the combination of variables is found for which the squared error is minimized. With these variables, a theoretical fit can be described by Eq. 6.13.

$$C_{\mathrm{P.th}}(x) = \frac{C_{\mathrm{P,max}}}{\cosh(\frac{\pi}{h}(x - x_0))} \tag{6.13}$$

x_0 influences the location of the maximum amplitude, h, determines the width of the curve and $C_{\mathrm{p,max}}$ determines the maximum amplitude. Integrating this function from $10 < x < 10$ using the trapezoidal rule provides a sufficient range to resemble $-\infty$ to $+\infty$. Integrating the experimental data using the trapezoidal rule provides the measured lift coefficient, which only covers the length of the pressure tabs on the wall. These integrations are the numerator and denominator in Eq. 6.12, and thus can be used to calculate the correction factor.

In Fig. 6.4, the fitted curve through the experimental points can be seen for the V3 model at an $\alpha = 8°$ and $\mathrm{Re} = 10^6$.

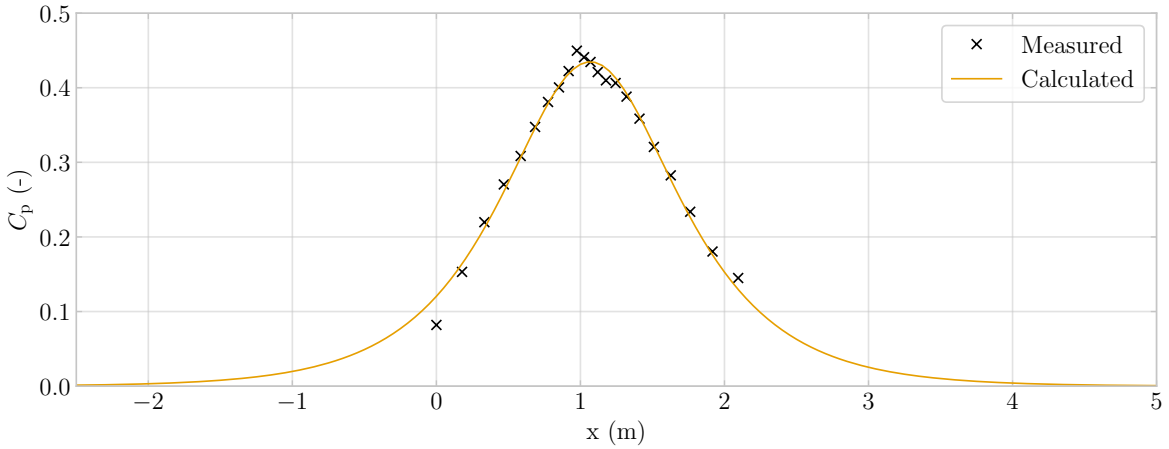

Figure 6.4: Theoretical C_p fit of the pressure distribution of the V3 model without zigzag at $\alpha = 8°$ and $\mathrm{Re} = 10^6$

The calculated correction factors for every angle at $\mathrm{Re} = 10^6$ for the V3 model and Model2 are shown in Fig. 6.5 and Fig. 6.6. The correction factors for $\mathrm{Re} = 5 \times 10^5$ can be seen in Fig. B.1

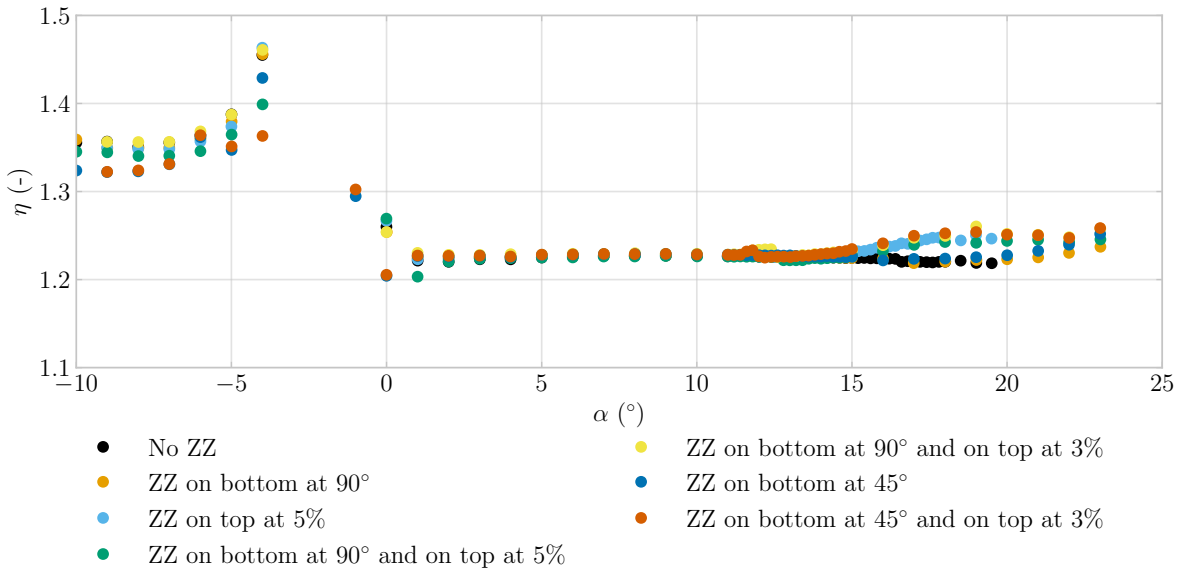

Figure 6.5: Correction factors for all α at $\mathrm{Re} = 10^6$ for the V3 model

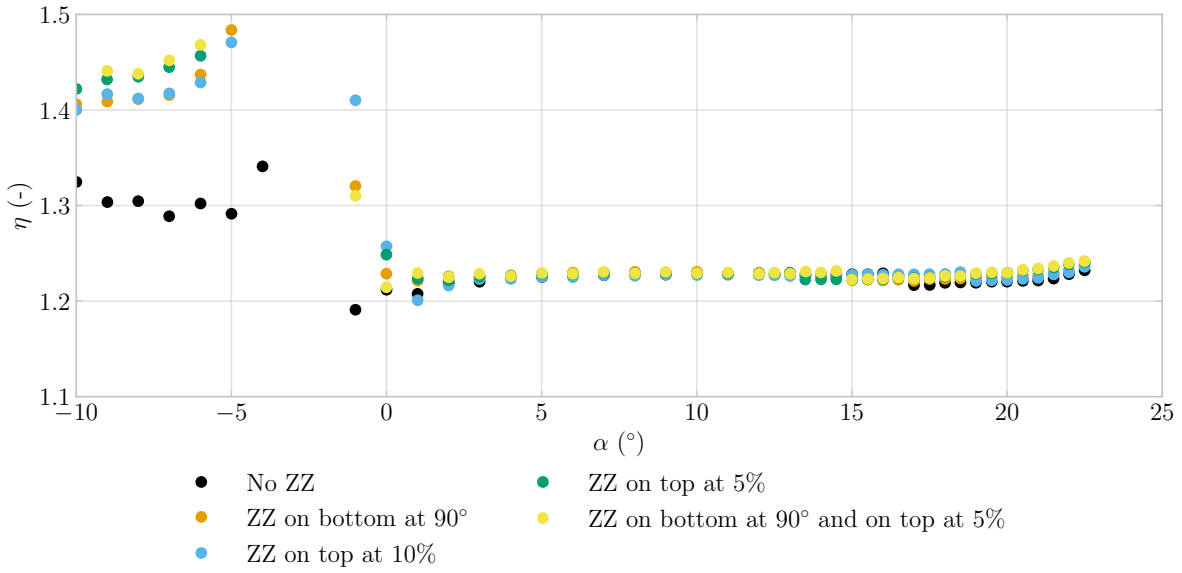

Figure 6.6: Correction factors for all α at $\mathrm{Re} = 10^6$ for Model2

Here you can clearly see that between $\alpha = 2°$ and $\alpha = 8°$, the correction factor stays constant. The average of these correction factors is assumed to be applicable to the entire angle of attack range. The reason for the outliers around $\alpha = -2°$ is due to the zero-lift angle of attack. As the airfoil produces little to no lift, it becomes increasingly difficult to fit a curve through the measurement points. Therefore, the correction factor becomes inconsistent. For each case, the final correction factor is calculated by averaging the correction factors between $\alpha = 2°$ and $\alpha = 8°$. In Table B.1, the final correction factors are tabulated.

6.3. Wall correction factors

Measurements in closed-loop wind tunnels are affected by the presence of solid walls that constrain the flow around the test model. Unlike free-flight conditions, the proximity of the tunnel walls alters the pressure distribution and streamlines around the model, leading to deviations in aerodynamic coefficients such as drag, C_d, lift, C_l, and the angle of attack, α. These effects are referred to as wall interference.

To compensate for these effects and approximate free-stream conditions more accurately, wall correction factors are applied. These corrections remove the influence of the tunnel walls on the measured values, making the results more representative of unbounded flow.

The correction formulas used in this work are based on the classical method developed by Allen & Vincenti [55]. Their approach accounts for three main sources of interference: solid blockage, wake blockage, and lift interference. Each of these components contributes to the overall distortion of the flow and must be corrected to obtain accurate aerodynamic coefficients. The final correction formulas by Allen & Vincenti [55] have been rewritten by Timmer [56] and are given in Eq. 6.14 to 6.16.

Before applying these corrections, the lift coefficient measured from the pressure strips, $C_{\mathrm{l,meas}}$, must first be adjusted as explained in Sect. 6.2 This is done using a correction factor η, such that the uncorrected lift coefficient becomes $C_\mathrm{l}' = C_{\mathrm{l,meas}}\eta$. This corrected value is then used in the wall interference equations below:

$$\alpha = \alpha' + \frac{\sigma}{2\pi\beta}(C_\mathrm{l}' + 4C_\mathrm{m}') \tag{6.14}$$

$$C_\mathrm{l} = C_\mathrm{l}'\left[1 - \frac{\sigma}{\beta^2} + 5.25\frac{\sigma^2}{\beta^4} - \frac{(2-M'^2)}{\beta^3}\Lambda\sigma\left(1 + \frac{1.1\beta}{(t/c)}\alpha^2\right) - \frac{(2-M'^2)(1+0.4M'^2)}{4\beta^2}\left(\frac{c}{h}\right)C_\mathrm{d}'\right] \tag{6.15}$$

$$C_{\mathrm{d}} = C'_{\mathrm{d}}\left[1 - \Delta C^*_{\mathrm{d}} - \frac{\left(2 - M'^2\right)}{\beta^3}\Lambda\sigma\left(1 + \frac{1.1\beta}{(t/c)}\alpha^2\right) - \frac{\left(2 - M'^2\right)\left(1 + 0.4M'^2\right)}{4\beta^2}\left(\frac{c}{h}\right)C'_{\mathrm{d}}\right] \tag{6.16}$$

In these equations, the primed coefficients (α', C'_{l}, C'_{d}, C'_{m}, M') refer to the uncorrected values obtained directly from the wind tunnel measurements. The corrected values are denoted without a prime. $\beta = \sqrt{1 - M'^2}$ is the compressibility correction factor. This value will be close to one as 1 as the flow is incompressible at the wind speeds for which the tests are performed. σ is the tunnel blockage factor. Λ is the body shape factor, which depends on the airfoil geometry. The ratio t/c represents the relative thickness of the airfoil, and c/h is the ratio of airfoil chord to tunnel height. The term ΔC^*_{d} is the wake buoyancy correction, which is zero when drag is measured using a wake rake.

The body shape factor Λ is a dimensionless quantity used in the calculation of the solid blockage correction in wind tunnel testing. It characterises how much the shape of the airfoil disturbs the surrounding flow due to both its thickness and surface pressure distribution. The factor is derived using potential flow theory and image systems, assuming symmetric streamlines and small disturbance approximations. A higher Λ value indicates that the airfoil displaces more flow, resulting in a stronger blockage effect. The formula for Λ can be seen in Eq. 6.17.

$$\Lambda = \frac{16}{\pi}\int_0^1 \frac{y}{c}\sqrt{(1 - C_{\mathrm{p}})\left(1 + \left(\frac{dy}{dx}\right)^2\right)}d\left(\frac{x}{c}\right) \tag{6.17}$$

Here, y is the local vertical coordinate of the symmetric airfoil profile, C_{p} is the inviscid pressure coefficient at that chordwise location, and c is the chord length. This factor is calculated by S. Bernardy prior to the wind tunnel tests [41].

Finally, it should be noted that the angle of attack correction in Eq. 6.14 requires the uncorrected moment coefficient C'_{m}. Since this quantity cannot be obtained directly from wall pressure strips or wake rake measurements, an alternative approach was used. The moment coefficient was determined numerically using the CFD framework developed by Masure [15], which provides C_{m} values over a range of angles of attack. To estimate the uncorrected moment coefficient at a given angle of attack, the CFD data was interpolated. This approximation is considered acceptable given the relatively small influence of C'_{m} on the overall angle correction.

6.4. Infrared images processing

One method used to visualise the boundary layer is infrared imaging. Thermal cameras were positioned on both the suction and pressure sides and captured an infrared image at each angle of attack for every test case. During testing, it became clear that the recirculation zone of the LEI airfoil could not be visualised with infrared imaging, as the heat signature from the suction side transferred through the canopy to the pressure side. In Fig. 6.7, both the pressure and suction sides of the airfoil are shown. On the top surface, three zigzag tapes of different thicknesses were applied to determine the minimum thickness required to trip the boundary layer. From this figure, it becomes evident that the boundary layer on the suction side is visible from the pressure side. As a result, infrared imaging was used solely to identify the transition location on the suction side of the airfoil.

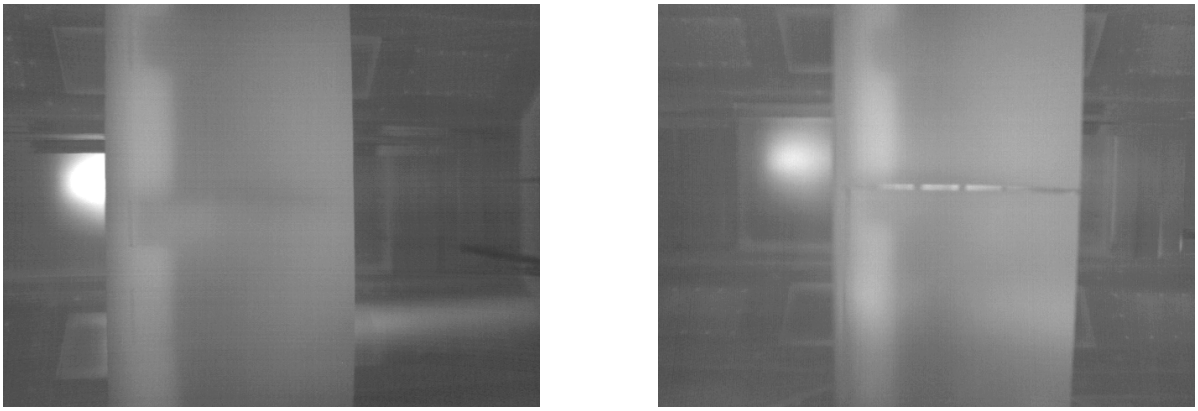

Figure 6.7: Infrared images at $\alpha = 8°$ and $\mathrm{Re} = 5 \times 10^5$ of Model2 suction side (left) and pressure side (right) with different thickness zigzag tape. $0.25\,\mathrm{mm}$ (top), $0.3\,\mathrm{mm}$ (middle) and $0.2\,\mathrm{mm}$ (bottom).

To determine the location of the transition, pixel analysis is used. With pixel analysis, the grayscale intensity of each pixel is determined within a certain region. These values are then averaged to obtain the overall grayscale intensity along the image. The grayscale intensity versus location is plotted in Fig. 6.8. This intensity profile is used to locate the leading and trailing edges as well as to determine the location of the transition. As the cameras are fixed in place, the leading and trailing edges are in different locations depending on the angle of attack. Therefore, the location has to be determined using this method for every angle of attack. To determine these locations, the maximum and minimum gradient is used to locate the leading and trailing edges, respectively. When these outer bounds are located, the second-largest negative gradient is located, which resembles the location of the transition. Then, based on the number of pixels, the transition line is behind the leading edge, and the chordwise position can be calculated. This has to be corrected with Eq. 6.18 as the airfoil is at a specific angle with respect to the cameras.

$$x_{\mathrm{tr,corr}} = \frac{x_{\mathrm{tr}}}{\cos(\alpha)} \tag{6.18}$$

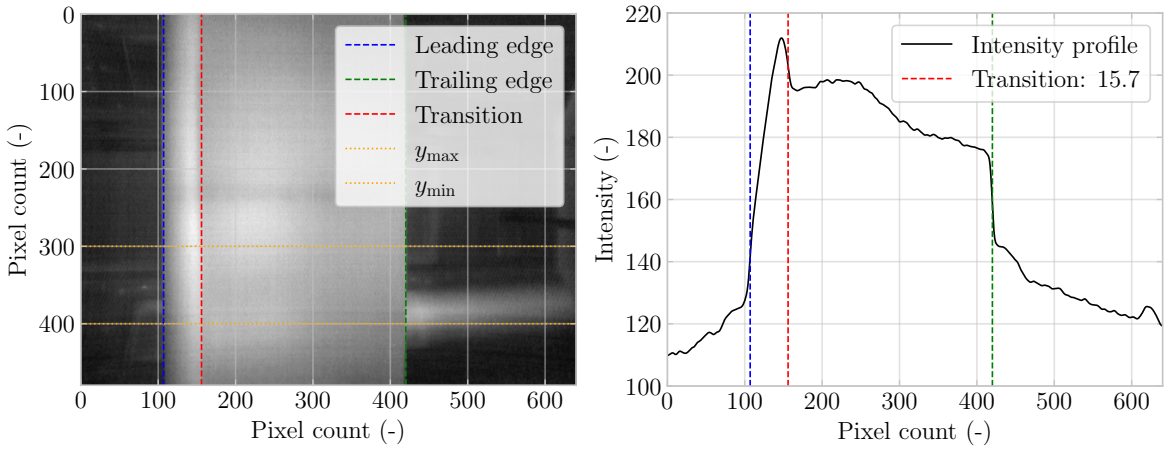

Figure 6.8: Transition line of the V3 model at $\alpha = 2°$ and $\mathrm{Re} = 10^6$

7

Results

This chapter will cover the results obtained from the wind tunnel tests. First, the uncertainty of the results is quantified by testing for hysteresis, the duration of the measurements and the repeatability of the measurements. This will be given in Sect. 7.1. Second, the airfoil polars for both the V3 model and Model2 will be explained in Sect. 7.2. Third, the location of the transition visualised by the infrared images will be shown in Sect. 7.3. Fourth, the analysis on the oil flow figures will be discussed in Sect. 7.4. At last, an overview of the infrared images, oil flow photo's and CFD results will be given in Sect. 7.5

7.1. Uncertainty

Prior to performing the tests stated in Sect. 5.2, the uncertainty tests were performed. As stated in Sect. 5.1, these tests comprised the hysteresis effect, long runs, and repeatability. The results of these tests are outlined in the following subsections.

7.1.1. Hysteresis effect

To check for hysteresis, the airfoil has been pitched up into a deep stall, after which the angle of attack was decreased. The uncorrected lift coefficient with respect to angle of attack, α, can be seen in Fig. 7.1 for Model2 at $\mathrm{Re} = 10^6$. In this figure, the black line corresponds to a positive pitching moment, whereas the orange line depicts a negative pitching moment. This provides a clear distinction between the moment the airfoil's pitching switches direction.

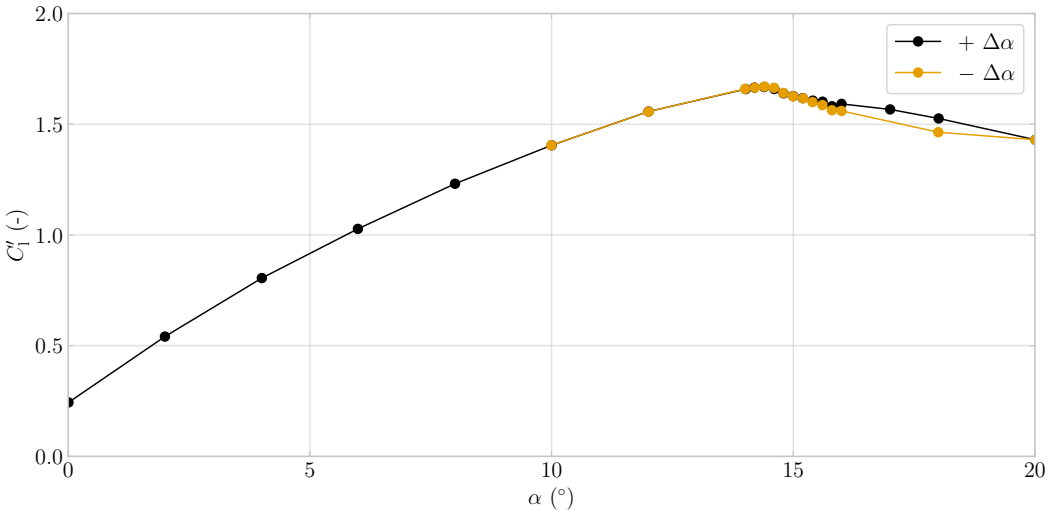

Figure 7.1: Hysteresis effect of Model2 at $\mathrm{Re} = 10^6$

From this figure, it becomes clear that the airfoil stalls at $\alpha = 14°$. Hereafter, the airfoil is pitched until $\alpha = 20°$. At this point, the airfoil is pitched back into pre-stall conditions. From the figure, it becomes clear that prior to stall, at stall, and just after stall, the uncorrected lift coefficient, C_l', is the same. From $\alpha = 16°$ to $\alpha = 20°$, C_l' differs with a maximum of 0.1. Given that the hysteresis only plays a minor role in angles above $\alpha = 16°$, it was decided to neglect this effect and not perform a forward and backward α sweep for every case.

7.1.2. Long runs

To check whether the duration of the tests are sufficient, an experiment was performed with three times the sampling time, referred to as a 'long run'. The long run was performed for the V3 model at $\alpha = 5°$ and $\mathrm{Re} = 10^6$. In Fig. 7.2, the results of the raw data of the normal and long run are plotted for the uncorrected lift and drag coefficient as well as the middle pressure tab on the upper and lower surface. The cumulative mean is plotted in order to check whether a steady state has been achieved.

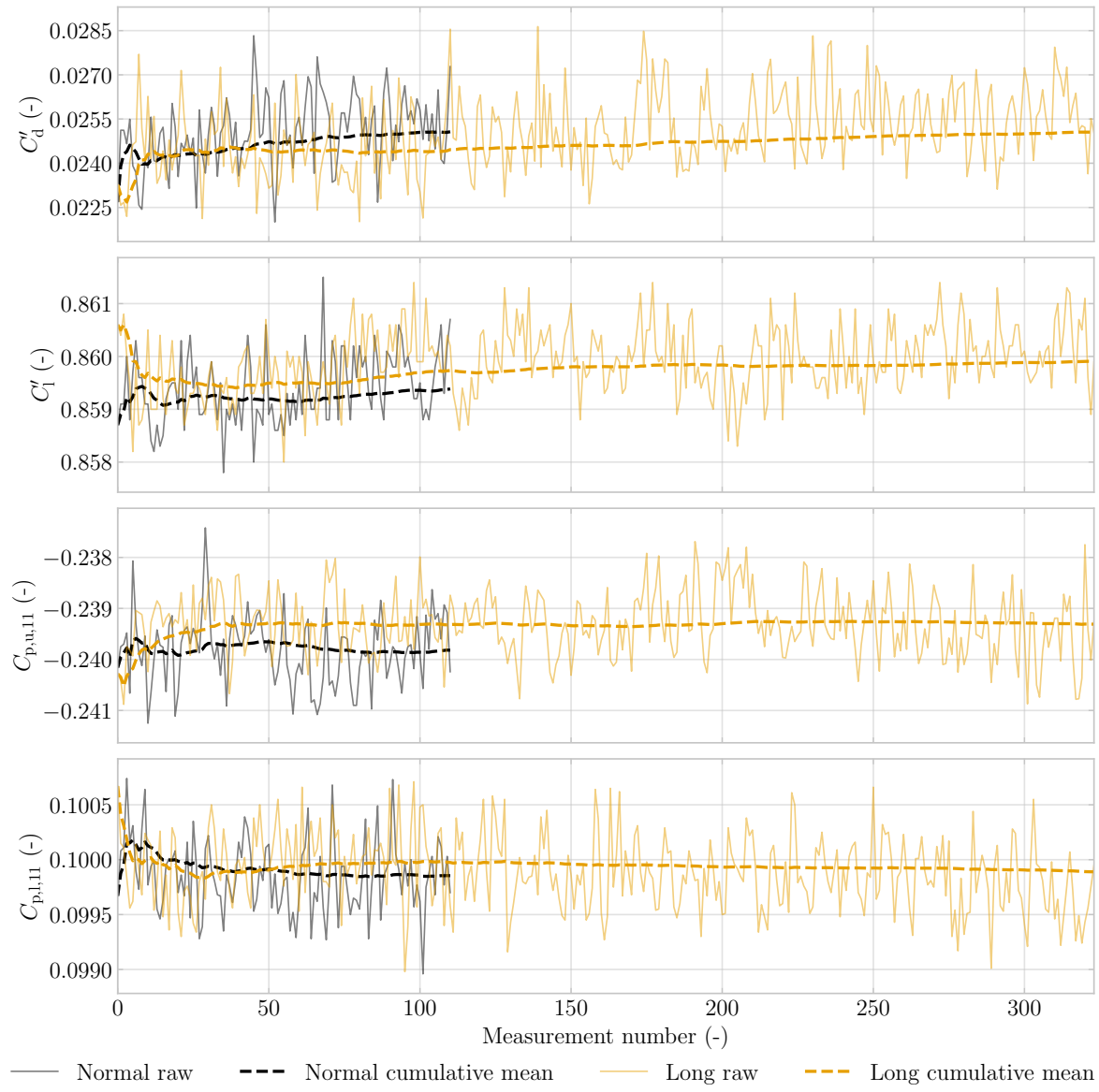

Figure 7.2: Long run validation for C'_d, C'_l, $C_{p,u,11}$ and $C_{p,l,11}$ for the V3 model at $\alpha = 5°$ and $\mathrm{Re} = 10^6$

From Fig. 7.2, it can be seen that both the normal (black) and long (orange) cumulative means converge toward stable values as more samples are included. This indicates that additional measurements beyond this point have a negligible influence on the average. The final values of the cumulative mean of the normal and long runs differ by at most 0.21%, as summarised in Table 7.1. This small variation shows that the chosen number of samples per measurement is sufficient to obtain a reliable mean value.

Table 7.1: Absolute percentage difference between long baseline and reruns at final cumulative mean

Parameter	% diff (long run)	% diff (rerun 1)	% diff (rerun 2)
C'_d	0.06%	0.34%	2.31%
C'_l	0.06%	0.11%	0.13%
$C_{p,u,11}$	0.21%	1.36%	0.86%
$C_{p,l,11}$	0.04%	0.10%	1.13%

7.1.3. Repeatability

To test the repeatability, the V3 model was tested with a zigzag tape at 5% of the chord on the top surface at $\mathrm{Re} = 10^6$. The test was performed at $\alpha = 10°$. In Fig. 7.3, the raw data and cumulative mean are plotted. As for the long run, the uncorrected lift and drag coefficient, as well as the middle pressure tab on the upper and lower surface, are plotted.

Rerun2 included a larger number of samples compared to the main run and Rerun1. However, since the cumulative mean converges toward a stable value after approximately 60 samples, this difference in sample count does not affect the validity of the repeatability check. This, however, does not hold for C'_d. The wake rake moves with a constant speed behind the airfoil, depending on the measurement length. As Rerun2 has more samples than the main run and Rerun1, this means that the wake rake has not traversed the entire model. This will influence the results for C'_d.

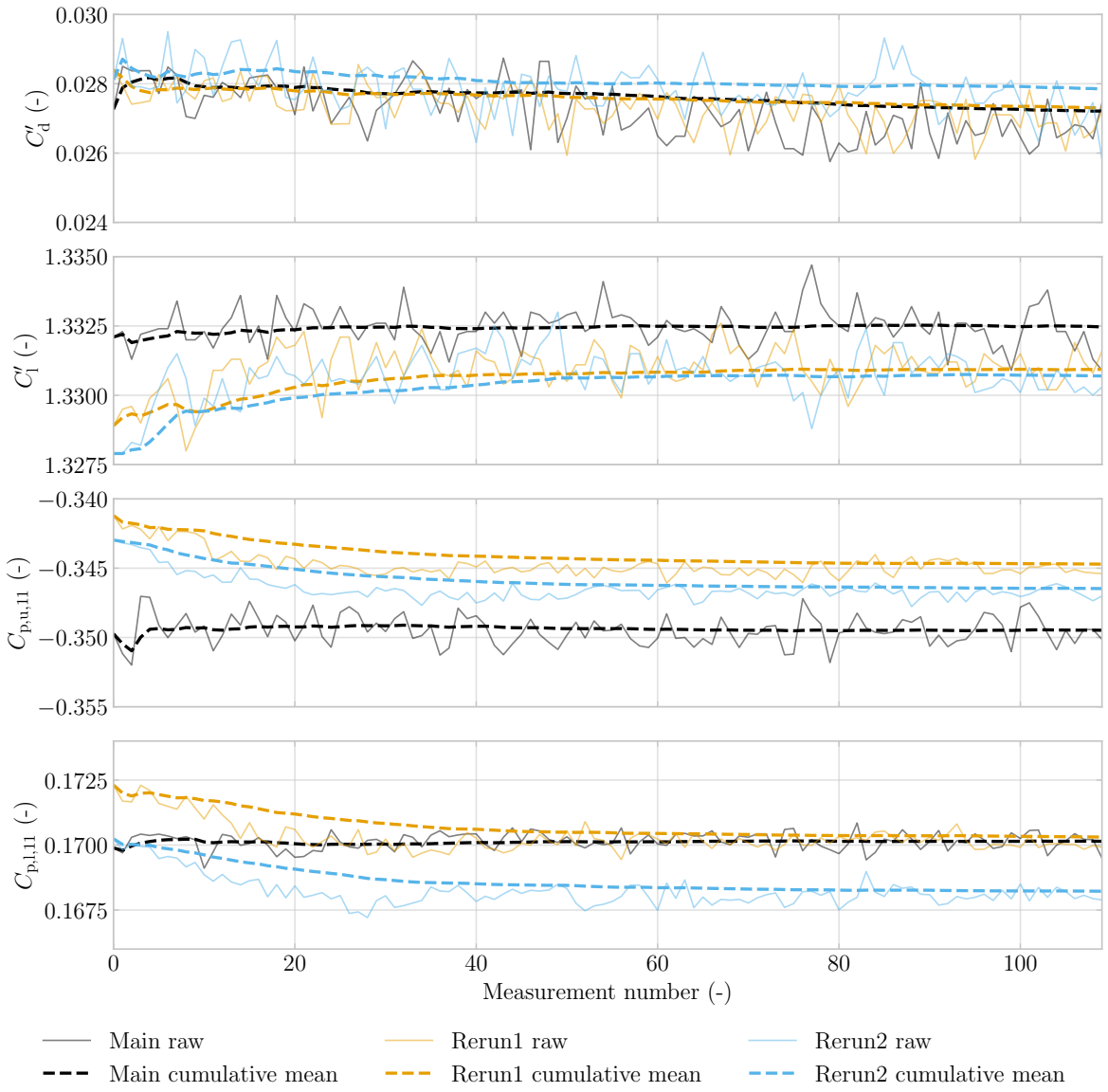

Figure 7.3: Repeatability validation for C'_d, C'_l, $C_{\mathrm{p,u,11}}$ and $C_{\mathrm{p,l,11}}$ for the V3 model with a zigzag on top at 5% at $\alpha = 10°$ and $\mathrm{Re} = 10^6$

With the cumulative mean, the difference between Rerun1 and Rerun2 with respect to the main run can be calculated. The percentage difference of the last value of the cumulative mean with both reruns

is tabulated in tab 7.1. The highest percentage difference is for C'_d with a value of 2.31%.When all the measurements of Rerun2 are used in the cumulative mean, the percentage difference of C'_d with respect to the main run reduces to 1.71%. The other differences are well below this value, indicating high measurement repeatability.

7.2. Airfoil polars

After the uncertainty analysis, the test runs were performed. In this section, the corrected experimental data explained in Ch. 6, is given for the V3 model and Model2 in the following subsections. Hereafter, the influence of Reynolds number is compared in Sect. 7.2.3. At last, the test cases without zigzag (ZZ) tape and the test case forcing a fully turbulent boundary layer are compared to CFD data in Sect. 7.2.4.

In the following figures, the solid line represents the corrected data. The X marks the angle of attack at which the wake rake cut-out. From this point onward, the data could not be corrected with the C'_d values, as these were not available. To still give a representation of the lift coefficient, the corrected data without C'_d correction is plotted as a dotted line.

7.2.1. V3 model

This subsection will cover the $C_l - \alpha$, $C_d - \alpha$, $C_l - C_d$ and $C_l/C_d - \alpha$ curves for the V3 model at $\mathrm{Re} = 5 \times 10^5$ and $\mathrm{Re} = 10^6$ in Fig. 7.4 and 7.5 respectively.

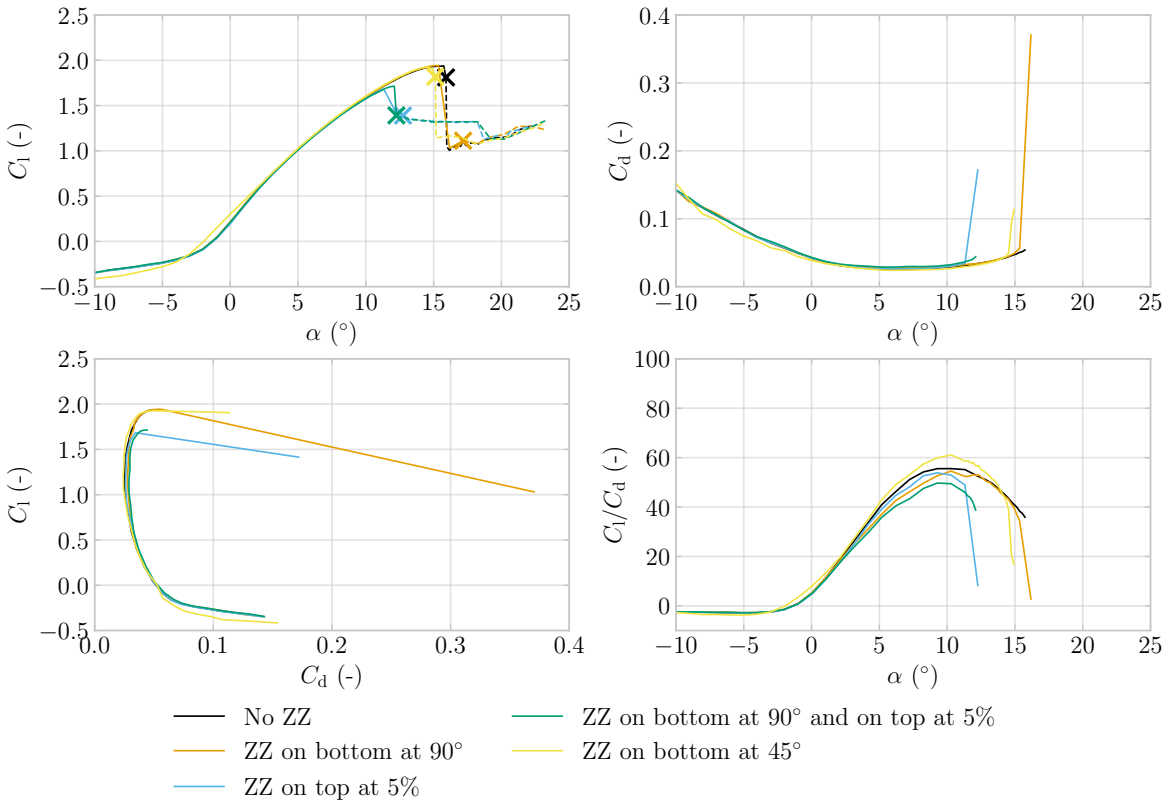

Figure 7.4: Airfoil polar for the V3 model at $\mathrm{Re} = 5 \times 10^5$ with $C_l - \alpha$ (top left), $C_d - \alpha$ (top right), $C_l - C_d$ (bottom left) and $C_l/C_d - \alpha$ (bottom right)

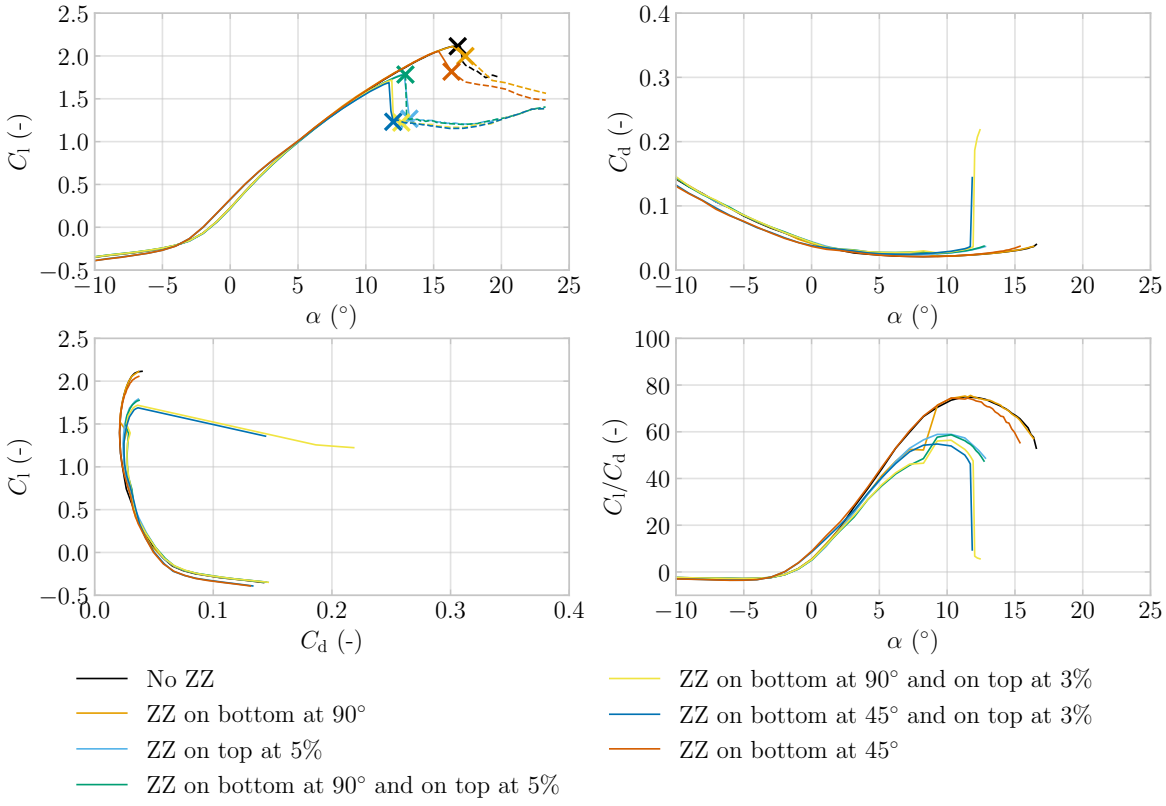

Figure 7.5: Airfoil polar for the V3 model at $\mathrm{Re} = 10^6$ with $C_l - \alpha$ (top left), $C_d - \alpha$ (top right), $C_l - C_d$ (bottom left) and $C_l/C_d - \alpha$ (bottom right)

For both figures, it becomes apparent that there are significant differences in the stall angle when a zigzag tape is applied to the top surface of the airfoil. When the zigzag tape is applied, the stall angle reduces with $\alpha = 3°$ with respect to the no zigzag case or when a zigzag tape is only applied to the LE-tube.

Furthermore, in Fig. 7.5, it is interesting to note the difference in drag coefficient when applying a zigzag tape on the bottom at $90°$. When the zigzag tape is applied exactly at the bottom of the LE-tube, there is little to no difference in the drag coefficient with respect to the case without zigzag tape. However, when the zigzag tape is applied under an angle of $45°$, the drag coefficient is visibly reduced from $\alpha = -10°$ to $\alpha = 2°$. It is hypothesized that the airflow around the LE-tube without zigzag tape results in laminar separation, which produces more drag than turbulent separation due to a higher adverse pressure gradient. When the zigzag tape is applied on the bottom at $90°$, the airflow should be tripped to a turbulent boundary layer, which should result in turbulent separation and thus a reduction in drag. As the C_d values for this case are the same, this suggests that the airflow did not have enough time to transition to a turbulent state or that the zigzag tape is located on the stagnation point. The zigzag tapes placed at $45°$ on the LE did give the airflow more time to transition to a turbulent boundary layer. This explains the reduction in drag coefficient when the zigzag tape is placed at an angle of $45°$. From $\alpha = 2°$ onward, the drag coefficient follows the curves where no zigzag is applied. This, again, could be that the zigzag tape is placed on the stagnation point. For higher angles of attack, the flow around the pressure side could start behind the zigzag tape, making the zigzag tape obsolete.

The lift coefficient for the $45°$ case is higher between $\alpha = -2°$ and $\alpha = 4°$ compared to the no zigzag cases. It is hypothesised that the reduction in recirculation zone and thus the increased attached flow area provides a higher lift coefficient. The recirculation zone grows in size with decreasing angles of attack. It is suspected that the recirculation zone from $\alpha = -10°$ to $\alpha = -2°$ is larger than the chord of the airfoil. Therefore, there is little to no difference in the lift coefficient. For angles of attack larger than $\alpha = 4°$, the reasoning is the same as for the drag coefficient.

At last, the $C_l - C_d$ curve shows the aerodynamic performance of each configuration. It follows logically from the $C_l - \alpha$ and $C_d - \alpha$ curves that the configuration without zigzag tapes is the best performing. Following it are the configurations with the zigzag tape placed only on the LE-tube. These configurations do perform a bit worse as the zigzag tape introduces more drag than the clean configuration.

7.2.2. Model2

This subsection will cover the $C_l - \alpha$, $C_d - \alpha$, $C_l - C_d$ and $C_l/C_d - \alpha$ curves for Model2 at $\mathrm{Re} = 5 \times 10^5$ and$\mathrm{Re} = 10^6$ in Fig. 7.6 and 7.7 respectively.

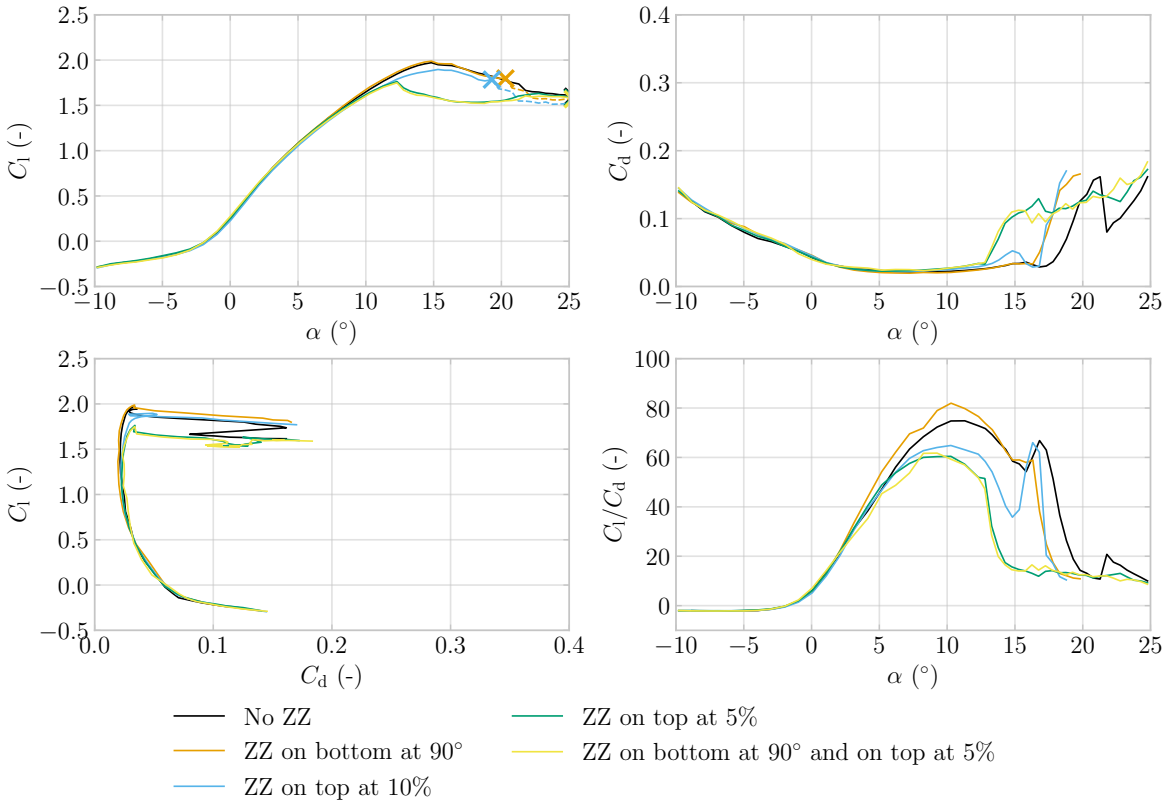

Figure 7.6: Airfoil polar for Model2 at $\mathrm{Re} = 5 \times 10^5$ with $C_l - \alpha$ (top left), $C_d - \alpha$ (top right), $C_l - C_d$ (bottom left) and $C_l/C_d - \alpha$ (bottom right)

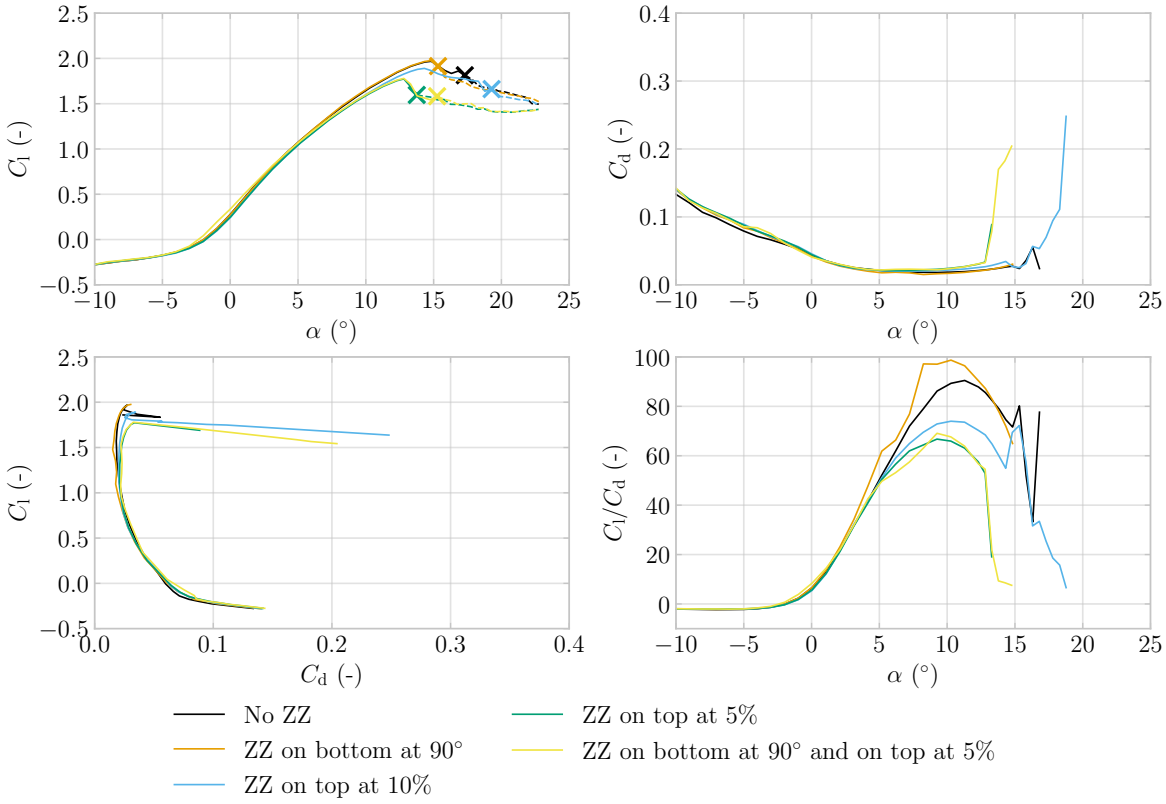

Figure 7.7: Airfoil polar for Model2 at $\mathrm{Re} = 10^6$ with $C_l - \alpha$ (top left), $C_d - \alpha$ (top right), $C_l - C_d$ (bottom left) and $C_l/C_d - \alpha$ (bottom right)

As for the V3 model, the zigzag tape on the top surface has a negative effect on the stall angle and thus the maximum lift coefficient. It is interesting to note that the zigzag tape located at 10% of the chord on the top surface has a less pronounced influence on the stall angle and lift coefficient than the zigzag tape placed at 5% of the chord on the top surface. This could be due to the fact that the flow naturally transitions prior to 10% of the chord on the top surface. This means that the zigzag tape is located inside the turbulent boundary layer and will only increase drag and have little influence on the lift coefficient. The increase in drag around stall angle can also be seen in the $C_d - \alpha$ graph.

Furthermore, just like the V3 model, the zigzag tape located on the LE has a negligible influence on the lift coefficient with respect to the case without zigzag tape. The LE-tube zigzag tape does create more drag in the deep-stall at $\mathrm{Re} = 5 \times 10^5$, as opposed to the no zigzag case. This could be due to the larger exposure of the zigzag tape when the airfoil is pitched into deep-stall.

7.2.3. Reynolds comparison

In Fig. 7.8 and 7.9, the results for two different cases are provided, both for $\mathrm{Re} = 5 \times 10^5$ and $\mathrm{Re} = 10^6$ for the V3 model and Model2, respectively. These figures give an insight into the influence of Re-number on the aerodynamic characteristics. The shown cases are the no zigzag case and the zigzag placed at 5% of the chord on the top surface and on the bottom of the LE-tube.

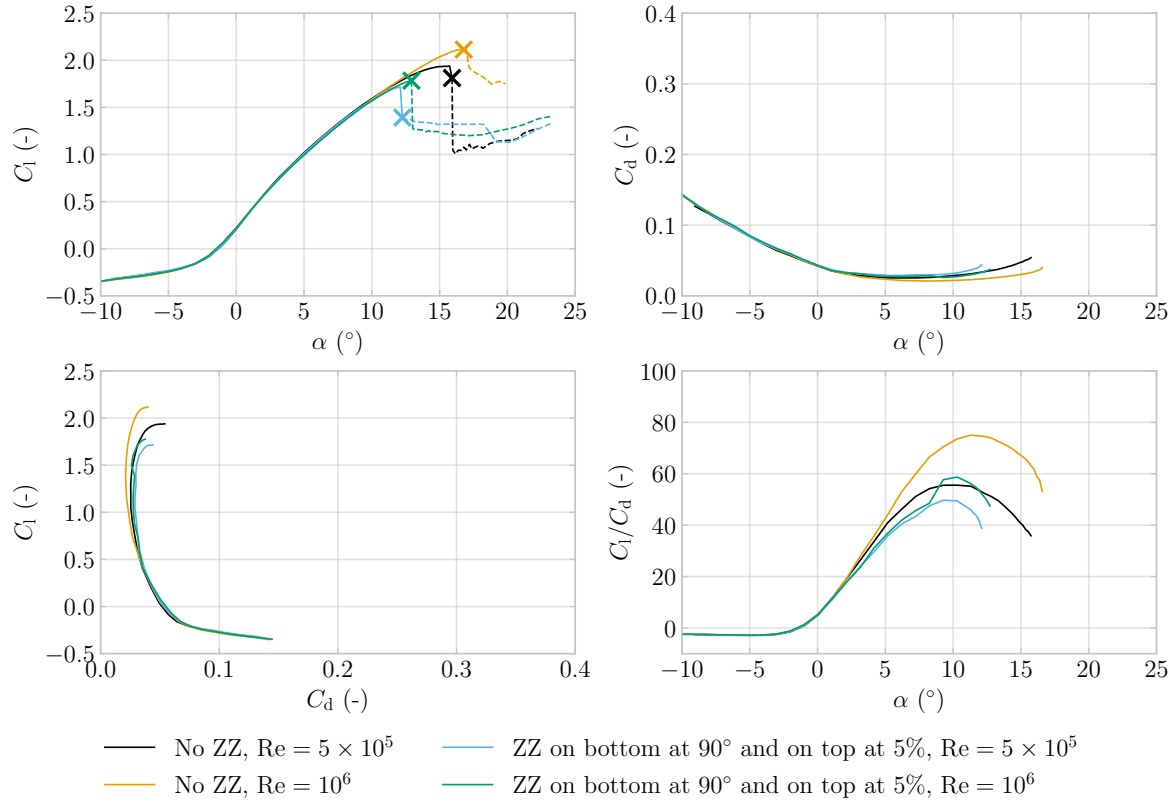

Figure 7.8: Airfoil polar for V3 model comparison between $\mathrm{Re} = 5 \times 10^5$ and $\mathrm{Re} = 10^6$ with $C_l - \alpha$ (top left), $C_d - \alpha$ (top right), $C_l - C_d$ (bottom left) and $C_l/C_d - \alpha$ (bottom right)

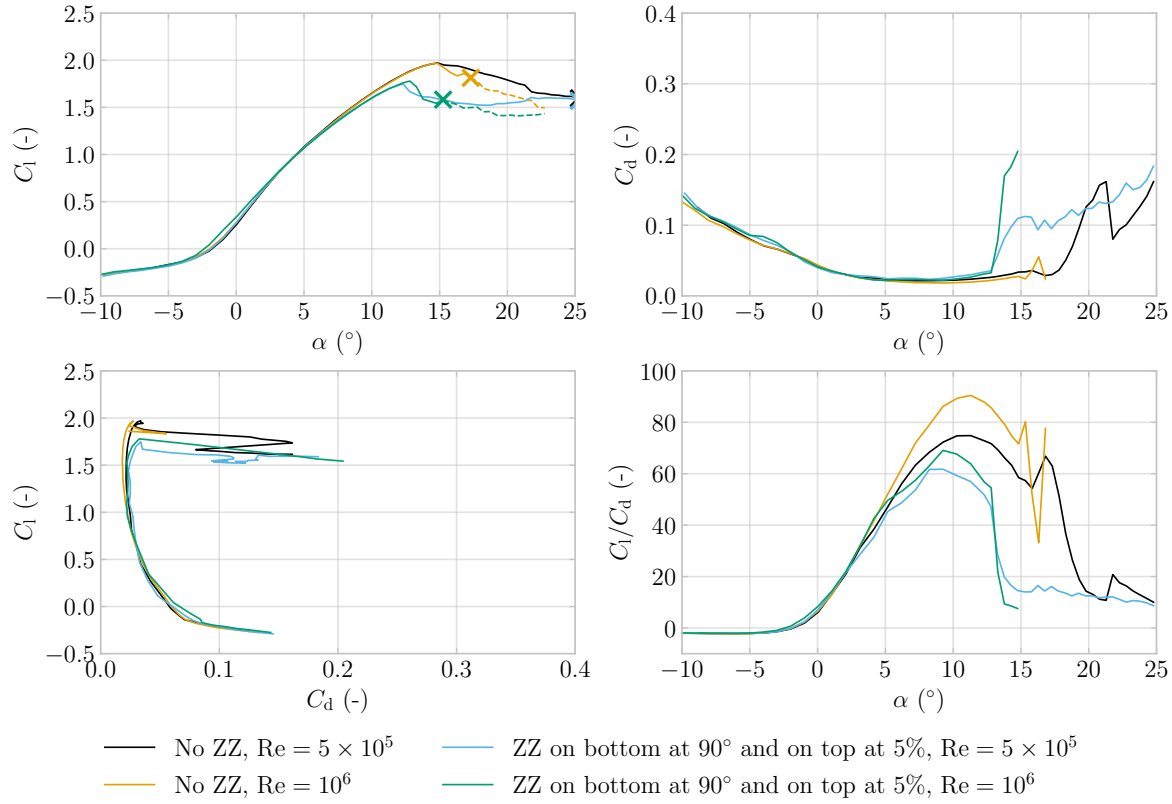

Figure 7.9: Airfoil polar for Model2 comparison between $\mathrm{Re} = 5 \times 10^5$ and $\mathrm{Re} = 10^6$ with $C_l - \alpha$ (top left), $C_d - \alpha$ (top right), $C_l - C_d$ (bottom left) and $C_l/C_d - \alpha$ (bottom right)

As in the CFD analysis by Folkersma [22], the differences between $\mathrm{Re} = 5 \times 10^5$ and $\mathrm{Re} = 10^6$ for both the V3 model and Model2 are small but notable. It becomes clear that with a higher Reynolds number, the stall angle increases around $1°$ with a small increase in maximum lift coefficient.

For both models, the case without zigzag tape at $\mathrm{Re} = 10^6$ is the best performing configuration. The maximum C_l/C_d value is 75 and 90 for the V3 model and Model2 respectively. This is around 20 higher than the other highest case.

The C_l value for all cases of the V3 model is almost identical between $\alpha = -10°$ and $\alpha = 10$. From $\alpha = 2°$ onwards, the C_d value changes slightly between the different cases. For the Model2 the C_l is similar between $\alpha = -10°$ and $\alpha = 6$ whereas the C_d is different. The difference in Reynolds number has a less pronounced effect in the linear parts of the lift polar. The differences occur towards higher angles of attack.

7.2.4. Comparison with CFD data

The experimental data obtained from the wind tunnel test is compared with numerically obtained data by performing RANS simulations using the CFD toolchain created by Masure [15]. As said in Sect. 3.3, the numerical simulations have been run for the V3 and Model2 at $\mathrm{Re} = 5 \times 10^5$ and $\mathrm{Re} = 10^6$ using a transition model and for the V3 at $\mathrm{Re} = 10^6$ assuming a fully turbulent flow. From the wind tunnel analysis, five different cases are compared to the CFD data. The V3 model with zigzag tapes at 3% of the chord on the top surface and $45°$ on the bottom LE-tube can be used to compare the CFD data with the assumption of a fully turbulent boundary layer. Furthermore, for both the V3 model and Model2, the cases without zigzag tapes at $\mathrm{Re} = 5 \times 10^5$ and $\mathrm{Re} = 10^6$ are compared to the CFD results, which included the transition model.

In each figure, the grey-shaded area represents the 99.7% confidence interval (CI) around the mean, corresponding to three times the standard deviation of the mean. The standard deviation was calculated

based on all corrected raw data. When the wake became too large, the wake rake could not measure the drag coefficient anymore. This resulted in missing data points for the drag coefficient, whereas the lift coefficient could still be measured. However, in Eq. 6.12, the lift coefficient had to be corrected with the drag coefficient. To still give an indication of what the lift coefficient could be, the lift coefficient is corrected with the drag coefficient obtained from CFD data. This is visualised by the red line. The red shaded area shows the lift coefficient when the data was corrected with 0 and 2 times the drag coefficient of the CFD data.

Figure 7.10 shows the wind tunnel (WT) data of the V3 model with zigzag tapes placed towards the LE and the CFD data assuming a fully turbulent boundary layer. It can be seen that the data matches between $\alpha = -2°$ and $\alpha = 12°$. The maximum lift coefficient matches well with the CFD data, although the maximum stall angle differs by $2°$. After stall, the C_l data follows the same trend as the CFD data, but as stall occurs earlier, the data is shifted by $2°$. At $\alpha = 12°$, the C_d spikes to 0.2 with the CI going from 0 to 0.3. This measurement should be omitted as the data has a high uncertainty. With larger negative angles of attack, the CFD overestimates the lift coefficient. The CFD estimate for the drag coefficient falls within the 99.7% CI up until stall. After this, the wake became too large, so the drag coefficient could not be measured anymore.

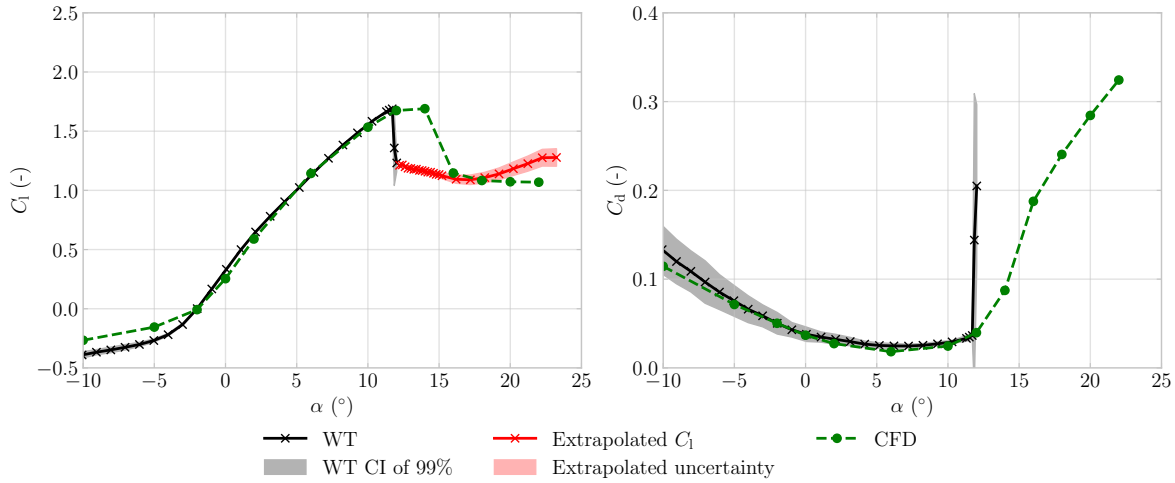

Figure 7.10: Airfoil polars for the V3 model with zigzag tape on bottom at $45°$ and on top at 3% at $\mathrm{Re} = 10^6$ compared to CFD results

Figure 7.11 till 7.14 show the experimental results without zigzag tape in comparison with the CFD results, including a transition model for the V3 model and Model2 for $\mathrm{Re} = 5 \times 10^5$ and $\mathrm{Re} = 10^6$. During the CFD simulations, multiple angles of attack did not converge using the transition model. These data points are left out of the comparison. For the V3 model in Fig 7.11 and 7.12, the CFD data greatly undershoots the experimental data both in maximum lift coefficient and maximum stall angle. As the data points for the linear part of the lift slope are not available, no conclusion can be drawn for this part of the lift curve. For both Re-numbers at $\alpha = 6°$, the lift and drag coefficients agree well, suggesting a better match in the linear region. Again, for Fig 7.11, the drag coefficient spikes just after stall. As with the previous model, this measurement should be omitted.

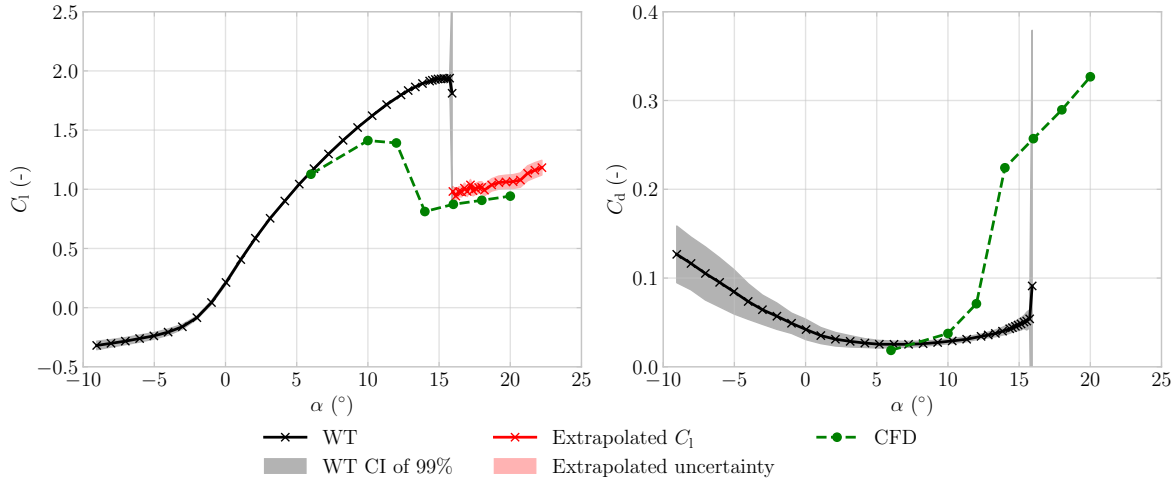

Figure 7.11: Airfoil polars for the V3 model without zigzag tape at $\mathrm{Re} = 5 \times 10^5$ compared to CFD results

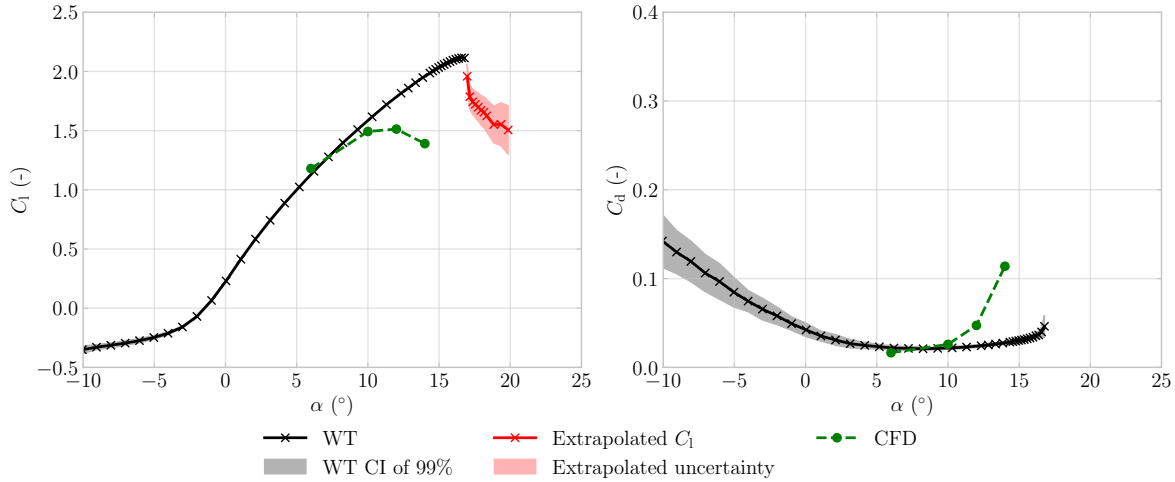

Figure 7.12: Airfoil polars for the V3 model without zigzag tape at $\mathrm{Re} = 10^6$ compared to CFD results

Figure 7.13 and 7.14 show Model2 at $\mathrm{Re} = 5{\times}10^5$ and $\mathrm{Re} = 10^6$ respectively. Unlike the V3 model, the CFD data models the stall angle relatively well. However, the maximum lift coefficient still undershoots with this transition model. For the $\mathrm{Re} = 5 \times 10^5$ case, more data points converged at lower angles of attack. The CFD data shows a similar lift slope and drag values between $\alpha = 2°$ and $\alpha = 6°$ as the experimental data.

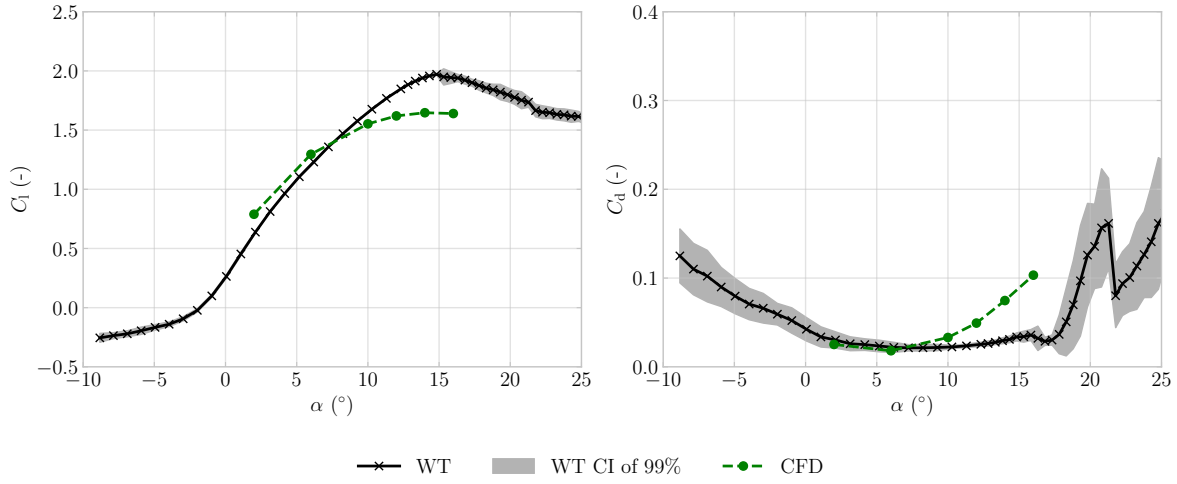

Figure 7.13: Airfoil polars for Model2 without zigzag tape at $\mathrm{Re} = 5 \times 10^5$ compared to CFD results

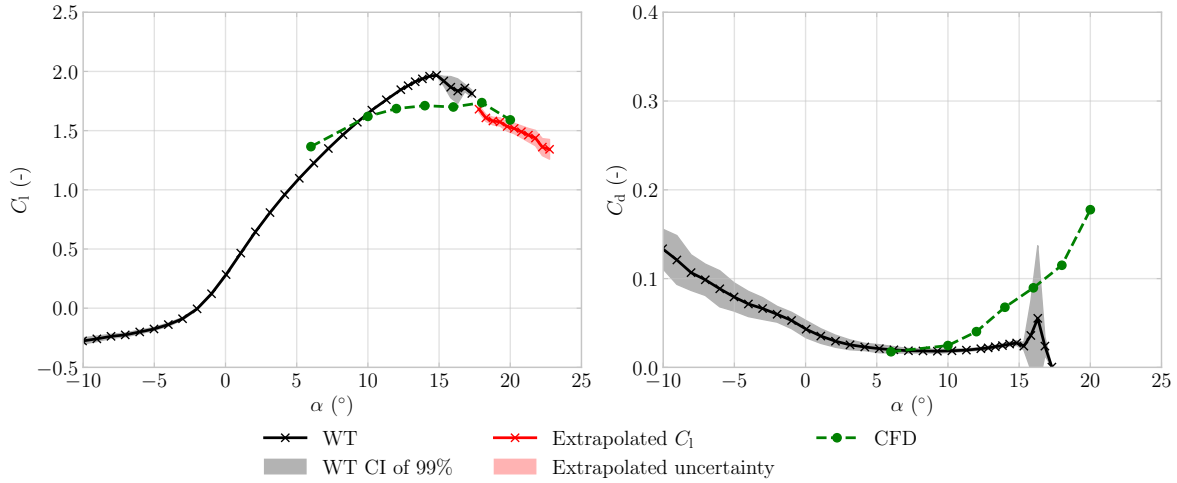

Figure 7.14: Airfoil polars for Model2 without zigzag tape at $\mathrm{Re} = 10^6$ compared to CFD results

7.3. Infrared imaging

In Fig. 7.15, the location of transition is plotted versus α for the V3 model and Model2 at $\mathrm{Re} = 5 \times 10^5$ and $\mathrm{Re} = 10^6$. The location of transition is a percentage of the chord from the LE. The difference in transition location becomes clear with different Re-numbers. With lower Re-numbers, the viscous forces dominate over inertial forces. This results in a stable laminar boundary layer which delays transition. This holds for the entire angle of attack range. Interesting to observe is the almost constant location of the transition point from $\alpha = 3°$ onward. This is both for the $\mathrm{Re} = 5 \times 10^5$ and $\mathrm{Re} = 10^6$. The reason for this constant location of separation is unknown, but it could be due to the effect of the geometry of the V3 model. The sharp curvature towards the leading edge of the airfoil could create a high adverse pressure gradient which could result in a laminar separation bubble. Unlike the V3 model, the location of transition gradually moves upstream with increasing angles of attack for Model2. It is hypothesized that due to the more gradual curvature of the Model2 than the V3 model, the flow does not encounter an high adverse pressure gradient and therefore, not creating a laminar separation bubble.

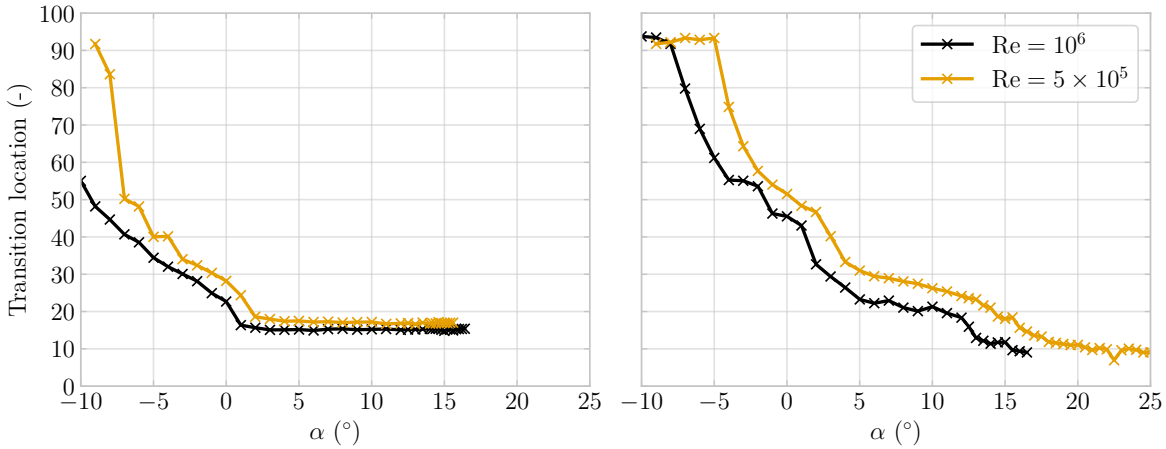

Figure 7.15: Location of transition vs α for the V3 model (left) and Model2 (right).

7.4. Oil flow visualisation

Oil flow visualisation was used to gain a better understanding of the flow around the LEI airfoil. The oil flow visualisation was performed at $\mathrm{Re} = 10^6$ at multiple angles of attack. First, the flow topology around a LEI airfoil is explained in Subsect 7.4.1. Second, the figures of the suction side are shown in Sect. 7.4.2, and lastly, the figures of the pressure side are shown in Sect. 7.4.3. The oil flow visualisation tests were performed in a clean configuration and with a zigzag tape configuration to show the difference the zigzag tape makes.

7.4.1. Flow topology

Before showing the results of the suction and pressure side under different angles of attack, the different regions should be identified. In Fig. 7.16, the suction and pressure sides of the V3 model can be seen with lines indicating specific regions.

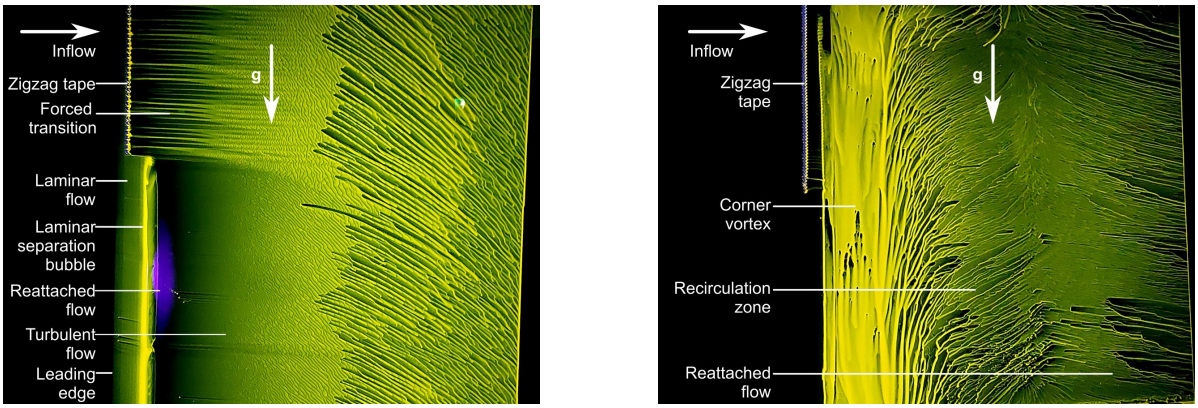

Figure 7.16: Oil flow for the V3 model indicating specific regions on the suction side (left) and pressure side (right).

Starting with Fig. 7.16, it is clearly visible that the zigzag tape does indeed trip the boundary layer into a turbulent boundary layer on the suction side. Next to this, as expected by Folkersma et al. [22], there is a formation of a laminar separation bubble after which the flow transitions into a turbulent boundary layer. In this figure, the surface imperfections also become visible. In the region without zigzag tape, multiple small black streaks can be seen when the flow is turbulent. This indicates surface imperfections upstream. This will have a negative effect on the aerodynamic performance of the airfoil. The purple

area on the suction side is the reflection of the UV-light on the model.

For the pressure side, the corner eddy is visible. As the velocity of this eddy is small, therefore the oil accumulates and flows down due to gravity. After this, the recirculation zone causes the oil to flow towards the LE. The reattachment zone of the recirculation zone is also clearly visible, as this is the line where the direction of the oil returns to streamwise direction. This produces a christmas tree-like pattern. It can be noted, however, that the zigzag tape at the pressure side of the LE-tube has little to no influence on the streamline pattern created by the oil. This will be further discussed in Sect. 7.4.3.

7.4.2. Suction side

In Fig. 7.17, the flow is visualized on the suction side of the V3 model at $\alpha = 2°$ and $\alpha = 11°$. Both angles of attack are before stall, which can be seen by the streamline pattern following the inflow direction. As expected, at both angles of attack, the zigzag tape successfully trips the flow into a turbulent boundary layer.

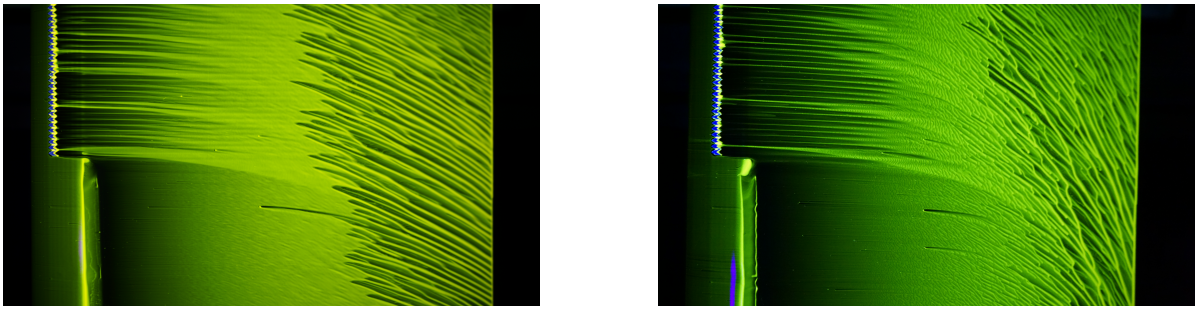

Figure 7.17: Oil flow for the suction side of the V3 model at $\alpha = 2°$ (left) and $\alpha = 11°$ (right).

When testing the airfoil at $\alpha = 14°$ and $\alpha = 17°$, an notable flow pattern occurred. According to the lift polars in Fig. 7.5, the zigzag tapes caused the LEI airfoil to stall at $\alpha = 12°$ whereas the no zigzag airfoil stalled at $\alpha = 16°$. This should be visible in streamline patterns on the suction side of the airfoil.

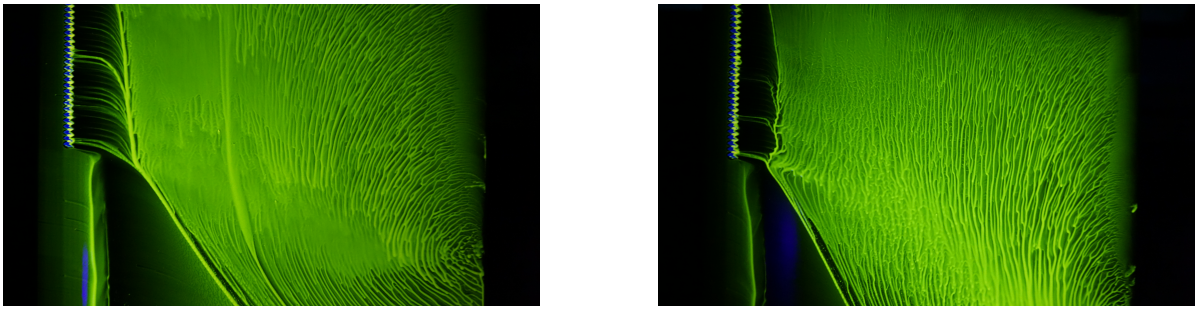

Figure 7.18: Oil flow visualisation for the suction side of the V3 model at $\alpha = 14°$ (left) and $\alpha = 17°$ (right).

In Fig. 7.18, the accumulation of oil behind the zigzag tap indicates a region of separation as the skin friction coefficient is low. Because the oil naturally flows downward due to gravity, it interferes with the oil flow in the part without zigzag tape. It is, however, visible that after the transition region, where the oil is swept away, streamlines occur. This indicates the turbulent boundary layer. The airfoil without zigzag tape has not yet stalled opposed to the zigzag part.

Looking at the $\alpha = 17°$ case in Fig. 7.18, the same streamline pattern behind the zigzag tape can be seen, indicating separation. The part without zigzag tape again shows a transition region, but the accumulation of oil starts sooner with respect to the $\alpha = 14°$ case. This suggests that separation does occur, but occurs more towards the trailing edge than the part with the zigzag tape.

Near the trailing edge in Fig. 7.18, the streamlines form half-circles. These could be formed due to stall cells over the airfoil. The size of the stall cells depends on the angle of attack of the airfoil as well as the aspect ratio of the airfoil. According to Weihs & Katz, the number of stall cells reduces with a smaller aspect ratio [57].

7.4.3. Pressure side

The V3 model has been tested with visualisation oil at the angles $\alpha = -5°$, $2°$, $11°$ and $17°$ on the pressure side of the airfoil. Figure 7.19 shows the results of the oil at $\alpha = -5°$ and $\alpha = 2°$ and Fig. 7.20 shows the results of $\alpha = 11°$ and $\alpha = 17°$.

In Fig. 7.19, it becomes clear that the corner eddy is quite large with $\alpha = -5°$. After the corner eddy, the recirculation zone is visible. The recirculation zone is too large to attach to the airfoil again. This is the reason that the oil lines after the corner eddy point flow upstream. At $\alpha = 2°$, the corner eddy, recirculation zone, and the attachment of this recirculation zone become visible again.

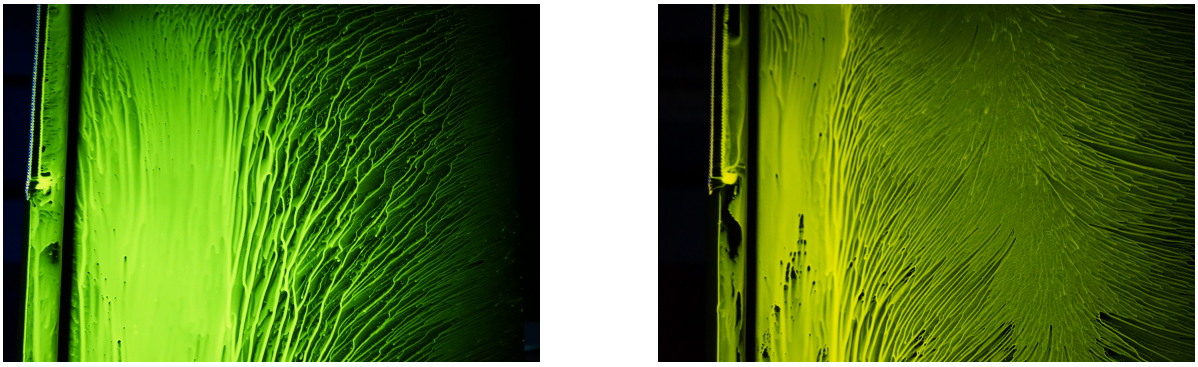

Figure 7.19: Oil flow for the suction side of the V3 model at $\alpha = -5°$ (left) and $\alpha = 2°$ (right).

As said in Sect. 7.2.1, when a zigzag tape is placed under an angle of $45°$, the drag coefficient is reduced with respect to the case without zigzag tape from $\alpha = -10°$ to $\alpha = 2°$. It was hypothesised that the airflow did not have enough time to transition into a turbulent state, which resulted in laminar separation, causing a higher drag coefficient. Fig. 7.19 at $\alpha = -5°$ shows a clear distinction in separation along the LE-tube, where the zigzag tape delays separation, contrary to the no zigzag tape. The oil behind the zigzag tape is swept away, indicating a transition into a turbulent flow. This difference could confirm the aforementioned hypothesis.

Figure 7.19 at $\alpha = 2°$ shows a slight difference in the location of separation. According to Fig. 7.5, there is still a small difference in C_{d} at $\alpha = 2°$. Interesting to note is the difference in the recirculation zone behind the zigzag tape and the clean configuration. The centre of the so-called Christmas tree pattern behind the zigzag tape is more towards the LE compared to the clean configuration. As the flow behind the zigzag tape is attached for longer to the LE-tube, the recirculation zone decreases in size. This reduction in recirculation zone could explain the slight increase in C_1 seen in Fig. 7.5.

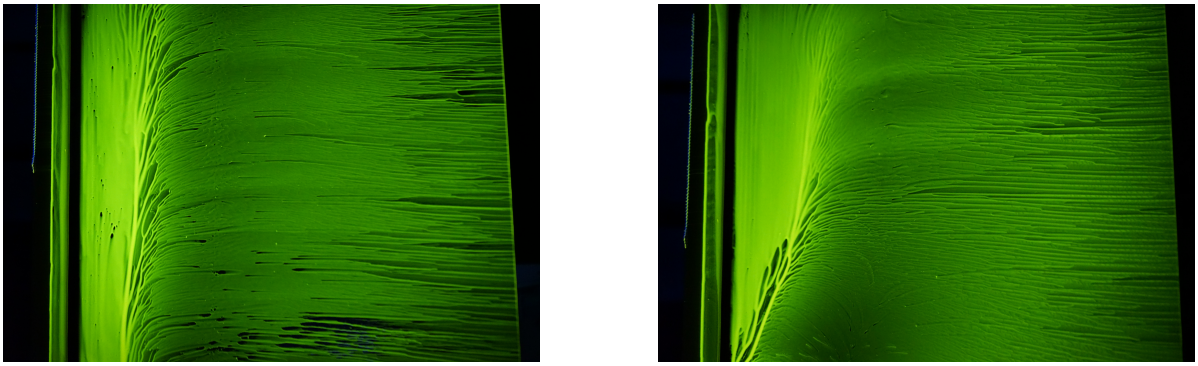

(a) (b)

Figure 7.20: Oil flow for the suction side of the V3 model at $\alpha = 11°$ (left) and $\alpha = 17°$ (right)

In Fig. 7.20, the oil flow visualisation at $\alpha = 11°$ and $\alpha = 17°$ can be seen. Unlike Fig. 7.19 the separation location is the same behind the zigzag tape as well as the clean configuration in Fig. 7.20. because of this, the recirculation zone at $\alpha = 11°$ has the same size with or without zigzag tape. This also explains the negligible difference between the lift and drag coefficient at $\alpha = 11°$ in Fig. 7.5.

At $\alpha = 17°$, a significant difference in the corner eddy just behind the LE-tube can be seen. It is suspected that the rib supporting the canopy has an effect on the airflow along the pressure side of the airfoil.

7.5. Boundary layer comparison with CFD

The following figure, Fig. 7.21, shows a comparison of the experimentally visualised boundary layer with the CFD results. From top to bottom, the figure shows the velocity field including streamlines, suction side oil flow visualisation with forced and free transition, the infrared image of the suction side, the pressure and the wall friction coefficient plot and the oil flow visualisation of the pressure side for $\alpha = 2°$ and $\alpha = 8°$. The images are cropped so that the leading and trailing edge lines up for every image. The red line in the C_p/C_f-plot shows the friction coefficient along the suction and pressure side. When the coefficient is zero, this means that the flow is separated. For the suction side, this is a separated flow, but on the pressure side, this indicates a corner eddy. When the friction coefficient is negative, it means that there is flow reversal and thus a recirculation zone.

With the oil flow visualisation on the suction side right above the infrared image, it can be seen that the laminar part of the boundary layer matches perfectly. The location of transition is not possible to see in the C_p, C_f-plot, as the CFD simulations are performed assuming a fully turbulent boundary layer.

The dashed lines indicate when the friction coefficient is negative. This, as said before, indicates the recirculation zone of the LEI airfoil. It is difficult to model the reattachment point using CFD, but in Fig. 7.21, the size of the recirculation zone for both angles match quite well.

It can be observed that, on the suction side, the oil towards the trailing edge tends to flow downward more at $\alpha = 8°$. When the airflow separates, the friction coefficient goes to zero. This means that the oil will accumulate where the airflow is separated. With the accumulated oil, gravity will drag it downward, creating oil flow streaks in the downward direction. When looking at the C_f-plot for both $\alpha = 2°$ and $\alpha = 8°$, it can be seen that the friction coefficient towards to trailing edge is closer to zero than for the $\alpha = 2°$ case. This explains the difference in oil flow towards the trailing edge between the two cases.

Just like the suction side, the pressure side streamlines in the recirculation zone at $\alpha = 2°$ tend to flow downward. The reason for this is in the friction plot as well. The value of the friction coefficient is just below zero. This means that gravity drags the oil downward. In the $\alpha = 8°$ case, the slope of the friction coefficient is very steep and the friction coefficient is more negative. This means that gravity influences the oil less, and thus the streamlines are more horizontal.

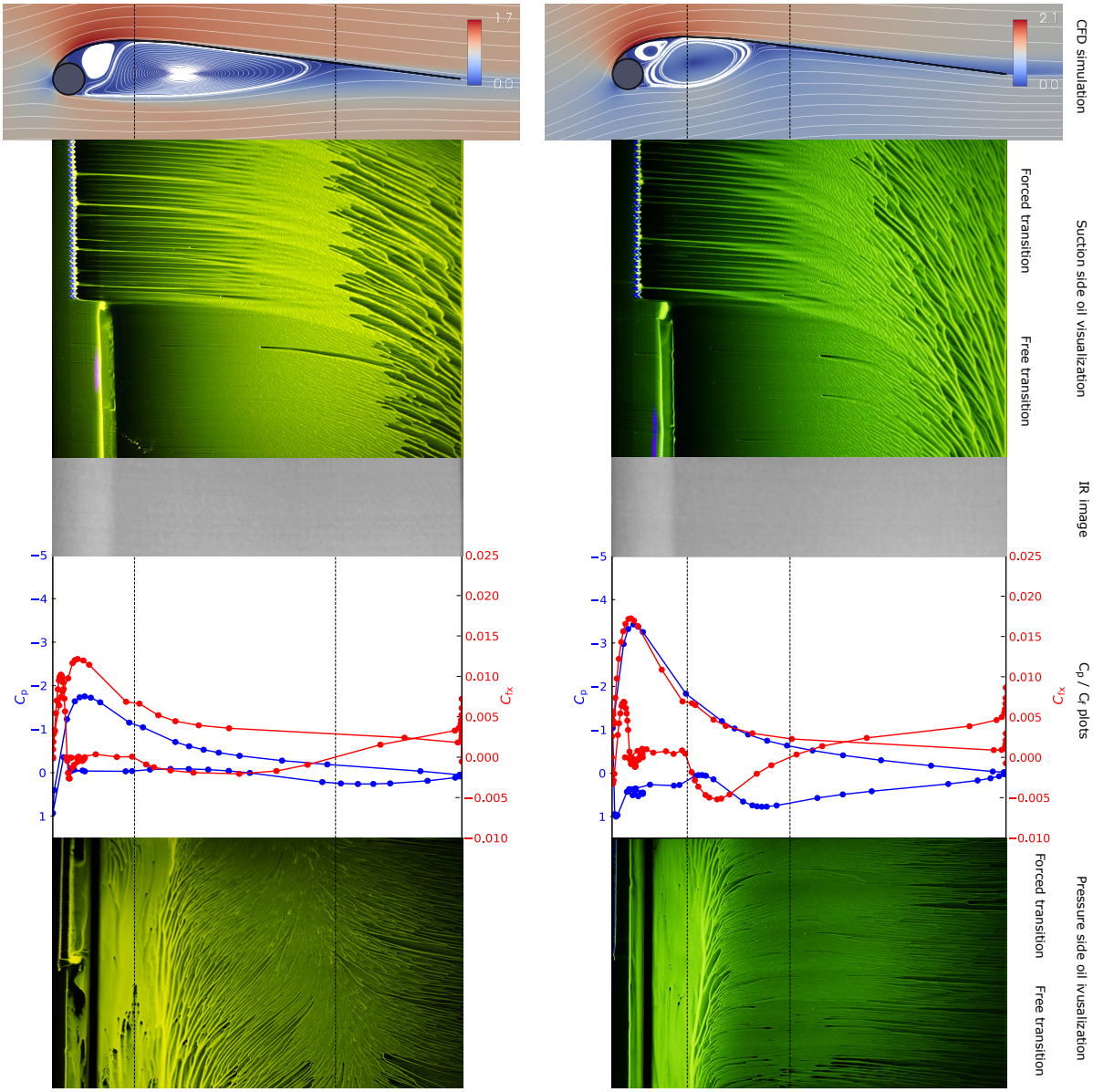

Figure 7.21: Boundary layer comparison with CFD for the V3 model at $\alpha = 2°$ (left) and $\alpha = 8°$ (right) at $\mathrm{Re} = 10^6$.

Figure 7.22 shows the comparison of the boundary layer with the CFD results for $\alpha = -5°$ and $\alpha = 14°$. The oil flow visualisation figure of the suction side at $\alpha = -5°$ has not been taken and is therefore missing from this figure.

This figure shows that the CFD simulation at $\alpha = -5°$ does not capture the corner eddy. Instead, the CFD simulation predicts a recirculation zone that extends over the entire chord, while the oil flow visualisation on the pressure side indicates that the recirculation zone only covers the second half of the chord. The first half is occupied by the corner eddy.

In the $C_\mathrm{p}/C_\mathrm{f}$-plot of $\alpha = 14°$, the estimation of the recirculation zone matches. As said before, the size of the corner eddy is distorted. This is most likely due to the rib influencing the airflow. Interesting to note is the location of separation on the suction side. The red dashed line indicates where the friction coefficient becomes zero. This dashed line is close to the separation point behind the zigzag tape.

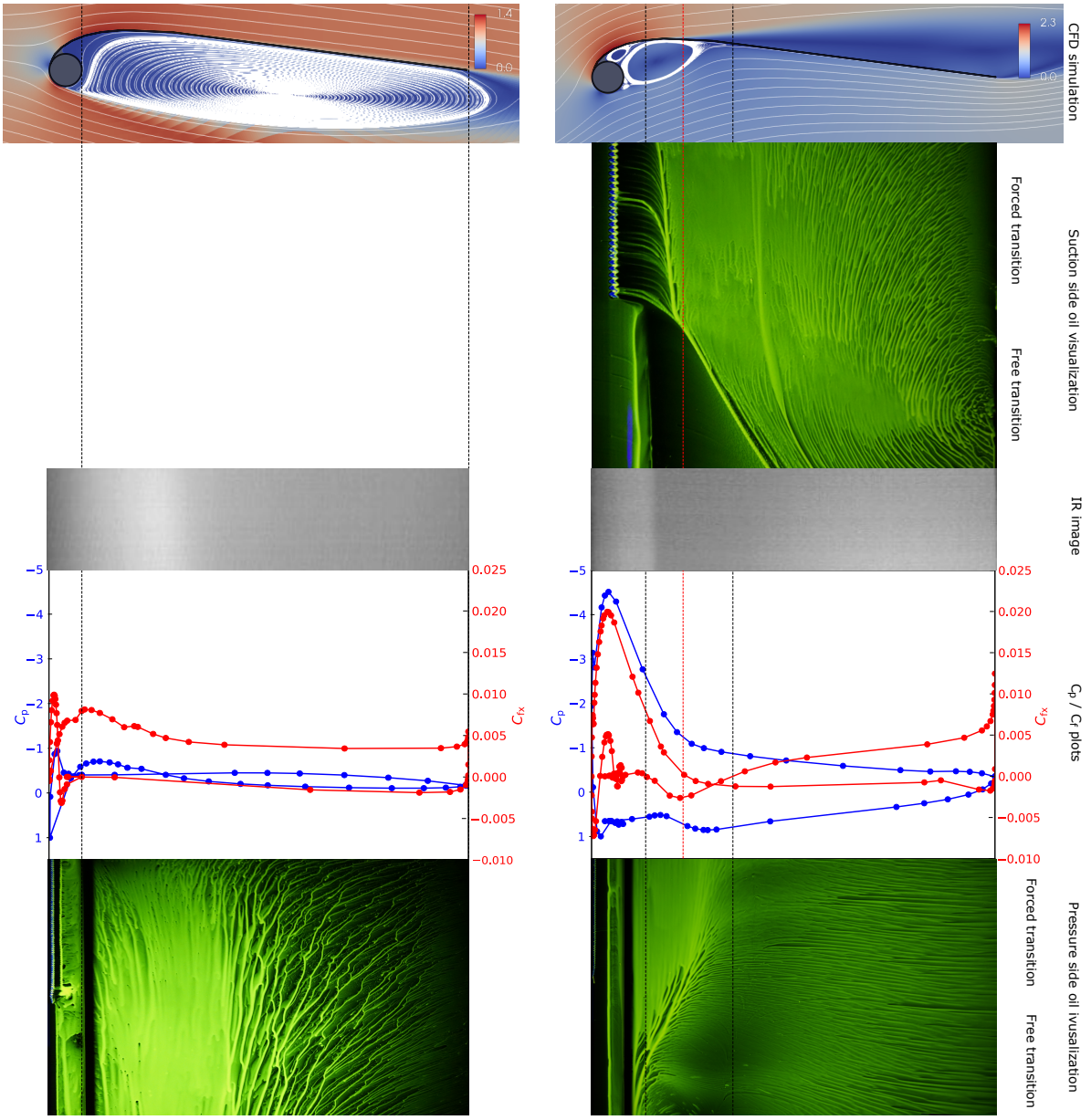

Figure 7.22: Boundary layer comparison with CFD for the V3 model at $\alpha = -5°$ (left) and $\alpha = 14°$ (right) at $\mathrm{Re} = 10^6$.

8

Conclusions and Recommendations

This report describes a first attempt to experimentally characterize the aerodynamics of 2D rigid LEI airfoils in a wind tunnel, and using this data to validate 2D Reynolds-Averaged Navier Stokes (RANS) simulations.

Two different airfoil scale models were designed, manufactured and tested at $\mathrm{Re} = 5 \times 10^5$ and $\mathrm{Re} = 10^6$. The aerodynamic coefficients were measured using a wake rake and pressure strips on the test section wall. The numerical data was obtained using RANS simulations with either the $\gamma - \tilde{\mathrm{Re}}_{\theta \mathrm{t}}$ transition model or with the assumption of a fully turbulent boundary layer.

This chapter outlines the main conclusions of this thesis, answering the research questions listed in Ch. 2. Next to this, recommendations will be given for future work based on the findings of this thesis.

8.1. Conclusion

Prior to testing, an uncertainty analysis was performed to check on hysteresis effects, measurement duration and repeatability. Hysteresis only showed a deviation of 0.1 of the uncorrected lift coefficient at $\alpha = 16°$. The maximum percentage difference in cumulative mean of the measurement duration and repeatability was 0.21% and 1.71%. This shows that the experimental data has a low uncertainty and can be used for the validation of the numerical data.

The zigzag tape experiments showed that tripping the boundary layer on the suction side strongly reduces both the maximum lift and stall angle, while having minimal effect on drag before stall. In contrast, tripping the flow on the lower side of the leading edge tube has a positive influence on the low-angle-of-attack region, likely by reducing the recirculation zone. These observations show the sensitivity of LEI airfoils to boundary-layer transition and demonstrate the potential of controlled tripping to increase the aerodynamic performance.

The experimental campaign characterised the influence of the Reynolds number on the aerodynamic behaviour of LEI airfoils. The results confirmed what is known from literature [22], that an increase in Reynolds number results in a higher maximum lift coefficient and delayed stall.

The comparison with CFD data showed good agreement for the fully turbulent case, supporting the validity of the CFD toolchain under this assumption. However, discrepancies appeared in the post-stall region, which are inherently difficult to capture with RANS simulations. When the transition model was included, the simulations for multiple angles of attack did not converge. This made it difficult to validate the CFD toolchain, which included the transition model. Modelling flow separation with RANS simulations, including a transition model, remains challenging, as even small deviations in the predicted separation point can significantly affect the maximum lift coefficient and stall angle. This could explain the difference in the measured and simulated coefficients. The lowest angle that converged was $\alpha = 6°$. The lift and drag coefficients from this simulation were close to the experimental values, indicating

possible agreement within the linear part of the polar. However, the limited number of converged cases means this cannot be stated with confidence.

Oil-flow visualisation revealed the presence of a laminar separation bubble on the suction side, whereas the pressure side is governed by a corner eddy and a recirculation zone on the V3 model. These flow phenomena were also observed in literature [22]. The zigzag tapes did influence the flow topology, especially the laminar separation bubble on the suction side and the size of the recirculation zone at lower angles of attack. The CFD analysis was able to capture the size of the recirculation zone accurately, whereas the size of the corner eddy proved to be more difficult.

Despite the successful completion of the experimental campaign, the scientific quality of the results was limited by a number of factors. The construction and surface imperfections of the models resulted in uncertainty of the aerodynamic coefficients. The thin canopy with one additional central rib still deflected under high load, and the rib may have significantly influenced the drag coefficient. With the current measurement setup, the moment coefficient was not possible to measure. The moment coefficient is required for the correction of the angle of attack. Furthermore, at high angles of attack, the drag coefficient was not measurable due to the size of the wake. The drag coefficient is used in the correction of the lift coefficient, thus making the lift coefficient more uncertain. Infrared imaging only indicated the transition location on the suction side and was not suitable for visualising the flow topology on the pressure side. After construction, there were discrepancies in the shape of the wind tunnel models, which influenced the results. Furthermore, these discrepancies were not included in the CFD analysis, resulting in a comparison that is not fully representative. Finally, several angles of attack did not converge with the CFD analysis, including the transition model, preventing a complete validation across the full range of angles of attack.

8.2. Recommendations

As this is the first dedicated experimental research on LEI airfoils, several recommendations can be made for future work. The models were manufactured by an external party. It was expected that this company would roll the shape of the canopy, resulting in a smooth surface. As the radius of the canopy was too small at the leading edge, this method could not be used. Therefore, the sheet metal was bent in small intervals to approximate a smooth curvature. These small bends did have an influence on the airflow across the airfoil, as it is not a perfectly smooth surface. The black decoration foil did aid in smoothing out the surface, but it was not perfect. Furthermore, upon delivery of the models, it was observed that the models were twisted. Due to the relatively thin sheet metal, the heat generated during welding warped the metal canopy, resulting in a twisted model. It was possible to untwist Model2 prior to the experimental test successfully, but the V3 model had to be remade. For future experimental testing, it would be better to construct the models using carbon fibre moulding. This eliminates the imperfection created by bending the material as well as ensuring a perfectly smooth model. The trailing edge could also be rounded, which is used in the CFD simulations.

For future models, it is advised to remove the centre rib and increase the thickness of the canopy. The rib influenced the drag coefficient more than expected. At higher angles of attack, the oil flow visualisation around the rib was also distorted. This showed the influence of the rib at higher angles of attack. Removing this rib altogether would solve these problems, as the influence of a thicker canopy is less pronounced than using a rib. If the model is constructed out of carbon fibre, the canopy thickness would not influence the smallest possible radius at the leading edge, and therefore, the canopy can be made thicker. This would also aid in achieving the initial goal of testing at $\mathrm{Re} = 2 \times 10^6$.

The side plates of the model were designed to improve the rigidity of the model. During the installation of the models inside the test section of the LTT, it was observed that the side plates could have been designed as the ground plates used in the turntable of the LTT. This would significantly improve the installation process of the models, as there are no bolts required to mount the models to the ground plates. Another benefit of designing the side plates as ground plates is that there is no obstruction of the airflow on the top and bottom walls of the wind tunnel. This obstruction does influence the results, but it is expected that this influence is small.

For future design of the models, it is advised to reduce the chord length of the models. During the experiments, the wake grew too large at high angles of attack, which resulted in the wakerake not

being able to measure the total reduction of momentum in the flow. This meant that there are multiple data points missing for the drag coefficient at high angles of attack. Next to this, the angle of attack had to be corrected with the uncorrected moment coefficient. As the moment coefficient could not be measured with the current setup, the angle of attack is corrected using the moment coefficient obtained by CFD. A different method for measuring the flowfield around the model is the use of particle image velocimetry (PIV). With PIV, the data can be used to derive the surface pressure, lift, drag and moment coefficient without interfering with the flowfield [58][59]. This measurement technique would eliminate most of the shortcomings of the experimental test.

After construction, the exact shape of the airfoils has changed compared to the airfoil shape used in CFD. To improve the CFD results, the exact shape of the airfoil models can be measured using lasers. Using this exact profile, a more accurate shape can be used as an input for CFD. Furthermore, the CFD results, including the $\gamma - \tilde{\mathrm{Re}}_{\theta t}$ transition model [46], resulted in multiple non-converged angles of attack. The study by Masure [15] did not include an in-depth analysis of different transition models and optimisation of relaxation factors. A future study is required to optimise the Python toolchain developed by Masure [15], to increase the amount of converged angles of attack. The experimental results obtained by this study can be used to validate the effectiveness of different transition models. Next to this, an in-depth analysis of unsteady Reynolds-averaged Navier-Stokes (URANS) is beneficial, as this simulation method also captures the unsteady effects of the aerodynamics around an LEI airfoil. These unsteady effects are due to the recirculation zone and separation of the airflow over the suction side. An attempt has been made for an URANS simulation. The results and the simulation setup are explained in App. C.

At last, during the oil flow visualisation, only positive angles of attack were tested on the suction side with the V3 model. As seen by the infrared images, the location of transitions stays constant for these angles, meaning that the laminar separation bubble does not move. It would have been interesting to see if a laminar separation bubble is present at negative angles of attack. Furthermore, as the location of transition does change with increasing angle of attack for Model2, it would have been interesting to see if a laminar separation bubble is even formed on Model2 or if the flow transitions from laminar to turbulent without forming a laminar separation bubble.

A

LEI airfoil deflection

This Appendix shows the resultant deflection due to the expected load at $\alpha = 14°$. This angle results in the maximum lift which the model can generate during testing at $\mathrm{Re} = 2 \times 10^6$. The deflection analysis is done using the FEM solver in SolidEdge for Model2. The results can be seen in Fig. A.1 for a varying canopy thickness of 1, 2, and $3\,\mathrm{mm}$

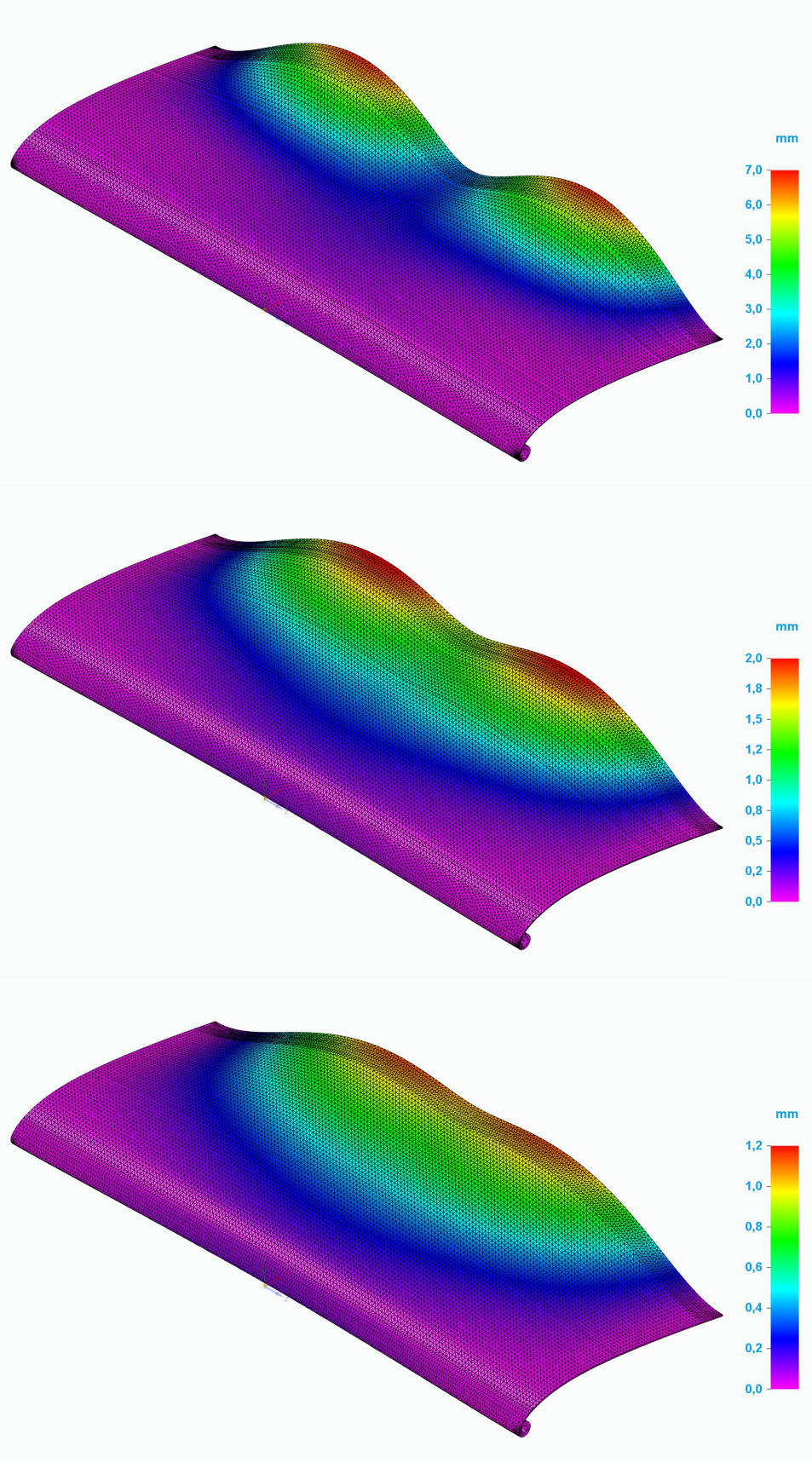

Figure A.1: Displacement of Model2 at $\alpha = 14°$ and $\mathrm{Re} = 2 \times 10^6$ for different canopy thicknesses: $1\,\mathrm{mm}$ (top), $2\,\mathrm{mm}$ (middle), and $3\,\mathrm{mm}$ (bottom).

B

Correction factors

This appendix shows the correction factors for all $\mathrm{Re} = 5 \times 10^5$ cases at every angle of attack for both the V3 model and Model2. These correction factors can be seen in Fig. B.1. Furthermore, the correction factors are averaged between $\alpha = 2°$ and $\alpha = 8°$ and given in Table B.1. This averaged value is used in the correction of the lift coefficient.

Table B.1: Correction factors for the V3 model and Model2 cases.

(a) V3 model cases

Case	Correction factor
No ZZ, $\mathrm{Re} = 10^6$	1.2244
No ZZ, $\mathrm{Re} = 1.5 \times 10^6$	1.2270
No ZZ, $\mathrm{Re} = 5 \times 10^5$	1.2333
ZZ on bottom at $90°$, $\mathrm{Re} = 10^6$	1.2260
ZZ on bottom at $90°$, $\mathrm{Re} = 5 \times 10^5$	1.2343
ZZ on top at 5%, $\mathrm{Re} = 10^6$	1.2256
ZZ on top at 5%, $\mathrm{Re} = 5 \times 10^5$	1.2332
ZZ on bottom at $90°$ and on top at 5%, $\mathrm{Re} = 10^6$	1.2244
ZZ on bottom at $90°$ and on top at 5%, $\mathrm{Re} = 5 \times 10^5$	1.2296
ZZ on bottom at $90°$ and on top at 3%, $\mathrm{Re} = 10^6$	1.2286
ZZ on bottom at $45°$ and on top at 3%, $\mathrm{Re} = 10^6$	1.2280
ZZ on bottom at $45°$, $\mathrm{Re} = 10^6$	1.2273
ZZ on bottom at $45°$, $\mathrm{Re} = 5 \times 10^5$	1.2377

(b) Model2 cases

Case	Correction factor
No ZZ, $\mathrm{Re} = 10^6$	1.2243
No ZZ, $\mathrm{Re} = 2 \times 10^6$	1.2148
No ZZ, $\mathrm{Re} = 5 \times 10^5$	1.2250
ZZ on bottom at $90°$, $\mathrm{Re} = 10^6$	1.2274
ZZ on bottom at $90°$, $\mathrm{Re} = 5 \times 10^5$	1.2338
ZZ on top at 10%, $\mathrm{Re} = 10^6$	1.2234
ZZ on top at 10%, $\mathrm{Re} = 5 \times 10^5$	1.2259
ZZ on top at 5%, $\mathrm{Re} = 10^6$	1.2266
ZZ on top at 5%, $\mathrm{Re} = 5 \times 10^5$	1.2369
ZZ on bottom at $90°$ and on top at 5%, $\mathrm{Re} = 10^6$	1.2281
ZZ on bottom at $90°$ and on top at 5%, $\mathrm{Re} = 5 \times 10^5$	1.2341
ZZ on bottom at $90°$, $\mathrm{Re} = 10^6$	1.2296
ZZ on bottom at $90°$, $\mathrm{Re} = 5 \times 10^5$	1.2336

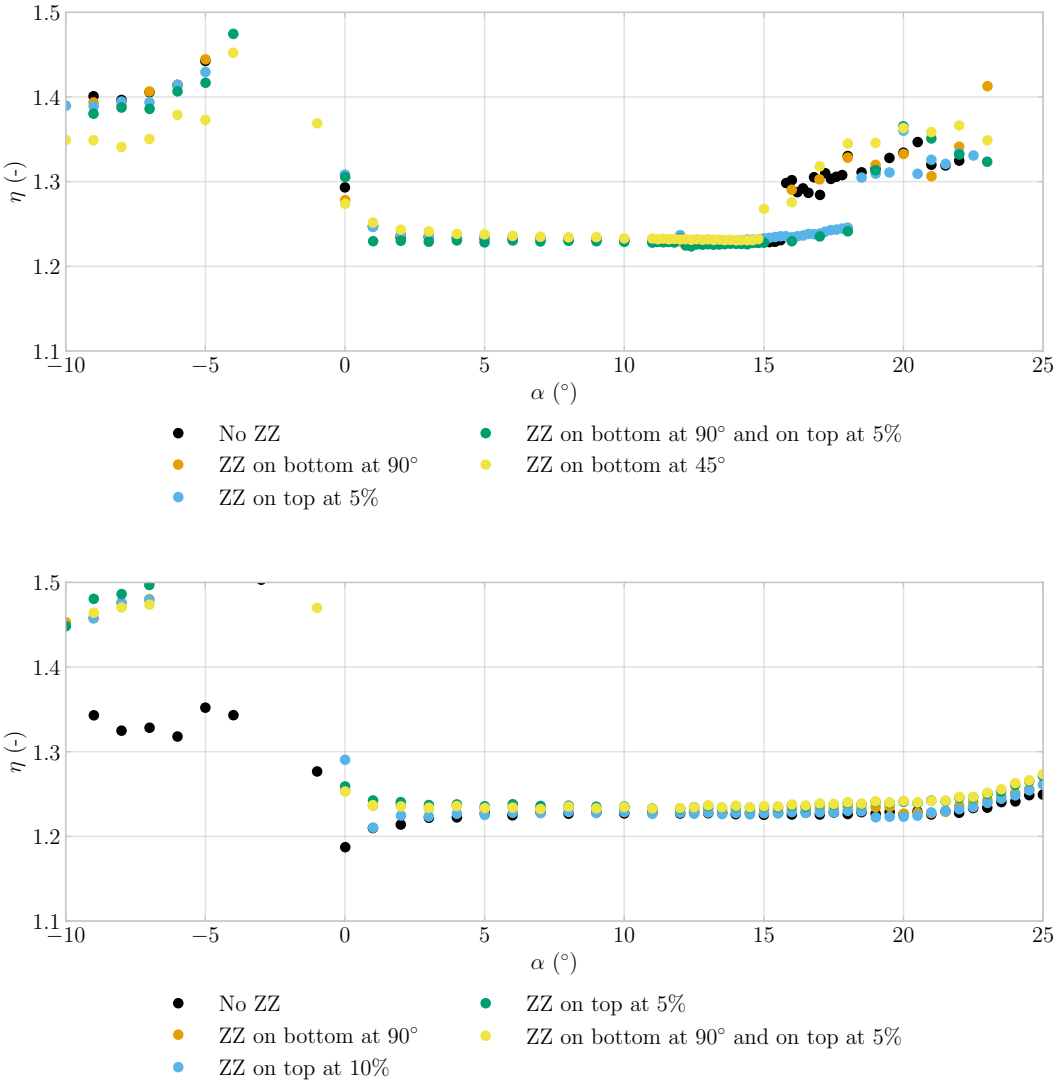

Figure B.1: Correction factors for all α at $\mathrm{Re} = 5 \times 10^5$ for the V3 model (top) and Model2 (bottom).

C

URANS

An attempt has been made to perform URANS to solve for the unsteady behaviour of the airflow using the CFD toolchain developed by Masure [15]. First the simulation setup will be discussed after which the results will be given in Sect. C.1 and C.2 respectively. This chapter concludes with recommendations for future research in Sect. C.3.

C.1. Simulation setup

The OpenFOAM [44] simulation for $\mathrm{Re} = 3 \times 10^5$ was performed using the same mesh as the original RANS simulations. Pimplefoam is specified to indicate an URANS simulation using an Euler time discretisation. Furthermore, the Endtime is set at 0.1 with a $\Delta t = 5 \times 10^{-4}$. Adjustable timestep is set to True with a maximum Courant (Co) number of 0.3 where Co is defined as

$$\mathrm{Co} = \frac{|u|\,\Delta t}{\Delta x} \tag{C.1}$$

Setting a maximum Courant number allows the timestep Δt to reduce if this timestep would result in a $\mathrm{Co} > 0.3$. Keeping the Courant number below 0.3 results in a more stable and accurate result, but it does require more steps to go to the specified Endtime.

The Pimplefoam loop parameters are as specified in Table. C.1

Table C.1: Loop parameters for pimpleFoam.

Parameter	Value
nOuterCorrectors	2
nCorrectors	2
nNonOrthogonalCorrectors	1
momentumPredictor	On

Table C.2: Relaxation factors for pimpleFoam.

Parameter	value
p	0.2
U	0.3
k	0.3
ω	0.3

The field (p) and equation (U, k, ω) relaxation factors used in the Pimplefoam can be seen in Table C.2. The equation relaxation factors influence the linear iterations. These linear iterations have a maximum set to 30 with a tolerance of 10^{-7} for each parameter.

C.2. Results

The V3 model was tested using URANS and RANS at $\alpha = 2°$ and $\alpha = 12°$ with $\mathrm{Re} = 3 \times 10^5$. Two RANS simulation have been done, one assuming a fully turbulent boundary layer and the other including a transition model. The results, including the experimental data at $\mathrm{Re} = 5 \times 10^5$, are tabulated in Table C.3. The lift coefficient seems plausible, whereas the drag coefficient is rather high. When

increasing the Reynolds number to $\mathrm{Re} = 5 \times 10^5$, the aerodynamic coefficients diverge after a few iterations. The RANS simulation did converge, unlike the simulation at $\mathrm{Re} = 5 \times 10^5$. The residuals can be seen in Fig. C.1. The flow residuals do fall below the 8×10^{-7} threshold while the force residuals show oscillatory behaviour. This indicates unsteadiness. This shows the need for URANS simulations.

Table C.3: Results for URANS, RANS and experimental data for C_l and C_d at $\alpha = 2°$ and $\alpha = 12°$

Angle	Parameter	URANS	RANS	RANS (incl transition)	WT $\mathrm{Re} = 5 \times 10^5$	WT σ
2°	C_l	0.456	0.567	0.553	0.586	0.0028
2°	C_d	0.084	0.032	0.034	0.031	0.0025
12°	C_l	1.308	1.524	0.756	1.797	0.0021
12°	C_d	0.331	0.073	0.192	0.034	0.0008

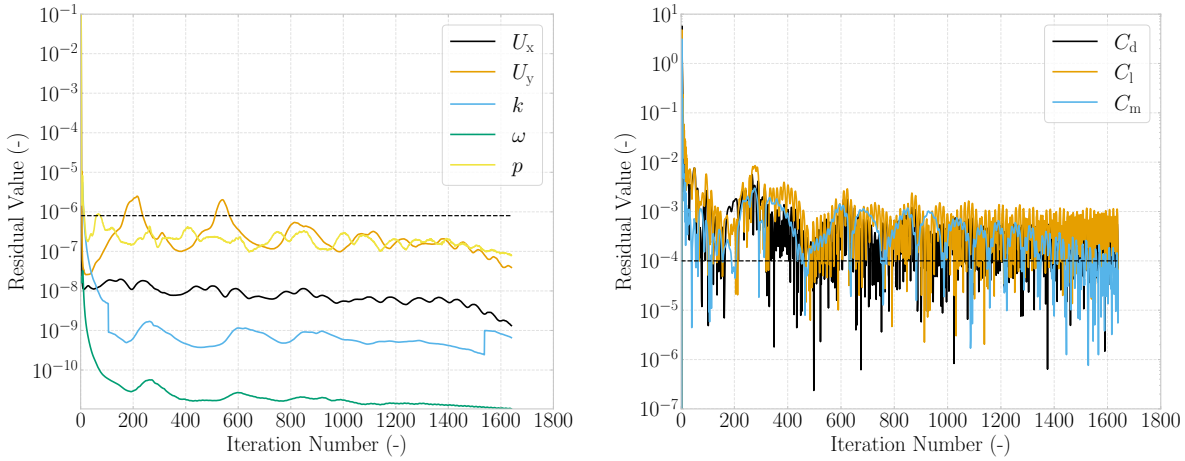

Figure C.1: Final flow (left) and force (right) residuals of the V3 model assuming a fully turbulent boundary layer at $\alpha = 2°$ and $\mathrm{Re} = 3 \times 10^5$

C.3. Recommendations

The reason for the divergence is still unknown, but it could be due to several different parameters. The mesh used in the URANS simulations was developed based on RANS simulations. The mesh size could be too coarse to capture the vortex dynamics at higher Reynolds numbers. Furthermore, increasing the Reynolds number results in a thinner viscous sublayer. This will in turn increase the y^+ value as the change, which could make the wall model inconsistent.

Next, with increasing Reynolds number, the inflow velocity increases. This will require a smaller Δt to keep the simulations stable. Furthermore, the maximum CO-number could be adjusted to keep the simulation stable.

At last, the simulations should be performed on the high-performance computer (HPC) at the TU Delft. This computer can reduce the computation time massively. This allows for smaller Δt with a higher Endtime. This could improve the simulation results.

Bibliography

[1] U. Ahrens, M. Diehl, and R. Schmehl, eds. *Airborne Wind Energy*. Berlin, Heidelberg: Springer, 2013. ISBN: 978-3-642-39964-0. DOI: 10.1007/978-3-642-39965-7.

[2] Kitepower. *Kitepower – airborne wind energy systems*. Start-up company from TU Delft. [Accessed: April 8, 2025]. 2025. URL: https://thekitepower.com/.

[3] J. A. W. Poland et al. "Wind tunnel load measurements of a leading-edge inflatable kite rigid scale model". In: *Wind Energy Science Discussions* (2025). Discussion paper, in review, pp. 1–33. DOI: 10.5194/wes-2025-77. URL: https://wes.copernicus.org/preprints/wes-2025-77/.

[4] J. Oehler, M. van Reijen, and R. Schmehl. "Experimental investigation of soft kite performance during turning maneuvers". In: *Journal of Physics: Conference Series* 1037.5 (2018), p. 052004. DOI: 10.1088/1742-6596/1037/5/052004.

[5] R. van der Vlugt et al. "Quasi-steady model of a pumping kite power system". In: *Renewable Energy* 131 (2019), pp. 83–99. DOI: 10.1016/j.renene.2018.07.023.

[6] G. Lebesque. "Steady-state RANS simulation of a leading edge inflatable wing with chordwise struts". [Accessed: March 2025]. Master's thesis. Delft University of Technology, 2020. URL: http://resolver.tudelft.nl/uuid:f0bc8a1e-088d-49c5-9b77-ebf9e31cf58b.

[7] P. Demkowicz. "Numerical analysis of the flow past a leading edge inflatable kite wing using a correlation-based transition model". [Accessed: April 2025]. Master's thesis. Delft University of Technology, 2019. URL: http://resolver.tudelft.nl/uuid:c53aa605-1b2e-47a7-b991-c1917d7463b4.

[8] J. Berens. "Dynamic nonlinear aeroelastic behaviour of flexible wings in an airflow". [Accessed: April 2025]. Master's thesis. Delft University of Technology, 2015. URL: http://resolver.tudelft.nl/uuid:aa859e12-1087-46a5-80c6-7e63053a017a.

[9] M. L. Loyd. "Crosswind kite power". In: *Journal of Energy* 4.3 (1980), pp. 106–111. DOI: 10.2514/3.48021.

[10] U. Fechner. "A methodology for the design of kite-power control systems". PhD thesis. Delft University of Technology, 2016. ISBN: 978-94-028-0409-6. DOI: 10.4233/uuid:85efaf4c-9dce-4111-bc91-7171b9da4b77.

[11] M. Folkersma, R. Schmehl, and A. Viré. "Steady-state aeroelasticity of a ram-air wing for airborne wind energy applications". In: *Journal of Physics: Conference Series* 1618.3 (2020), p. 032018. DOI: 10.1088/1742-6596/1618/3/032018.

[12] O. Cayon, M. Gaunaa, and R. Schmehl. "Fast aero-structural model of a leading-edge inflatable kite". In: *Energies* 16.7 (2023). DOI: 10.3390/en16073061.

[13] J. Poland. "Modelling aeroelastic deformation of soft wing membrane kites". [Accessed: April 2025]. Master's thesis. Delft University of Technology, 2022. URL: http://resolver.tudelft.nl/uuid:39d67249-53c9-47b4-84c0-ddac948413a5.

[14] J. Breukels. "An engineering methodology for kite design". [Accessed: April 2025]. PhD thesis. Delft University of Technology, 2011. URL: https://resolver.tudelft.nl/uuid:cdece38a-1f13-47cc-b277-ed64fdda7cdf.

[15] K. Masure. "Regression modeling on the 2D aerodynamics of LEI kite profiles". [Accessed: April 2025]. Master's thesis. Delft University of Technology, 2025. URL: https://resolver.tudelft.nl/uuid:865d59fc-ccff-462e-9bac-e81725f1c0c9.

[16] J. Oehler and R. Schmehl. "Aerodynamic characterization of a soft kite by in situ flow measurement". In: *Wind Energy Science* 4 (2019), pp. 1–21. DOI: 10.5194/wes-4-1-2019.

[17] O. Cayon, S. Watson, and R. Schmehl. “Kite as a sensor: Wind and state estimation in tethered flying systems”. In: *Wind Energy Science Discussions* (2025). Discussion paper, in review, pp. 1–41. DOI: 10.5194/wes-2024-182. URL: https://wes.copernicus.org/preprints/wes-2024-182/.

[18] H. Hu, M. Tamai, and J. T. Murphy. “Flexible-membrane airfoils at low Reynolds numbers”. In: *Journal of Aircraft* 45.5 (2008), pp. 1767–1778. DOI: 10.2514/1.35303.

[19] R. G. den Boer. *Low speed aerodynamic characteristics of a two-dimensional sail wing with adjustable slack of the sail*. Tech. rep. LR-307. [Accessed: April 2025]. Delft, The Netherlands: Technische Hogeschool Delft, Oct. 1980. URL: https://resolver.tudelft.nl/uuid:18ae2cc6-434e-49c8-9296-d3fa450850a5.

[20] M. R. Waszak, L. N. Jenkins, and P. Ifju. “Stability and control properties of an aeroelastic fixed wing micro aerial vehicle”. In: *AIAA Atmospheric Flight Mechanics Conference*. AIAA Paper 2001-4005. Montreal, Canada, Aug. 2001. URL: https://ntrs.nasa.gov/citations/20010081319.

[21] R. C. Leuthold. “Multiple-wake vortex lattice method for membrane wing kites”. [Accessed: April 2025]. Master’s thesis. Delft University of Technology, 2015. URL: https://resolver.tudelft.nl/uuid:4c2f34c2-d465-491a-aa64-d991978fedf4.

[22] M. Folkersma, R. Schmehl, and A. Viré. “Boundary layer transition modeling on leading edge inflatable kite airfoils”. In: *Wind Energy* 22.6 (2019), pp. 884–897. DOI: 10.1002/we.2329.

[23] W. Terra, A. Sciacchitano, and F. Scarano. “Cyclist Reynolds number effects and drag crisis distribution”. In: *Journal of Wind Engineering and Industrial Aerodynamics* 200 (2020), p. 104143. DOI: 10.1016/j.jweia.2020.104143.

[24] J. Jonkman. *Google / Makani energy kite modeling: Cooperative Research and Development Final Report, CRADA Number CRD-17-00569*. Technical report NREL/TP-5000-80635. Golden, Colorado, USA: National Renewable Energy Laboratory (NREL), 2021. DOI: 10.2172/1813012.

[25] R. Damiani et al. “A vortex step method for nonlinear airfoil polar data as implemented in KiteAeroDyn”. In: *AIAA SciTech 2019 Forum*. AIAA Paper 2019-0804. NREL/CP-5000-74483. Conference paper. San Diego, California, USA: American Institute of Aeronautics and Astronautics (AIAA), Jan. 2019. DOI: 10.2514/6.2019-0804.

[26] M. Ranneberg. *Direct wing design and inverse airfoil identification with the nonlinear Weissinger method*. 2015. arXiv: 1501.04983 [physics.flu-dyn]. URL: https://arxiv.org/abs/1501.04983.

[27] O. Cayon. “Fast aeroelastic model of a leading-edge inflatable kite for the design phase of airborne wind energy systems”. [Accessed: April 2025]. Master’s thesis. Delft University of Technology, 2022. URL: http://resolver.tudelft.nl/uuid:aede2a25-4776-473a-8a75-fb6b17b1a690.

[28] M. E. Deaves. “An investigation of the non-linear 3D flow effects relevant for leading edge inflatable kites”. [Accessed: April 2025]. Master’s thesis. Delft University of Technology, 2015. URL: http://resolver.tudelft.nl/uuid:ccb56154-0b70-4a41-8223-24b0f8d145c5.

[29] S. Sachdeva. “Impact of turning induced shape deformations on aerodynamic performance of leading edge inflatable kites”. [Accessed: April 2025]. Master’s thesis. Delft University of Technology, 2017. URL: http://resolver.tudelft.nl/uuid:3dd54665-f48c-4e48-9f57-dc285cece612.

[30] SurfPlan Pty Ltd. *SurfPlan software*. [Accessed: April 2025]. 2025. URL: http://www.surfplan.com.au/sp/.

[31] R. van Kappel. “Aerodynamic analysis tool for dynamic leading edge inflated kite models: A nonlinear vortex lattice method”. [Accessed: April 2025]. Master’s thesis. Delft University of Technology, 2012. URL: https://repository.tudelft.nl/record/uuid:385d316b-c997-4a02-b0f3-b30c40fffc32.

[32] J. Watchorn. “Polynomial regression model for aerodynamic wind loading of LEI kites”. [Accessed: March 2025]. Master’s thesis. Delft University of Technology, 2023. URL: https://resolver.tudelft.nl/uuid:42f611a2-ef79-4540-a43c-0ea827700388.

[33] T. Corentin. *Kite design, methods and digital simulations*. Technical report. End-of-study internship report; Fluid Dynamics—Energy Transport and Environment. Reference about 2D kite profiles from BTS comparison (Xfoil / GridPro / Gmsh). Accessible on request: Beyond-The-Sea.com. Toulouse, France: Institut Supérieur de l’Aéronautique et de l’Espace, 2023.

[34] Delft University of Technology. *Open jet facility (OJF)*. [Accessed: April 2025]. 2025. URL: https://www.tudelft.nl/lr/organisatie/afdelingen/flow-physics-and-technology/facilities/low-speed-wind-tunnels/open-jet-facility.

[35] M. A. M. Folkersma. “Aeroelasticity of membrane kites: Airborne wind energy applications”. PhD thesis. Delft University of Technology, 2022. DOI: 10.4233/uuid:eae39f5a-49bc-438b-948f-b6ab51208068.

[36] A. Bruining. *Aerodynamic characteristics of a curved plate airfoil section at Reynolds numbers 60000 and 100000 and angles of attack from -10 to +90 degrees*. Technical report LR-281. Historical technical report; Accessed: May 2025. Delft University of Technology, Department of Aerospace Engineering, 1979. URL: http://resolver.tudelft.nl/uuid:6b92442a-01f7-4b7c-8d53-c4f10720ff3e.

[37] Delft University of Technology. *Low turbulence tunnel (LTT)*. [Accessed: March 2025]. 2025. URL: https://www.tudelft.nl.

[38] C. Huijts and M. Voskuijl. “The impact of control allocation on trim drag of blended wing body aircraft”. In: *Aerospace Science and Technology* 46 (2015), pp. 72–81. DOI: 10.1016/j.ast.2015.07.001.

[39] Siemens Digital Industries Software. *Solid Edge*. Version 2025; Accessed: April 2025. 2025. URL: https://solidedge.siemens.com/.

[40] D. A. M. De Tavernier. “Aerodynamic advances in vertical-axis wind turbines”. PhD thesis. Delft University of Technology, 2021. DOI: 10.4233/uuid:7086f01f-28e7-4e1b-bf97-bb3e38dd22b9.

[41] S. Bernardy. *Personal communication*. Multiple discussions with S. Bernardy in 2025. 2025.

[42] Technoweld. *Basics of distortion in welding*. [Accessed: April 2025]. 2019. URL: https://technoweld.com.au/2019/07/30/basics-of-distortion-in-welding/.

[43] Pointwise Inc. *Pointwise: Computational fluid dynamics (CFD) meshing software*. [Accessed: August 2025]. 2023. URL: https://www.pointwise.com.

[44] OpenCFD Ltd. *OpenFOAM v2006*. Version v2006; Accessed: August 2025. 2020. URL: https://www.openfoam.com.

[45] J. H. Ferziger, M. Perić, and R. L. Street. *Computational methods for fluid dynamics*. 4th ed. Cham, Switzerland: Springer Nature Switzerland AG, 2020. ISBN: 978-3-319-99691-2. DOI: 10.1007/978-3-319-99693-6.

[46] R. B. Langtry and F. R. Menter. “Correlation-based transition modeling for unstructured parallelized computational fluid dynamics codes”. In: *AIAA Journal* 47.12 (2009), pp. 2894–2906. DOI: 10.2514/1.42362.

[47] W. Timmer and R. P. J. O. M. van Rooij. “Summary of the Delft University wind turbine dedicated airfoils”. In: *Journal of Solar Energy Engineering* 125.4 (2003), pp. 488–496. DOI: 10.1115/1.1626129.

[48] T. Jelínek. “Experimental investigation of the boundary layer transition on a laminar airfoil using infrared thermography”. In: *EPJ Web of Conferences* 180 (2018), p. 02040. DOI: 10.1051/epjconf/201818002040.

[49] C. L. Running et al. “A wrap-film technique for infrared thermography heat-transfer measurements in high-speed wind tunnels”. In: *Experimental Thermal and Fluid Science* 135 (2022), p. 110604. DOI: 10.1016/j.expthermflusci.2022.110604.

[50] D. Ragni. *Lecture slides for “Flow Measurement Techniques” [Course AE4180]*. [Accessed: August 2025]. 2024.

[51] A. L. Braslow and E. C. Knox. *Simplified method for determination of critical height of distributed roughness particles for boundary-layer transition at Mach number from 0 to 5*. Technical report NACA TN 4363. Historical technical report. National Advisory Committee for Aeronautics (NACA), Langley Aeronautical Laboratory, 1958. URL: https://ntrs.nasa.gov/citations/19930085292.

[52] Y. Zhang, A. van Zuijlen, and G. van Bussel. “The MEXICO rotor aerodynamic loads prediction: Zigzag tape effects and laminar-turbulent transition modeling in CFD”. In: *Journal of Wind Engineering and Industrial Aerodynamics* 168 (2017), pp. 152–163. DOI: 10.1016/j.jweia.2017.06.002.

[53] I. H. Abbott, A. E. von Doenhoff, and L. S. Stivers Jr. *Summary of airfoil data*. Technical report Report 824. Historical technical report. Washington, D.C.: National Advisory Committee for Aeronautics (NACA), 1945. URL: https://ntrs.nasa.gov/citations/19930090976.

[54] D. Althaus. *Measurement of lift and drag in the laminar wind tunnel*. Technical report. University of Stuttgart, 2005. URL: https://www.iag.uni-stuttgart.de/dateien/pdf/laminarwindkanal_messtechniken/althaus_2.pdf.

[55] C. Dalton. “Allen and Vincenti blockage corrections in a wind tunnel”. In: *AIAA Journal* 9.9 (1971), pp. 1864–1865. DOI: 10.2514/3.6435.

[56] W. A. Timmer. “Wind tunnel wall corrections for two-dimensional testing up to large angles of attack”. In: *Handbook of Wind Energy Aerodynamics*. Ed. by B. Stoevesandt et al. Cham, Switzerland: Springer Nature Switzerland, 2021. DOI: 10.1007/978-3-030-05455-7_27-1.

[57] D. Weihs and J. Katz. “Cellular patterns in poststall flow over unswept wings”. In: *AIAA Journal* 21.12 (1983), pp. 1757–1759. DOI: 10.2514/3.8321.

[58] B. W. van Oudheusden, E. W. F. Casimiri, and F. Scarano. “Aerodynamic load characterisation of a low-speed aerofoil using particle image velocimetry”. In: *The Aeronautical Journal* 112.1130 (2008), pp. 197–205. DOI: 10.1017/S000192400000213X.

[59] D. Ragni et al. “Surface pressure and aerodynamic loads determination of a transonic airfoil based on particle image velocimetry”. In: *Measurement Science and Technology* 20 (2009), p. 074005. DOI: 10.1088/0957-0233/20/7/074005.